Neutron Star Structure from Electromagnetic and Gravitational Wave Observations

A Dissertation Presented for the

Doctor of Philosophy

Degree

The University of Tennessee, Knoxville

Mohammad Al-Mamun

August 2021

dedicated to my parents

for their love, support, and encouragements

Acknowledgments

First and foremost, I would like to thank my parents for their utmost belief in me. Despite being thousands of miles apart, their continuous support and advice cleared my doubts time and time again during this period of my life.

I am incredibly grateful to my Ph.D. supervisor, Dr. Andrew W. Steiner, who wholeheartedly helped me gain the necessary knowledge for this research project. The conversations we had and the guidance he provided over the years helped me excel both personally and professionally.

I want to thank my friends and colleagues here at UTK for a wonderful time during this phase of my life. I am also thankful to the administrators in my department, especially Chrissane Romeo, for helping me with all those pesky paperwork.

To the friends, I gained in BSA (Knoxville), take my earnest gratitude for those warm feelings of having a home away from home. I especially like to thank Amirus Saleheen and Mohammed Fahad Hassan for their help during my transition to UTK. Muktadir Rahman, Mujibur Rahman, Arup Barua, and to all my friends with whom I shared this dream of pursuing a Ph.D., thanks to you, those dreamy evenings are becoming a reality. I am genuinely thankful to have you all as my friends during this journey.

Furthermore, this work would not have been possible without the financial support from NSF Grant Nos. PHY 155487 and AST 1909490.

Abstract

Neutron star (NS) research primarily relied on spectral observations before the first gravitational wave (GW) detection from the binary neutron star merger was done by the LIGO-VIRGO collaboration. The GW170817 merger event provided mass and tidal deformability $\tilde{\Lambda}$ constraints for neutron stars. This project used these constraints and associated them with the constraints made by the NS X-ray observations to construct neutron star models. Selective X-ray sources were used in this work, which showed reliable uncertainties from their previous uses. The mass-radius constraints from the electromagnetic (EM) observations were constructed from seven quiescent low-mass X-ray binaries (QLMXBs), three photospheric radius expansion X-ray busters (PREs), and the NICER observation of PSR J0030+451. Also, two different neutron star equation of state (EOS) priors, three polytropes (3P) and four line-segment (4L), were used for the analyses.

The radial constraints of a 1.4 $M_{\odot}$ NS from the combined dataset with GW, QLMXBs, and PREs were $R_{1.4} \in [11.21\ \mathrm{km}, 12.55\ \mathrm{km}]$ and $R_{1.4} \in [11.25\ \mathrm{km}, 12.39\ \mathrm{km}]$ for the 3P and 4L EOS priors, respectively. Adding the NICER observation to the other data did not improve these constraints but shifted slightly towards the larger radii. Two models were constructed by convolution operations on EM data, named intrinsic scattering (IS), to test unknown uncertainties in them. No significant variations were found from these IS analyses.

This project also compared several nearly EOS independent quantities of neutron star binary parameters with the model posteriors. Also, the Pearson

correlation tests were done to check radial dependencies of the slope of the symmetry energy L and the minimum value of the maximum mass neutron star M_{max}. These tests showed that M_{max} is always independent of R, but the correlation between L and R depends on the EOS prior.

Table of Contents

List of Tables

List of Figures

Chapter 1

Introduction

Neutron stars (NSs) are objects with near-infinite curiosities. Neutron stars are the remnant of core-collapse supernova explosions. Theoretical predictions of neutron stars precede the first confirmed observation by decades. In past 50 years, research on NSs and their evolution [11, 91, 92] has gained momentum in most astrophysics communities. NSs can also be used to determine the relationship between the thermodynamic quantities (pressure P, densities ρ, and temperature T) of dense matter [19, 69]. The core density of a neutron star can go far beyond the densities reproducible in terrestrial nuclear experiments. Thus, neutron stars can be treated as unique laboratories to determine the nucleon-nucleon interactions at larger densities.

The mass measurements of neutron stars are fairly accurate [120]. Other than the NS masses, parameters such as radius [41, 68, 70, 71, 113, 114] and surface temperature are mostly model-dependent. All forms of observational data of neutron stars from old (Chandra, Rossi, XMM-Newton) [18, 63, 89] and emergent (LIGO-VIRGO collaboration, NICER) [73, 93, 102] exploratory missions should be added to update existing models. Building an all-inclusive model to get the NS structure is still a challenge for theorists. Data-driven modeling has been proven to be the best approach to tackle this issue of acquiring a comprehensive model. This dissertation will address the methods used to incorporate different observations to build models comparable with the phenomenological results from neutron star structure analyses. Starting with a brief introduction of NSs, this dissertation will present a brief review of the phenomenological models of neutron stars. The underlying physics of neutron stars and the numerical methods used in this project to combine different observations are cataloged later. The final chapters are divided to report the current inferences of NS properties, and the possible improvements on these established models.

1.1 A Brief Overview of Neutron Star

1.1.1 Origin

At some point in their evolution, all stars will run out of fuel to burn. Massive stars are more dynamic than the lower mass stars. The excess mass generate immense pressure inside the star, accelerating their lives and causing them to go through more fusion cycles. Depending on their initial masses and the metallicity of their cores, the final fate of these massive stars can have different outcomes [50, 116]. Progenitor stars with gravitational masses in-between $8-20$ $M_\odot$ will form neutron stars after supernova.

A supernova is the explosion of a massive progenitor star [15, 107] and Neutron stars are the outcome of type Ib, type Ic or type II supernovae. These supernova types represents the class that undergoes core-collapse process. In a type II supernova [10, 16, 17], the star runs out of nuclear fuel by fusing atoms until the burning process reaches Nickel-56 [40]. At this point, the star cannot generate more energy by fusion and, it is supported only by the degeneracy pressure of electrons to prevent collapse. This degeneracy pressure fails when the core mass goes beyond $> 1.2\ \mathrm{M}_\odot$ and this initiates the core-collapse process [72]. The Chandrasekhar limit provides a mathematical relation for the core of collapsing star based on the electron fraction number Y_e. This Y_e is the ratio of remaining electrons and the total baryons (neutrons and protons) in the core . The Chandrasekhar mass limit M_ch is given as,

$$M_\mathrm{ch} = 5.76\ (Y_\mathrm{e})^2 \tag{1.1}$$

For $Y_\mathrm{e} = 0.5$, the Chandrasekhar limit is $1.4\ \mathrm{M}_\odot$ which is widely used as a canonical mass for the core of collapsed star. The extreme heat in the core starts to disassemble nuclei to the elementary level (electrons, protons and, neutrons). The capture process of electrons on protons starts to produce more neutrons and, the energy produced from this process is carried away by electron neutrinos

$$p + e^- \to n + \nu_e\,. \tag{1.2}$$

Neutrons are also produced by inverse beta decay at the core, and the core becomes neutron-rich over time

$$\bar{\nu}_e + p \to n + e^+\,. \tag{1.3}$$

After collapsing by five orders of magnitude in density, neutron-neutron repulsive interaction stops the core from further collapse. The infalling materials bounce back due to this repulsive force and initiate shock waves towards the star's surface. These shock waves stall between the core and surface layer of the star. The neutrinos that failed to escape and neutrinos produced by the pair annihilation process energize this shock wave to a point where t explodes.

$$e^+ + e^- \rightarrow \nu + \bar{\nu} \tag{1.4}$$

Most of the materials get ejected during this explosion, leaving behind a neutron-rich core of the dead star. The core of that exploded star forms a new neutron star [15]. This new remnant of a supernova contains some incredibly fascinating information. The mass of a neutron star is measured in solar masses $M_\odot$, but the radius is much much smaller than all other stars. Typically they have a radial range of tens of kilometers. The remaining nuclei exude more neutrons out of the nucleus at nuclear drip densities 4×10^{11} g/cm^3, and the neutrons dripped out at this density form a homogeneous system of nuclear matter with other protons and neutrons. The innermost density of a neutron star can go up to 10^{15} g/cm^3. The degeneracy pressure from neutrons and the inter-nucleon interactions prevent the NS structure from another collapse.

1.1.2 Neutron Star Layers

Once it has cooled after the supernova, a neutron star can be divided into five distinct layers [44]. The outer layer forms the atmosphere of the NS, and there are four internal layers, namely the outer crust, the inner crust, the outer core, and the inner core.

The *atmosphere* is the NS's outermost layer, which is where all the electromagnetic radiation is formed (photosphere). Observation of the atmosphere can help determine the surface temperature, surface gravity, magnetic field strength, chemical compositions, and surface geometry. The thickness of this layer varies from a few millimeters to tens of centimeters with the effective surface temperature $T_{\text{eff}} \in [3 \times 10^5\ \text{K}, 3 \times 10^6\ \text{K}]$. It might even be possible to form a solid or liquid atmosphere if the surface temperature of NS becomes sufficiently cold.

The *outer crust* has a thickness of a couple of hundred meters, and it consists of the remaining degenerate electrons e and ions Z after the supernova explosion. The electron degeneracy pressure keeps this layer bound to the internal structure. Deep within this layer, the electron Fermi energy becomes sufficient to start the beta capture process and enriches the neutron fraction as a consequence.

The *inner crust* boundary starts from the region where neutrons starts to drip out of the nuclei. This layer is roughly a kilometer thick, and the density can be half of the saturation density n_0 (0.16 nucleons per fm^3 or 2.3×10^{14} g/cm^3). In all the regions of a neutron star, both e and μ behave as the ideal Fermi gas. At the core-crust boundaries, the nuclei completely dissolve into free neutrons with a mix of free protons, electrons, and muons μ.

The *outer core* has a spread of a couple of kilometers with a density range $n \in [0.5n_0,\ 2n_0]$. All the components in this layer remain in a strongly degenerate state. The composition forms a beta equilibrium with both the beta decay and the inverse electron capture process. This layer accommodates nucleons in a strongly interacting fluid form known as nuclear matter. The nuclear matter is the homogeneous system of neutrons and protons and the saturation density defines the point where this system forms an equilibrium with proton number density n_p and neutron number density n_n.

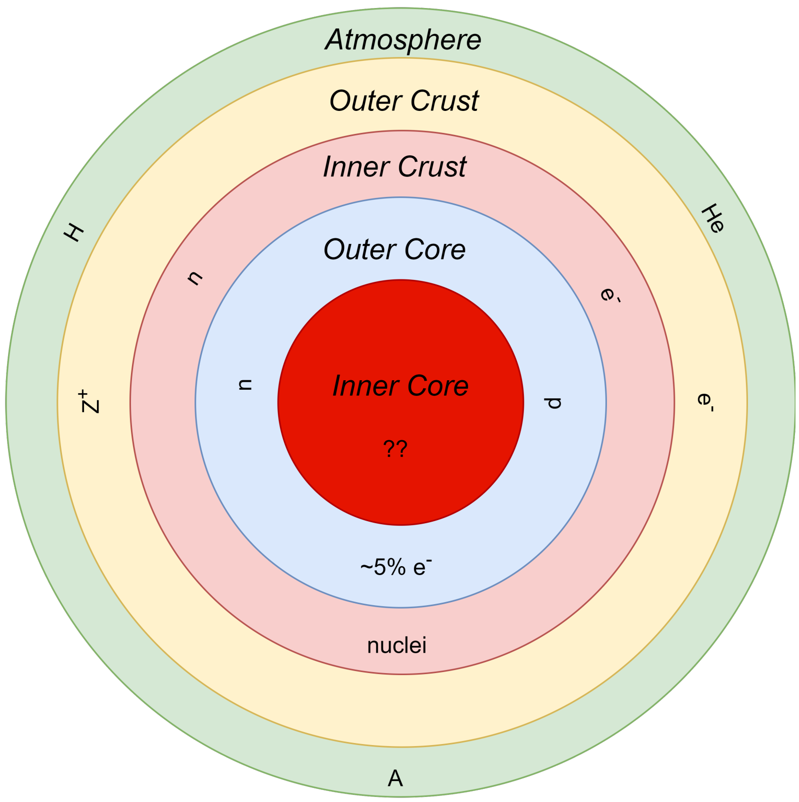

Figure 1.1: Different layers forming a neutron star. Layers in this figure are not to scale.

The *inner core* is the innermost and densest layer of a neutron star. The density in the inner core starts from $2n_0$ and gradually increase towards the center of the star. This layer is formed mainly with nuclear matter, but there also theories with possibilities exotic phenomena such as hyperonization, pion condensation, kaon condensation, and strong phase transition forming self-bound quark matter.

1.1.3 Neutron Star Classifications

Most neutron stars can be classified in two main classes: *isolated* and members of *binary* systems. All *isolated* neutron stars [81] emit some form of electromagnetic radiation, either persistently or intermittently. These radiations are detected in visible, infrared, X-ray and, gamma spectrum. Pulsars got their name from the frequent pulses detected from these types of neutron stars. There are also different classes of non-pulsating NSs. One of these classes of isolated systems is the compact central objects (CCOs) [28, 89] which are weakly magnetized X-ray sources at the center of supernova remnants. Another NS class contains older stars with age between $10^5 - 10^6$ years emitting thermal blackbody X-ray spectra named as the dim isolated neutron stars (DINS) [81].

Binary systems can be found in either wide systems with no exchange of matter in-between or accreting systems with mass transfer to the neutron stars from their companions. NS in wide binaries more or less behave as isolated ones. NS binaries are further defined by their companion stars. High-mass X-ray binaries (HMXBs) [122] have an NS and its companion is a star with a mass range of $2\ \mathrm{M}_\odot - 3\ \mathrm{M}_\odot$. If the companion star has a mass less than solar mass $\mathrm{M}_\odot$; the system is defined as low-mass X-ray binaries (LMXBs) [78]. In HMXB, neutron star is always the low mass entity in the binary and the source of strong X-ray emissions. The massive star in HMXB produces all other thermal emissions. However, neutron star in the LMXB is the high mass object and the X-ray and thermal radiations are emitted from the NS surface.

Pulsars are also observed in exotic triple-star systems. PSR B1620-26 [119] is revolving around a white dwarf and a planetary-mass and, there are pulsar detected with two companion stars forming a triple star system [98].

Radii measurements of isolated neutron stars are challenging and thus have broad systematic uncertainties. Radiations from star surface are mostly used to calculate its radius, but the highly compact neutron star employ gravitational lensing effect on the surface radiation. This lensing effect always add more uncertainties to the radii measurements. Compared to the isolated NSs, NS binaries can provide more accurate radial constraints. Because of the substantial variations in radial ranges, this project excluded radii observations from isolated NSs.

1.1.4 Neutron Star Observables

Masses: NS binaries orbiting in a Keplerian path can be used to measure their masses [4, 56]. The parameters used for these measurements are the orbital period $P_{\rm orb}$, the semimajor axis projection from the pulsar line of sight $x = (a_1 \sin\, i)/c$, the eccentricity e, the time of periastron $T_{\rm p}$, and the longitude of the periastron $L_{\rm p}$. Here, i is the inclination of the orbit, and c is the speed of light. From Kepler's Third Law, the mass function of the binaries can be written as,

$$\frac{(M_{\rm NS}\ \sin i)^3}{(M_{\rm NS}+M_{\rm C})^2} = \frac{P_{\rm orb} v^3}{2\pi G}\,. \tag{1.5}$$

$M_{\rm NS}$ represents the mass of a neutron star and $M_{\rm C}$ is the mass of the companion star.

The orbital velocity projections are calculated from x and $P_{\rm orb}$

$$v = \frac{2\pi a_1 \sin i}{P_{\rm orb}}\,. \tag{1.6}$$

To measure the mass using pulsar timing observations, five post-Keplerian parameters with relativistic corrections have been introduced [110]. These parameters are the rate of periastron motion $\dot{\omega}$, Einstein delay γ due to the gravitational redshift and relativistic time dilation, the decay rate of the orbital period $\dot{P}_{\rm orb}$, range r of the pulses and, shape s of the pulses detected on Earth-based detectors.

$$\dot{\omega} = 3\left(\frac{2\pi}{P_{\rm orb}}\right)^{5/3}\left(\frac{GM_\odot}{c^3}\right)^{2/3}(M_{\rm NS}+M_{\rm C})^{2/3}(1-e^2)^{-1} \tag{1.7}$$

$$\gamma = e\left(\frac{P_{\rm orb}}{2\pi}\right)^{1/3}\left(\frac{GM_\odot}{c^3}\right)^{2/3}\frac{(M_{\rm NS}+2M_{\rm C})M_{\rm C}}{(M_{\rm NS}+M_{\rm C})^{4/3}} \tag{1.8}$$

$$\dot{P}_{\rm orb} = -\frac{192\pi}{5}\left(\frac{2\pi GM_\odot}{P_{\rm orb}c^3}\right)^{5/3}\left(1+\frac{73}{24}e^2+\frac{37}{96}e^4\right) \times (1-e^2)^{-7/2}\frac{M_{\rm NS}M_{\rm C}}{(M_{\rm NS}+M_{\rm C})^{1/3}} \tag{1.9}$$

$$r = \frac{G_\odot}{c^3}M_{\rm C} \tag{1.10}$$

$$s = x\left(\frac{2\pi}{P_{\rm orb}}\right)^{2/3}\left(\frac{c^3}{GM_\odot}\right)^{1/3}\frac{(M_{\rm NS}+M_{\rm C})^{2/3}}{M_{\rm C}} \tag{1.11}$$

Effective surface temperatures: The luminosity L measured from the surfaces of NS in binaries can be used to infer the effective surface temperature $T_{\rm eff}$ [35, 131]. Neutron stars are not true blackbodies. Still, the spectrum coming from the stellar surface can be modified to use in the blackbody radiation relation.

$$L \propto \sigma_{\rm B} R^2 T_\infty^4 \tag{1.12}$$

Here, $\sigma_{\rm B}$ is the Stefan-Boltzmann constant and T_∞ represents the surface temperature measured by the observatories. Like the radius measurements, the surface temperature is also effected by the neutron star's extreme compactness. Removing the redshift contribution from T_∞ provides the desired effective temperature.

$$T_{\rm eff} = \left(1 - \frac{2GM}{Rc^2}\right)^{-1/2} T_\infty \tag{1.13}$$

If the uncertainty on L can be controlled, the above equations will provide good predictions on the NS surface temperature.

Radii: The size and the distance of the observed NSs made radii measurements fairly difficult. There is currently no direct measurement mechanism to get the radius, but thermal emissions from the pulsars can be used to infer the radii. If the distance D of the star is known, the effective radius R_∞ can be calculated using the measured thermal flux F and the effective surface temperature $T_{\rm eff}$. More details about radii measurements are given in section 2.1.

Periods: Most radio pulsars do have a stable pulsation period. Pulsars can be observed in two different classes based on the pulsar timing measurements: normal pulsars with a period of 1 second and those with a period order of milliseconds. The first observed pulsar PSR B1919+21 had a pulsation period of 1.33 s [8], and a millisecond pulsar was discovered in 1982 with a period of 1.558 ms [6]. In 2021, Ref. [101] observed eight new millisecond pulsars ranging from 2.74 to 8.48 ms in globular clusters.

Quasiperiodic pulsations: These pulsations can arise in X-ray binaries from the difference of the rotational frequency of neutron stars with the Keplerian frequency of the innermost stable orbit [123, 82]. Detection of quasiperiodic oscillations might help with the analysis of strong-field general relativity.

Magnetic fields: A rapidly rotating neutron star is believed to power strong magnetic fields [12, 42]. A millisecond pulsar can have magnetic field strength on the order of 10^8–10^9 G [21], where the field strength in normal pulsars might go up to 10^{12} G [87, 94]. There are objects with much higher field strength associated with them, and they are mainly referred to as magnetars. The atmosphere of neutron stars depends on magnetic effects, whereas strong fields might kickstart phase transition within the star.

Glitches: Sometimes, the pulsars can be seen to have a sudden shift of the rotational frequency Ω. This behavior is known as glitches. The first recorded glitches were detected from the Crab [36] and Vela pulsars [100]. Shifts in rotational frequencies are believed to be coming from younger pulsars, and the relative increase of frequencies $\Delta\Omega/\Omega$ are measured be on the order of $10^{-10} - 10^{-6}$.

1.2 Electromagnetic Spectra from Neuron Stars

Neutron stars in accreting binary systems provide significant insight on the NS structure. Although NSs in these systems rotate along their axes, the period of NS determines the analyses that can be done on them. Any neutron star with a rotational period of ~ 1 s can be used in a non-rotating framework and utmost care is necessary to implement the observations from millisecond pulsars in NS models.

All accreting neutron stars binaries emit some form of radiation. The variation of this radiation showed that the X-ray binaries have frequent transitions from *active* to *quiescence* state, and this transition happens back and forth. The companion star, that supplies the NS's accreting material, is typically a white dwarf star in low-mass X-ray binaries. This material piles up within the Roche lobe to form an accreting disk around the neutron star. The accretion process might continue for months to years until the disk becomes hot and dense enough to ionize the falling materials. Ionization changes the viscosity in the disk and initializes a rapid falling process of matter on the NS surface [67]. This process generates an enormous amount of energy which is detected as X-ray outbursts. Detectors have measured these outbursts as high as 1000 times the luminosity of the Sun. These outbursts are referred to as the active state.

Another phase of disk formation starts right after the accretion disk empties enough material onto the NS surface, and the disk becomes significantly cold or by radiating potential energies. This phase of intermittent disk formation is known as the *quiescence* state. During quiescence, neutron stars emit non-thermal radiation from the hot matter in the crust and the core. These radiations are on the order of the luminosity of the Sun [14]. Radiation during the quiescence phase does not contain a varied range of X-ray spectra, and searching these specific bandwidths (approximately $0.5-10$ keV) makes it more efficient to detect quiescent low-mass X-ray binaries (QLMXBs) [51]. The fallen ionized material from the outbursts forms the star's outer envelope, and the materials on this envelope are always arranged in a manner where the lightest element resides on the surface, and heavier ones move inwards. The motion of ions also goes though a chemical diffusion process where the less dense regions of these layers get populated by the mass transport phenomena. Thus the quiescence phase can also be used to determine the atmosphere (H or He) of the neutron star [106].

Some NS binary transients produce X-ray bursts in their active phase. These are labeled as X-ray bursters and subdivided into two different types. Type I bursts are produced by the explosive thermonuclear burning of the accreted matter on the neutron star's surface. In the type II bursters, rapid pulsations were observed along with immense X-ray emissions.

Often the energy released from the type I bursters become sufficient enough to produce luminosity exceeding the Eddington limit, and the radiation pressure will expand the NS atmosphere. The Eddington limit describes the maximum luminosity of a star balancing the outward force from radiation with the gravitational force acting inward.

$$L_{\rm Edd} = 3.2 \times 10^4 \frac{M}{M_\odot} L_\odot \sim 10^{38} \text{ erg s}^{-1} \tag{1.14}$$

Thermal radiation detected from stars are produced in the atmosphere layer. Therefore, this layer is also referred to as the photosphere. Radiation from the photosphere follows the blackbody relation $L \propto R^2 T^4$. The luminosity of the star remains constant ($\sim 10^{38}$ erg s^{-1}) for most of the expansion and contraction phases of the atmosphere. Variation of the temperature T determines the radius R of the photosphere. These types of bursters are named photospheric radius expansion X-ray bursters (PREs) [124].

1.3 Gravitational Waves

Gravitational waves (GWs) are propagating disturbances in spacetime. GW can originate from different oscillation modes (non-radial) of neutron stars.

Also, two massive orbiting or coalescing objects were hypothesized [49] to be the primary sources of powerful and detectable gravitational waves. The first gravitational wave detection from binary black hole merger GW150914 [105] proved the existence of these waveforms. The observation of binary neutron star merger GW170817 [73, 74] includes both the gravitational wave detection and the post-merger photonic emission. This project uses the masses $(m_1,\ m_2)$ and tidal deformations $(\Lambda_1,\ \Lambda_2)$ from the inspiraling neutron stars in GW170817. A brief review of the physics behind gravitational waves is given hereafter.

In the classical theory of gravitation, there are no restrictions on the propagation speed due to the changes in gravitational field. This unconstrained propagation speed aids the developing disturbances to make an immediate impact on other bodies. This contradict the relativistic assertion that no information or disturbances can move with speed larger than the speed of light c. The notion of gravitational waves resulted from Einstein's theory of general relativity (GR) [34] which counters this contradiction from Newton's theory of gravity. Analytical details provided in this section are inspired by the calculations on gravitational radiation in Refs. [59, 83, 104]

The theory of general relativity operates on a four-dimensional manifold. All points occupying this manifold are referred to as events, and each event is labeled with a four-vector x^μ $(\mu = 0, 1, 2, 3)$. The zeroth coordinate in these four vectors represents time $x^0 = ct$ and the rest are assigned with the three-dimensional spatial coordinates. If there are possible interactions between two events x^μ and x^ν, the distance connecting them are defined as

$$ds^2 = g_{\mu\nu} dx^\mu dx^\nu \tag{1.15}$$

This quantity $g_{\mu\nu}$ is a symmetric tensor called the metric tensor used to describe all critical measures in GR. Special relativity does not explicitly use spacetime curvatures. Under this consideration, the four-fold manifold is described as Minkowski space, and the associated metric becomes,

$$g_{\mu\nu} = \eta_{\mu\nu} = \begin{pmatrix} -1 & 0 & 0 & 0 \\ 0 & 1 & 0 & 0 \\ 0 & 0 & 1 & 0 \\ 0 & 0 & 0 & 1 \end{pmatrix} \tag{1.16}$$

However, in general relativity, massive objects tend to bend the fabric of spacetime and the Riemann tensor $R_{\alpha\beta\mu\nu}$ quantifies the amount of bending. Riemannian geometry stipulates a condition $\nabla_\gamma g_{\mu\nu} = 0$ for all curves and vector fields. This divergence condition on the metric provides some uniquely determined coefficients $\Gamma^\gamma_{\mu\nu}$, known as Christoffel symbols, for a given metric.

$$\Gamma^\gamma_{\mu\nu} = \frac{1}{2} g^{\gamma\delta} \left(\partial_\mu g_{\delta\nu} + \partial_\nu g_{\mu\delta} - \partial_\delta g_{\mu\nu} \right) \tag{1.17}$$

The Riemann tensor can be represented by the Christoffel symbols as well.

$$R^\alpha_{\beta\mu\nu} = \partial_\mu \Gamma^\alpha_{\beta\nu} - \partial_\nu \Gamma^\alpha_{\beta\mu} + \Gamma^\alpha_{\sigma\mu}\Gamma^\sigma_{\beta\nu} - \Gamma^\alpha_{\sigma\nu}\Gamma^\sigma_{\beta\mu} \tag{1.18}$$

Einstein's theory of general relativity relates the mass distribution in the gravitational field with the spacetime curvature from massive bodies. The stress-energy tensor $T_{\mu\nu}$ serves the purpose of mass-energy distribution in the relativistic case, and a limiting case of $T_{\mu\nu}$ is used to calculate the neutron star structure in section 2.6.

$$G_{\mu\nu} \equiv R_{\mu\nu} - \frac{1}{2}g_{\mu\nu}R = \frac{8\pi G}{c^4}T_{\mu\nu} \tag{1.19}$$

Here, $R_{\mu\nu}$ is the contracted form of Riemann tensor $g^{\alpha\beta}R_{\alpha\beta\mu\nu}$, also known as the Ricci tensor, and $R = g^{\mu\nu}R_{\mu\nu}$ is the scalar curvature or Ricci scalar. Equation 1.19 provides the necessary relation between Einstein's gravitational field $G_{\mu\nu}$ with the spacetime curvature and the distribution of matter and radiation in the universe. A scalar curvature implies that the vanishing of R represents a spacetime that is free of massive objects and the spacetime is nearly flat. Thus the Riemann tensor will solely determine the gravitational wave propagation in empty space. According to Einstein's relation, any change in the matter distribution $T_{\mu\nu}$ will induce fluctuations far away in gravitational filed or the flat metric $\eta_{\mu\nu}$. The perturbed metric is given in terms of the variation $h_{\mu\nu}$,

$$\tilde{g}_{\mu\nu} = \eta_{\mu\nu} + h_{\mu\nu} \tag{1.20}$$

Solving Einstein's equations to calculate this new metric is a different challenge of it's own. For weak gravitational fields, assuming this perturbation to be small enough $|h_{\mu\nu}| << 1$ can provide a proper analytical solution. With this limiting case, only the linear terms of $h_{\mu\nu}$ are included in $\tilde{g}_{\mu\nu}$. This limiting solution is referred to as the *linearized theory* of gravitational waves. The Minkowski metric is symmetric in its covariant and contravariant form, which provides the metric identity.

$$\eta_{\mu\nu}\eta^{\mu\sigma} = \delta^{\sigma}_{\nu} \tag{1.21}$$

The inverse of perturbation metric $\tilde{g}_{\mu\nu}$ can be found using the above identity.

$$\tilde{g}^{\mu\nu} = \eta^{\mu\nu} - h^{\mu\nu} \tag{1.22}$$

The above equation holds for a weak field assumption and neglecting all $\mathcal{O}(h^2)$ and higher order terms from $h^{\mu\nu}$. Einstein showed that a metric perturbation could formulate a wave equation similar to electro-magnetism with an appropriate gauge. The perturbed metric used by Einstein is,

$$\bar{h}_{\mu\nu} \equiv h_{\mu\nu} - \frac{1}{2} h \eta_{\mu\nu} \tag{1.23}$$

where $h = \eta^{\mu\nu} h_{\mu\nu}$. Trace of $\bar{h}_{\mu\nu}$ yields $\bar{h} = -h$, and it can be used to invert Eq. 1.23. If one recalculates the Christoffel symbols with the perturbed metric and put them back in the Riemann tensor, only the $h_{\mu\nu}$ contributions will persist.

$$R_{\alpha\beta\mu\nu} = -\delta_\mu \delta_{[\alpha} h_{\beta]\nu} + \delta_\nu \delta_{[\alpha} h_{\beta]\mu} \tag{1.24}$$

With this modification and computing new Ricci tensor and scalar curvature, Einstein's equation will reduce to

$$\Box \bar{h}_{\mu\nu} - 2\delta^\sigma \delta_{(\mu} \bar{h}_{\nu)\sigma} + \eta_{\mu\nu} \delta^\mu \delta^\nu \bar{h}_{\mu\nu} = -\frac{16\pi G}{c^4} T_{\mu\nu} \tag{1.25}$$

where, the wave operator or d'Alembertian is defined as $\Box \equiv \eta^{\mu\nu} \delta_\mu \delta_\nu$. Equations 1.24 and 1.25 used two identities related to symmetrization and anti-symmetrization of pair indices.

$$A_{[ab]} \equiv \tfrac{1}{2}(A_{ab} - A_{ba}) \tag{1.26}$$

$$A_{(ab)} \equiv \tfrac{1}{2}(A_{ab} + A_{ba}) \tag{1.27}$$

It is required to find a gauge under which the divergence of $\bar{h}_{\mu\nu}$ vanishes, such as the Lorenz gauge condition $\delta^{\sigma}\bar{h}_{\mu\sigma} = 0$, which in terms yield a linearized Einstein's equation.

$$\Box\bar{h}_{\mu\nu} = -\frac{16\pi G}{c^4}T_{\mu\nu} \tag{1.28}$$

The above equation is equivalent to the electromagnetic wave equation where stress-energy tensor $T_{\mu\nu}$ behaves as the source for gravitational waves.

1.3.1 Interaction with Matter

A propagating gravitational wave has two different polarization states perpendicular to the direction of propagation x^k. Usually, these states are described in a transverse-traceless (TT) gauge.

$$\bar{h}^{TT}_{\mu\nu} = \begin{pmatrix} 0 & 0 & 0 & 0 \\ 0 & h_{+} & h_{\times} & 0 \\ 0 & h_{\times} & -h_{+} & 0 \\ 0 & 0 & 0 & \end{pmatrix} \tag{1.29}$$

The linearized GW is analogous to a spin-2 particle with helicity $h_{+} \pm ih_{\times}$. These polarization states induce an oscillating tidal field along with the spatial directions x^i and x^j while passing through matter. The h_{+} state determines the amplitude of oscillations along these coordinates, and the $h_{\times}$ polarization determines the fluctuations along the diagonal. Matter interaction with the tidal field allows one to measure the strength of incoming and outgoing gravitational waves. The total amplitude h is related to the quadrupole moment Q of the source and inverse of time ω. For a gravitational wave source of mass M and radius R, the amplitude measured at a distance of r is

$$h \sim \frac{2G}{c^4 r}\omega^2 M R^2 \tag{1.30}$$

The typical amplitude of h varies from 10^{-22} to 10^{-20}. Coalescing binary neutron stars at distant galaxies will produce GW with an amplitude of 10^{-22}. At the time of detecting merger event GW170817, the strain sensitivity of the LIGO-VIRGO was around 10^{-20}, which was planned for an upgrade in version three of their detectors. The flux of energy F carried by the gravitational waves is calculated by averaging over the polarization states.

$$F = \frac{c^3}{16\pi G}\left\langle \dot{h}_+^2 + \dot{h}_x^2 \right\rangle \sim \frac{c^3}{32\pi G} f^2 h^2 \tag{1.31}$$

Equation 1.31 relates GW strength with typical frequency f and amplitude h. The frequency range of GW from coalescing neutron stars will vary in-between $0.1 - 2$ kHz, and the flux will be in the order of milliwatts per meter squared. These wave signatures provide necessary constraints to correctly classify an event, whether the GW is produced from a black hole-black hole (BH-BH), a black hole-neutron star (BH-NS) or, a neutron star-neutron star (NS-NS) merger.

1.4 Phenomenological Constraints

Neutron star research can be divided into two distinct eras, pre- and post-discovery of pulsars. In the pre-discovery phase, theoretical predictions were made about a compact star denser than the white dwarf. Surprisingly, the first model of these highly dense objects was formulated by Lev Landau [64] in 1931, a year before Chadwick discovered the neutron [23]. Landau proposed a compact star configuration more dense than the white dwarf, which might resemble a giant nucleus. As this model did not contemplate the existence of the neutron, this configuration fell short of describing stars with maximum mass beyond 1.5 $M_\odot$. In 1934, W. Baade and F. Zwicky [5] made the first theoretical prediction of neutron stars. Their work on describing the immense energy release in supernovae predicted that the exploding star would transform into a neutron star at its final stage.

Oppenheimer and Volkoff [88] constructed the first mass model of a neutron star in 1939. They solved Einstein's equation for a spherically symmetric star (Tolman published an independent solution [121]) and numerically calculated the maximum mass of a neutron star is around 0.71 $M_\odot$. This mass limit was much lower than the Chandrasekhar [24] mass limit of white dwarfs 1.44 $M_\odot$. Oppenheimer and Volkoff selected a relatively simple equation of state with a non-interacting strongly degenerate neutron gas, and this deviation from the Chandrasekhar limit is a consequence of that. Their work provided evidence that the strong interaction of nuclear matter highly influence the maximum value of a neutron star mass $M_{\max}$ and a realistic equation of state should incorporate such interactions.

Hereafter, most of the neutron star research was focused on associating reliable and reasonable physics with the EOS. Enforcing the beta equilibrium condition for electrons, protons and, neutrons [20] with the Skyrme-type short-range nucleon-nucleon interactions [109] in the EOS, advance the minimum value of the maximum mass NS close to 2 $M_\odot$. This value of $M_{\max}$ is still used to determine whether an EOS can reliably predict the neutron structure. Any EOS that failed to achieve this maximum mass gets discarded. Also, the radius calculated by solving the Tolman-Oppenheimer-Volkoff equations with EOSs that support 2 $M_\odot$ sets the lower bound of R to 8 km and an upper bound of 20 km. The role of neutrinos in neutron star cooling [7] was another development done right before the discovery of the neutron star.

The first radio pulsar was discovered by Bell and Hewish [53] in 1967 but, the first precise mass measurement of a pulsar was done by Hulse and Taylor [56] on PSR B1913+16. They measured the mass of this pulsar to be 1.4408 ± 0.0003 $M_\odot$ and many subsequent pulsar measurements have clustered around this value. In the post-discovery era, neutron star research was more inclined to constrain radii of NSs. Mass measurements from the millisecond pulsars in globular clusters are used to make better estimates on the radial limits. Heinke et al. [52] measured the radius of NS X7 in the globular cluster 47 Tuc, assuming a mass of 1.4 $M_\odot$ to be [12.9, 16.3] km with 90% confidence limit. Bogdanov et al. [13] found the radius of the same neutron star to be 10.4 to 11.9 km with a 68% confidence limit. The variation in these two radial ranges of neutron star X7 proves that the radii measurements are highly model-dependent. Using eight QLMXB observations from different globular clusters, Steiner et al. [112] found the radii of a 1.4 $M_\odot$ neutron star within 10 to 14 km with a 95% confidence limit. Mass measurements of X-ray bursters can also be used to infer neutron star radius. Özel et al. [132] used 12 neutron star observations to bound the radial limit in-between 10.1 to 11.1 km for a 1.5 $M_\odot$ NS. It is evident from these references that combining multiple observations allows one to calculate better radial constraints.

In 2017, the first gravitational wave signal was detected from a binary neutron star merger [73]. For a low spin prior, this observation GW170817 made precise measurements of the chirp mass $\mathcal{M} = (m_1 m_2)^{3/5}/(m_1 + m_2)^{1/5} = 1.188^{+0.004}_{-0.002}$. Here, m_1 and m_2 are individual masses in the NS-NS binary. GW170817 also provides direct measures of neutron star tidal deformabilities due to the tidal force from its companion.

Most of the current NS models are built upon the $M_{\rm max}$ constraint of 2 $M_{\odot}$, but a couple of recent pulsar measurements showed the existence of neutron stars beyond this mass limit. The mass measured from PSR J2215+5135 [76] is $2.27^{+0.17}_{-0.15}$ $M_{\odot}$, and MSP J0740+6620 [26] has a mass of $2.14^{+0.1}_{-0.09}$ $M_{\odot}$. It implies the necessity of updating current EOSs so that the neutron star models can incorporate larger value of maximum mass.

1.5 Project Motivations

Beyond the year 2000, X-ray astronomy has commenced more missions to find precise measures from distant neutron stars. These new incoming data from observations also triggered rapid advancements in the field of theoretical astrophysics. The objective here is to work in sync with all relevant fields such as low energy nuclear physics (experiments and theory), high energy physics (also both experiments and theory), observational astronomy, and last but not least the theoretical astrophysics to obtain

"One true mass-radius curve of neutron stars."

The aim for the first part of this project was to include different observations to build a uniform model and test the impact of these new data on neutron star radii measurement. This work was inspired by the analyses done on QLMXBs [112] and PREs [86] to measure the mass-radius distribution for each NS source. Alongside these NSs, mass measurements from NS-NS binary merger GW170817 [75] and

PSR J0030+0451 [102] were added to the combined dataset. The low-density part of the equation of state ($n < 2n_0$) was parameterized by the results from Quantum Monte Carlo simulations, and a Skyrme-type fit was used to implement nuclear experiment results. In the high-density regime of nuclear matter, two different extrapolation method was used. Overall, eight different models were simulated combining two EOS prior with four combinations of observational datasets. These simulations are structured to perform a Bayesian inferences with the Markov Chain Monte Carlo method. Each source of the neutron star observations used in this project was treated as uncorrelated data points in those simulations. The resultant mass-radius distributions showed apparent dependencies on the prior choice of the equation of state. These distributions also inferred a more stringent limit on radii, compared to the limits given in the previous section, for NSs with the canonical mass 1.4 $M_\odot$.

It was hypothesized that the mass-radius constraints from the spectral data are not entirely free of background noises. Thus, they might contain some hidden uncertainties that are yet to be uncovered. Two of the models presented in this dissertation were built to test this hypothesis. In these models, a simple convolution operation (named intrinsic scattering) was performed on the spectral data and, these new datasets were used for the simulation.

Data from GW170817 provided a testbed for a set of binary parameters of neutron stars. The deformation of the star surface due to the tidal force can be measured directly. This tidal deformation Λ is related to the radii of the neutron stars. Thus, a measure of individual Λ's in the binary can be used to infer structural properties as well. The intention of simulating tidal deformability was to test the influence of X-ray data on constraining this quantity. This project also performed tests on a couple of approximately universal relations for NS binaries.

These universal relations demonstrated that the antisymmetric contribution of tidal deformabilities $\Lambda_{\mathrm{a}} = \Lambda_2 - \Lambda_1$ [130], mass ratio $q = m_1/m_1$ of the NSs in binaries [27] and, the individual compactness $C = M/R$ [80] are primarily independent of the equation of state prior. This part of the tests was performed to quantify the variation of these EOS independent quantities with the simulated ones. Lastly, two correlation analyses were done to test the dependencies of radius R on EOS parameters and the minimum value of maximum mass M_{max}.

The computation cost for simulating all these models was expensive. The central expenses were to get equilibrated Markov chains and, discarding all points that are correlated to each other. An ideal simulation has to have true randomness, which means that the simulated points should be uncorrelated. The complexity of correlation analysis becomes large with a more extensive parameter set. Although a crude calculation on correlation analysis was performed during this project, a better estimate of correlation needs to be included in these model analyses. Implementing emulators should be a simple way around this, as this is computationally cheaper. Emulators can also be used to update established models with new observations. With emulators, it will not be necessary to simulate new models with all of the NS sources. Successful implementation of emulators will drastically reduce the complexity of simulations mentioned earlier.

In recent years, more and more neutron stars with masses larger than 2 $\mathrm{M}_{\odot}$ are being discovered. As the maximum mass of a neutron star is EOS dependent, an updated variant of EOS is needed to describe these massive NSs. Rather than using the EOS parameters, the hypothesis here is to formulate a inverse relation with M_{max} with EOS parameters and use M_{max} as a free parameter in model simulations.

The final part of this dissertation, currently in progress, involves analyzing non-radial pulsations of neutron stars. The fundamental mode (f-mode) of neutron star oscillation is identified as a carrier of gravitational wave signatures [25, 126]. The goal of performing f-mode analyses is to get a relationship between the compactness of the star and the frequency of oscillation, similar to Ref. [30], with the EOS mentioned above, and test the correlations between the f-mode and tidal deformabilities [54].

Chapter 2

Neutron Star Models and Simulations

In an ideal case, all of the neutron star observables mentioned in 1.1 should be included while constructing an NS model. This task needs to be done with care. Most of these observables are riddled with considerable systematic uncertainties and, these uncertainties are getting updated with successive observations. The current project presented here used a selective group of observables and various NS observations to properly constrain the mass-radius (M-R) relation of an NS.

2.1 Observational Dataset

Firstly, a joint dataset is compiled with mass-radius constraints from low mass X-ray binaries (QLMXBs), photospheric radius expansion X-ray bursters (PREs), and an additional observation from NICER. The LIGO-VIRGO observation of neutron star binary merger GW170817 does not put direct constraints on NS radii but, the masses are well constrained, data from GW170817 is also included here.

The joint dataset comprises seven QLMXBs from globular clusters 47 Tuc (X7), ω Cen, NGC6397, NGC6304, M13, M28, and M30. References [112, 108] provide spectral data for NS masses and their corresponding radial constraints. Radii measurements of NSs are complicated but, the effective radius can be obtained by the observed X-ray flux F, temperature T, and the distance D.

$$R_\infty = \sqrt{\frac{FD^2}{\sigma_\mathrm{B} T^4}} \tag{2.1}$$

Here, σ_B is the Stefan-Boltzmann constant. R_∞ is the radius of the star observed by the detector from a large distance. The outgoing spectra can be affected by gravitational lensing due to the compactness of the neutron star. Actual radius R is obtained by removing the gravitational redshift z from R_∞. Defining the redshift (in natural units, $G = c = 1$) as

$$z = \left(1 - \frac{2M}{R}\right)^{-1/2} - 1, \tag{2.2}$$

the radius and mass of the star can be parameterized by

$$R = \frac{R_\infty}{(1+z)} \tag{2.3}$$

$$M = R_\infty \left[\frac{z(2+z)}{2(1+z)^3}\right] \tag{2.4}$$

Mass-radius information and the source properties from the binaries mentioned above can be found in Ref. [84]. Most binaries used in this project came from the observations of globular clusters. Nearly 10% of the observed LMXBs can be found in globular clusters. Choosing NS binaries from the globular clusters can be beneficial as their distances are constrained with well-known systematic uncertainties [128]. In contrast, it is hard to measure distances to

LMXBs, although the Gaia mission is making headway. The accretion process and the interactions in the NSs that reside in globular clusters are also well documented [9]. Also, their spectra coming from the thermal surface has little to no power-law component, allowing one to consider uniform temperature distribution throughout the star's surface. These spectral data also provide information on NS atmospheres. The current project includes mass-radius inferences considering both H and He atmospheres with a specific weight to each of them. The choice of atmospheric data in use, either H or He, defines the atmospheric prior and the results from different atmospheric priors can be seen in Fig. 2.1.

Mass-radius inferences from photospheric radius expansion X-ray bursters named as SAX J1810.8-429, 4U 1724-307 [85], and 4U 1702-429 [84] are also added to the dataset. The NICER mission recently published thee M-R constraints from pulsar observation of PSR J0030+0451 [102, 93] and, these results are also integrated into the current dataset. Figure 2.2 provides an example of M-R distribution from a PRE source along with the NICER observation. A couple of variable transformations had to be done to obtain the mass information from GW170817 NS-NS binary merger. There is no direct evidence on the radius from this measurement, but a strong constraint on tidal deformability $\tilde{\Lambda}$ is provided. This result from the LIGO-VIRGO collaboration [74, 75] is published with chirp mass $\mathcal{M}$ and mass ratio q,

$$\mathcal{M} = \frac{(m_1 m_2)^{3/5}}{(m_1 + m_2)^{1/5}} \tag{2.5}$$

$$q = \frac{m_2}{m_1} \tag{2.6}$$

Here, m_1 and m_2 represent the mass of the NSs in the binary.

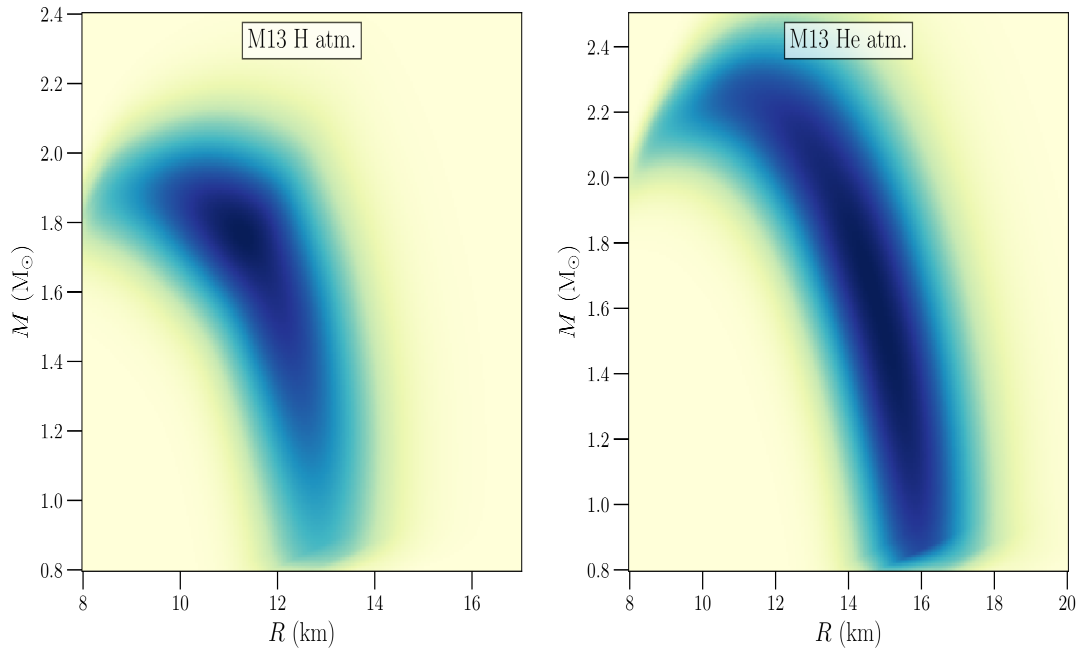

Figure 2.1: The M-R distributions for binares in M13 cluster. Figure in the left is generated with a H atmosphere prior and, the right side plot represents the He atmosphere.

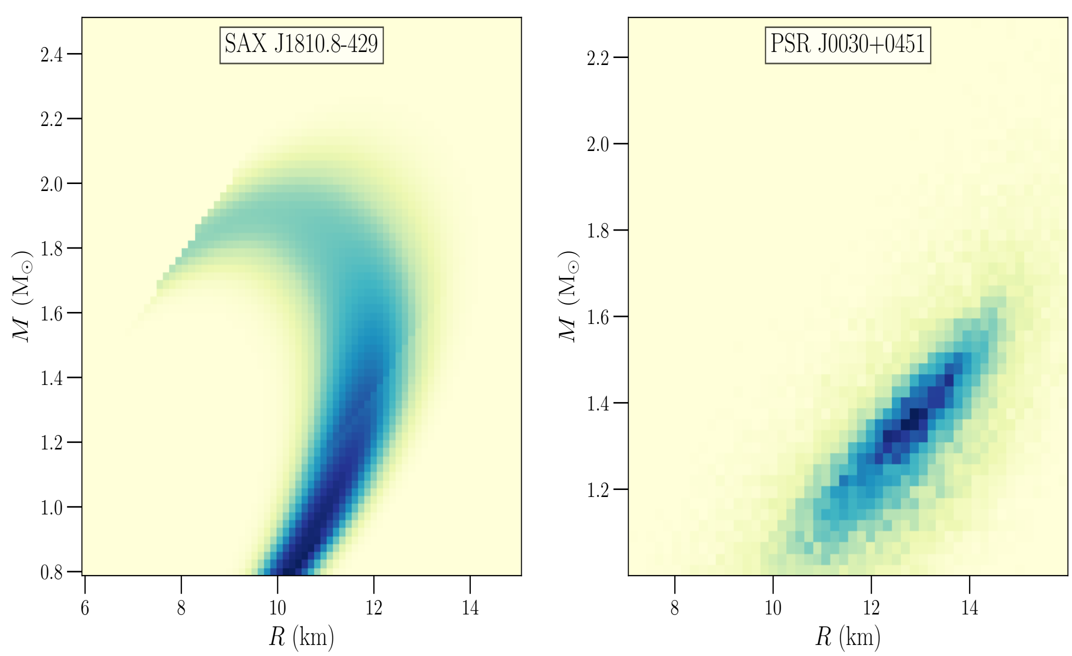

Figure 2.2: Figure in the left demonstrates the mass-radius relation from SAX J1810.8-429, a photospheric radius expansion x-ray burster. The other figure provides the M-R constraint of PSR J0030+0451.

It was favorable to use the symmetric mass ratio η instead of q to avoid the mass ratio boundaries of m_1 and m_2.

$$\eta = \frac{m_1 m_2}{(m_1 + m_2)^2} \tag{2.7}$$

Furthermore, $\tilde{\Lambda}$ is given as the symmetric combination from the individual deformabilities (Λ_1, Λ_2) and their corresponding masses.

$$\tilde{\Lambda} = \frac{16}{13} \frac{(m_1 + 12m_2)\, m_1^4 \Lambda_1 + (m_2 + 12m_1)\, m_2^4 \Lambda_2}{(m_1 + m_2)^5} \tag{2.8}$$

A redshift correction had to be applied on the detector frame chirp mass $\mathcal{M}_{\mathrm{det}}$ to get $\mathcal{M}$.

$$\mathcal{M} = \frac{\mathcal{M}_{\mathrm{det}}}{1 + z} \tag{2.9}$$

Distribution for the LIGO data is interpolated from a 3-dimensional grid of these parameters with corresponding likelihood at each grid point. Lastly, a total conditional probability for this joint analysis is formed using the LIGO data D_{LIGO} and X-ray source data D_{i}.

$$\begin{aligned} \mathcal{P}(D|M) \quad &= \quad D_{\mathrm{LIGO}} \left[\mathcal{M}_{\mathrm{det}}(m_1, m_2, z), \eta(m_1, m_2), \tilde{\Lambda}(m_1, m_2, \{p\}) \right] \\ &\quad \times \prod_{\mathrm{i}}^{\mathrm{N}} D_{\mathrm{i}}[R(m_{\mathrm{i}}, \{p\}), m_{\mathrm{i}}, \zeta_{\mathrm{i}}, \sigma_{\mathrm{i}}] \end{aligned} \tag{2.10}$$

Here, $\{p\}$ is the set of EOS parameters, ζ is the binary parameter to select NS atmosphere, σ is the uncertainty, and N represents the number of spectral sources used in our models.

2.2 Probability distribution of GW170817 Data Using KDE

Observed data from the binary NS merger GW170817 is publicly available in the LIGO-VIRGO repository. This dataset has individual masses and their respective tidal deformabilities from the inspiraling neutron stars. Six other parameters determine the sky position of the event, which are not relevant for this project. The drawbacks of the GW170817 public data are that the information is not presented in a functional form, and the number of sample points, about 4000, does not create a dense enough grid for the simulation. An alternative approach uses a density estimator and generates the desired number of grid points from the density function with the associated probabilities.

Density estimation is the process of constructing a probability density function (PDF) from a given data set. The function used in the estimator is referred to as kernel. Kernel $k(x; h)$ is a function of given data x and some additional hyperparameters hs. This k function calculates the relation between the points in provided dataset. The kernel hyperparameters are free parameters of the function and does not get optimized from the data. These parameters are optimized externally. The generic form of a kernel density estimator (KDE) is given as,

$$\mathcal{P}_{\mathrm{KDE}}(x) = \frac{1}{nh} \sum_{i=1}^{n} K\left(\frac{x - \mu_x}{h}\right) \tag{2.11}$$

Here, $\mathcal{P}_{\mathrm{KDE}}(x)$ if the PDF with n data points for variate x. K is the kernel function with a hyperparameter h, also referred to as the bandwidth. A hyperparameter is a parameter that is not set by the given data. Generally, the hyperparameter determines the smoothness of the kernel function. By definition, a kernel function has to be smooth and symmetric over the median μ_x. Also,

$$\int_{-\infty}^{\infty} k(x)dx = 1 \text{ and,} \tag{2.12}$$

$$\lim_{x\to\pm\infty} k(x) \to 0. \tag{2.13}$$

Any function that satisfies Eqs. 2.12 and 2.13 can be used as a kernel. This project used a Gaussian kernel $k(x;h) \propto \exp\left(-x^2/2h^2\right)$ and the KDE implementation in the Scikit-learn [90] machine learning package. There are several methods to find the best value of the bandwidth. For the GW170817 dataset, an extensive grid search was performed to find the best bandwidth. Scikit-learn has a search method named "GridSearchCV" (GCV), which is used for hyperparameter optimization. GCV was given the range $[0.1, 1]$ for h and, it calculated the score for each point in this interval. The final output from GCV returns the best fit model for KDE with the optimized value of h. The trained KDE model has a method called "score", and it will return the probability for a given set of variate values. Before generating the PDF, the neutron star parameters m_1, m_2 Λ_1 and, Λ_2 were converted to $\mathcal{M}$, q and, $\tilde{\Lambda}$ using Eqs. 2.5, 2.6 and, 2.8. A KDE model was trained using parameters $\mathcal{M}$, q and, $\tilde{\Lambda}$. Also, a three-dimensional grid with dimensions $40 \times 40 \times 40$ was made for these three parameters. The range of each axis runs from the minimum to the maximum value for its respective parameter, which is acquired by the parameter conversion process. This grid was supplied to the trained KDE model and KDE generates probabilities for each grid point. The grid and the associated probabilities are stored in a tabular format for easy access in the simulations. A density plot given in Fig. 2.3 shows the values of $\mathcal{M}$, q and, $\tilde{\Lambda}$. The normalized color bar represents the probabilities.

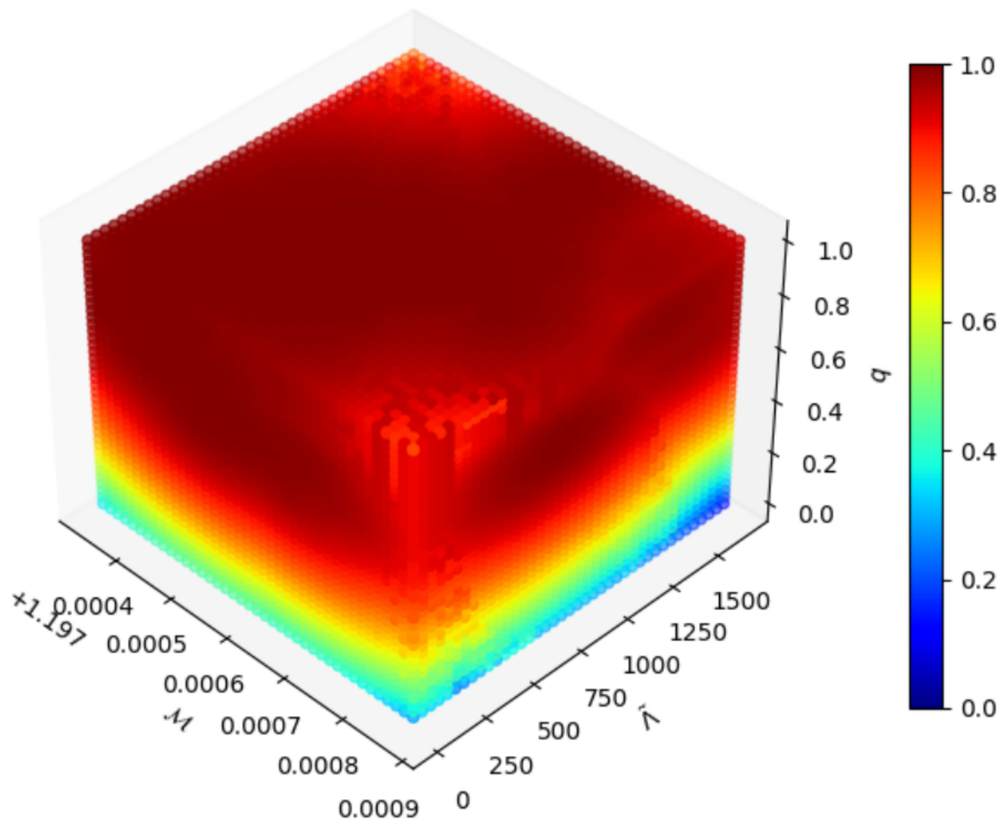

Figure 2.3: The probability density grid with chirp mass $\mathcal{M}$, mass ratio q and, tidal deformability $\tilde{\Lambda}$ from GW170817. The density is normalized between 0 and 1 with 0 being the lowest probability and 1 being the highest.

The posterior distributions relating these binary parameters, $\mathcal{M}$, q and $\tilde{\Lambda}$, are given in Appendix A. Figure 2.3 has some noisy points around low $\tilde{\Lambda}$ and high $\mathcal{M}$. The possible cause of this noise might be the number of sample points used to train the KDE.

2.3 Intrinsic Scattering of EM Spectra

A large amount of background noise is associated with raw spectral data. The published constraints from neutron star sources went through a rigorous denoising process. The authors in Ref. [86] assumed some hidden uncertainties in X-ray bursts cooling observations and proposed an intrinsic scattering (IS) method to further denoise the spectra. The current project adopted this IS method and applied an additional filter on the X-ray data.

The IS method uses a modified version of the Gaussian blurring process, usually used in image processing services. The Gaussian blur effect softens the texture of the image but keeps the boundaries intact. This softening effect removes any distinct shift between the data bins, and the outcome of this filter should reveal new centroid values (mean and variance).

There are several different algorithms to implement image blurring, but this project took advantage of the Gaussian kernel filter algorithm. This filter performs a convolution operation on the target data using a Gaussian function G. The variance σ referred to as the smoothing parameter is treated as a free parameter here. For two-dimensional input data, the function is defined as the normal distribution.

$$G(x, x^{'}, y, y^{'}) = \frac{1}{2\pi\sigma^2} \exp\left\{-\frac{(x-x^{'})^2 + (y-y^{'})^2}{2\sigma^2}\right\} \tag{2.14}$$

Here, the term $1/2\pi\sigma^2$ is the normalization factor. For the mass-radius data, the mass variance σ_M and the radius variance σ_R were generated by multiplying appropriate weights for different axes with this σ parameter.

$$\sigma_M \equiv (1.4\mathrm{M}_\odot)\sigma \tag{2.15}$$

$$\sigma_R \equiv (5\mathrm{km})\sigma \tag{2.16}$$

It is desirable to treat both σ_M and σ_R as free parameters, but more free parameters mean a significant computation cost increase. Generating the filters for the grid points is also a costly process. The smoothing effect mostly depends on how many nearest neighbors were selected for the target grid point. Applying this filter to the spectra produces new data for further analysis.

$$D_{IS}(R,M) = \int_{M_0}^{M_1}\int_{R_0}^{R_1} dR^{'}dM^{'}\,D(R^{'},M^{'})\;G(R,R^{'},M,M^{'}) \tag{2.17}$$

2.4 Quantum Many Body Problem

A neutron star can be considered as a many-body quantum system. Like any quantum system, the internal constitutes of the star will form minimum energy configurations among layers. Hence, the microphysics within the star will be governed by quantum statistics. The challenge in these quantum many-body systems is to find an accurate solution to the Schrödinger equation. If these particles are assumed to be non-relativistic, the Born-Oppenheimer Hamiltonian for the many-body system is given as,

$$\hat{H} = -\frac{1}{2}\sum \nabla_i^2 - V \tag{2.18}$$

Here, the first term in Eq. 2.18 is the kinetic part, and V represents the potential of the system. The form of this potential can be defined in a various manner depending on the system in concern. The goal hereafter is to find the eigenvalues and the eigenvectors of this Hamiltonian. The complexity of finding a solution grows exponentially with an increasing number of constituents. There are several well-established methods to tackle large quantum systems. The Hartree-Fock method, random phase approximation, many-body perturbation theory, Green's function method, density functional theory and, quantum Monte Carlo methods are some of the most popular approaches for minimizing the quantum many-body system. There is no definite rubric to measure the best approach from the methods mentioned above. This project used Quantum Monte Carlo simulation results, which were previously used to build successful neutron star models.

2.5 EOS Parametrization

An equation of state based on the nucleonic (proton and neutron) interactions can be used to generate an overall relationship between the pressure P and the mass density ρ of the star. If required, ρ can easily be substituted with energy density ϵ.

$$\rho(n) \rightarrow \epsilon(n) \rightarrow P(n) \tag{2.19}$$

All these quantities are functions of the total baryon number density n while, $n = n_{\mathrm{p}} + n_{\mathrm{n}}$ is given in terms of proton and neutron number densities ($n_{\mathrm{p}},\ n_{\mathrm{n}}$). Any system comprised of an idealized medium of interacting nucleons with uniform density is known as nuclear matter. In highly dense objects like neutron stars, their cores could go far beyond the saturation density of nuclear matter n_0. Modern experiments can test EOSs up to two saturation densities in the lab environment, but an extensive amount of theoretical work can be found in the literature with systematics to describe densities beyond $2n_0$. The high-density EOS is parameterized by extrapolation methods (i.e., two polytropes, three polytropes, etc.). Naturally, these simulated EOSs have to be validated with the experiments in low-density regions. This current project incorporates two different ways to parameterize the EOS. Both EOS descriptions contain data acquired from Quantum Monte Carlo simulations for $n = [0, 2n_0]$ and results obtained from the Skyrme fitting with experiments (at proton fraction $x = 1/2$) but differ in extrapolation schemes.

As mentioned in the previous section, Quantum Monte Carlo (QMC) methods solve quantum many-body systems. Here, a variation of the Auxiliary Field Diffusion Monte Carlo (AFDMC) method is implemented. This method was demonstrated in [41], which is also described as Gandolfi-Carlson-Reddy (GCR) model. This model defines a functional which parameterizes the energy density for pure neutron matter (PNM),

$$E_{\mathrm{PNM}}(n_{\mathrm{B}}) = a\left(\frac{n_{\mathrm{B}}}{n_0}\right)^{\alpha} + b\left(\frac{n_{\mathrm{B}}}{n_0}\right)^{\beta} \tag{2.20}$$

The above equation defines energy per particle as a function of nuclear matter density. Reference [111] provides a precise limit for parameter a and α, 12.5 Mev $< a <$ 13.5 MeV and $0.47 < \alpha < 0.53$. The first term in Eq. 2.20 corresponds to two-nucleon interactions and the second term defines the three nucleonic parts. For symmetric nuclear matter (i.e. x=1/2, where $x = \frac{n_{\mathrm{p}}}{n_{\mathrm{p}}+n_{\mathrm{n}}}$ is the proton fraction), the symmetry energy S relates to a and b as,

$$S = a + b + 16 \tag{2.21}$$

The other two free parameters b and β in Eq. 2.20 can be parameterized using the slope L of the symmetry energy.

$$L = 3(a\alpha + b\beta) \tag{2.22}$$

29.5 MeV $< S < 36.1$ MeV and 30.0 MeV $< L < 70.0$ MeV provide an exhaustive range for these parameters with the additional constraint on a and α given above.

The Skyrme model is an efficient method to describe density-dependent nucleonic interaction in nuclear matter near saturation density. This model determines the non-relativistic zero range interactions of nucleons using Hartree-Fock calculations. One limitation of using the Skyrme model is that the validity of the range is relatively short, $0.01n_0 - 3.0n_0$, in terms of NS EOS. Therefore, it was employed only for the low-density part of the EOS. A comprehensive study of nuclear energy density optimization based on Skyrme Hartree-Fock-Bogoliubov theory is done in Ref. [61].

Parameters used to generate Skyrme models are given in Table 2.1 and model selection is made following the same procedure as Ref. [32]. A random model is chosen from this set for each iteration. In terms of the randomness of selecting these models, the value of a selected parameter (primarily arbitrary) from the parameter set $\{p\}$ is multiplied with a large number, and the modulus of 1000 is taken.

$$\mathrm{row}_{\mathrm{Sk\_table}} = (10^9 p)\%1000 \tag{2.23}$$

Table 2.1: Skyrme functional parameters (x) and their mean values ($\hat{x}$) given with the standard deviation and 95% confidence interval.

x	$\hat{x}$	σ	$95\%CI$
ρ_c (fm^{-3})	0.15631	0.00112	[0.154, 0.158]
E/A (MeV)	-15.8		
K (MeV)	239.930	10.119	[223.196, 256.663]
a_{sym} (MeV)	29.131	0.321	[28.600, 29.662]
L (MeV)	40.0		
$1/M_s$	1.074	0.052	[0.988, 1.159]
$C_0^{\rho\Delta\rho}$ $(MeVfm^5)$	-46.831	2.689	[-51.277, -42.385]
$C_1^{\rho\Delta\rho}$ $(MeVfm^5)$	-113.164	24.322	[-153.383, -72.944]
V_0^n $(MeVfm^3)$	-208.889	8.353	[-222.701, -195.077]
V_0^p $(MeVfm^3)$	-230.330	6.792	[-241.561, -219.099]
$C_0^{\rho\nabla\rho}$ $(MeVfm^5)$	-64.309	5.841	[-73.968, -54.649]
$C_1^{\rho\nabla\rho}$ $(MeVfm^5)$	-38.650	15.479	[-64.246, -13.054]
C_0^{JJ} $(MeVfm^5)$	-54.433	16.481	[-81.687, -27.180]
C_1^{JJ} $(MeVfm^5)$	-65.903	17.798	[-95.334, -36.472]

The coupling constants uniquely determine original parameters in the Skyrme model in Table 2.1. The mean potentials t_0, t_1, t_2, and t_3 as well as the exchange parameters x_0, x_1, x_2, and x_3 at neutron matter saturation density can be calculated using the methods described in Ref. [115, 60]. A combination of the Skyrme model and results from QMC provides the necessary low-density EOS.

$$E(n_{\mathrm{B}}, x) = E_{\mathrm{Sk}}\left(n_{\mathrm{B}}, x = \frac{1}{2}\right) + \left[(1-2x)^2 E_{\mathrm{PNM}}(n_{\mathrm{B}}) - E_{\mathrm{Sk}}\left(n_B, x = \frac{1}{2}\right)\right] \tag{2.24}$$

For densities above $2n_0$, extrapolation methods were used to estimate the equation of state. One of the EOS prior in this project uses a three piecewise polytropes (3P). The generic form of the polytropic EOS is,

$$P = K\epsilon^{\Gamma} \tag{2.25}$$

The adiabatic index, $\Gamma = 1+1/n$, depends on the number of polytropes. A simple continuity condition is employed to fix the value of polytropic constant K and this K makes sure that the EOS remains continuous in between the transition densities at $2n_0$, n_{T1} and n_{T2}. There is also possibility of a strong phase transition in the high-density matter and only extreme values of Γ and K in polytropes will produce a flat EOS prior. A different EOS prior with discretized line segments (4L) connecting the points in the P-ϵ grid was utilized to allow some phase transitions within the EOS. Another important quantity that can be used to bound the divergence of the EOS is the speed of sound in matter $c_{\mathrm{s}}^2 = dP/d\epsilon$.

$$0 < c_{\mathrm{s}}^2/c^2 \leq 1 \tag{2.26}$$

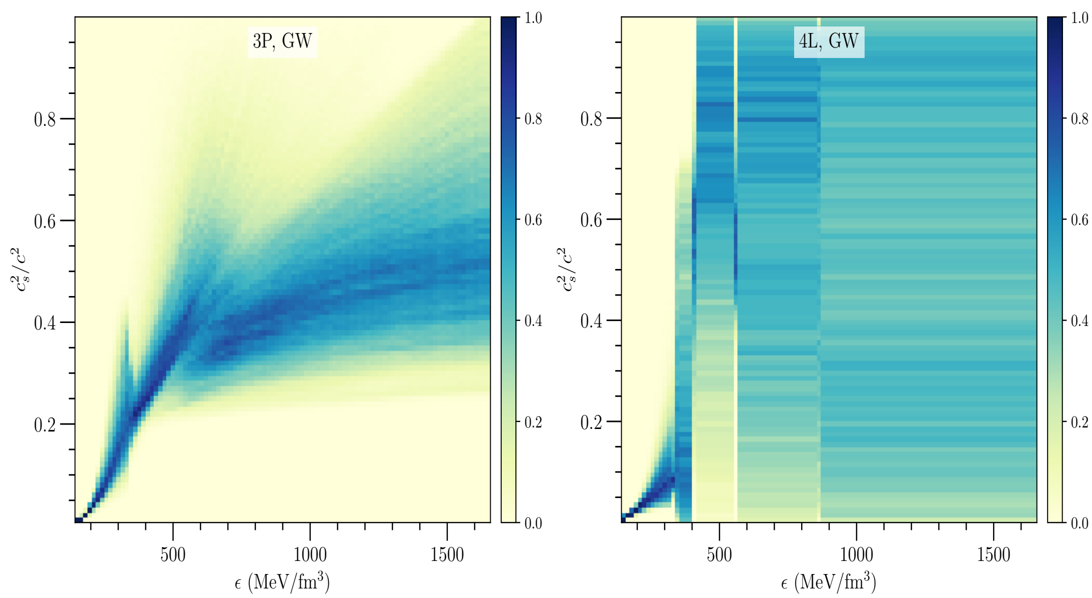

Figure 2.4: Speed of sound for both EOS priors as a function of energy densities.

Equation 2.26 gives us the measure of causality for EOSs, which implies that the speed of sound in matter should not exceed the speed of light c. Figure 2.4 demonstrates the c_s^2 distribution for different ϵ with both the 3P EOS (left panel) and the 4L EOS (right panel) prior.

2.6 NS Structure Calculation

Neutron star structure and evolution are calculated from the general relativistic corrections to the Newtonian formulation. The Tolman-Oppenheimer-Volkoff (TOV) equations are a set of coupled ODE that constrain a spherically symmetric body structure in equilibrium. The TOV equations can be solved with the assumption of NSs as spherically symmetric objects, and the intended M-R curves can be retrieved. These equations are built from selecting a stationary spherically symmetric metric, namely Schwarzschild metric, given as

$$ds^2 = -e^{2\Phi(r)}dt^2 + e^{2\Lambda(r)}dr^2 + r^2 d\theta^2 + r^2 sin^2\theta d\phi^2 \tag{2.27}$$

where, t is the time coordinate, r is a radial coordinate, θ and ϕ are the polar and azimuthal ones respectively. Also, $g_{\mu\mu}$ from Eq. 2.27 is $(-e^{2\Phi r},\ e^{2\Lambda(r)},\ r^2,\ r^2 sin^2\theta)$. All accreting neutron star rotate along its axis. Schwarzschild metric is applicable to slowly rotating neutron stars. The assumption here is that the NS considered for this project has period around seconds.

The proper length element $dl = e^{\Lambda(r)}dr$ from this metric shows $\Lambda(r)$ to be the correction to the proper radial length. $\Lambda(r)$ determines the space-time curvature in radial direction and generally defined in natural units ($G = c = 1$) as,

$$e^{\Lambda(r)} = \left(1 - \frac{2m}{r}\right)^{-1}. \tag{2.28}$$

Here, m is the gravitational mass that is smaller than the baryon mass or the rest mass. Similarly, the proper time interval $d\tau = e^{\phi(r)}dt$ requires $\phi(r)$ to provide corrections to the time coordinate. In GR, this correction is determined from the gravitational redshift as such

$$z(r) = e^{\phi(r)} - 1 \tag{2.29}$$

Einstein's field equation provides the relationship between the properties of massive objects to the geometry in GR. This equation relates the Ricci curvature tensor $\mathcal{R}_{\mu\nu}$ and the scalar curvature $\mathcal{R} = \mathcal{R}^{\mu}_{\mu}$ with the stress-energy tensor $T_{\mu\nu}$.

$$8\pi T_{\mu\nu} = \mathcal{R}_{\mu\nu} - \frac{1}{2}g_{\mu\nu}\mathcal{R} \tag{2.30}$$

$$T_{\mu\nu} = (P + \epsilon)u_{\mu}u_{\nu} - Pg_{\mu\nu} \tag{2.31}$$

$T_{\mu\nu}$ expression is for a perfect fluid assumption, and u is the four-velocity of matter. The energy density and pressure can be represented by the eigenvalues of $T_{\mu\nu}$.

$$T^0_0 = \epsilon \tag{2.32}$$

$$T^j_i = -P\delta^j_i \tag{2.33}$$

Calculating $T_{\mu\nu}$ and evaluating Einstein's field equations by component, the expression for pressure gradient can be derived.

$$\frac{dP}{dr} = -\frac{\epsilon m}{r^2}\left(1 + \frac{P}{\epsilon}\right)\left(1 + \frac{4\pi P r^3}{m}\right) \times \left(1 - \frac{2m}{r}\right)^{-1} \tag{2.34}$$

Also, the gravitational mass is defined as,

$$\frac{dm}{dr} = 4\pi r^2 \epsilon. \tag{2.35}$$

Equations 2.34 and 2.35 are the coupled TOV equations and can be solved simultaneously to get the M-R curves from a given EOS.

The M-R distribution and EOS have one-to-one correspondence and can be used to infer one quantity from the other. The implication of this specific feature is vast. Provided that there are reasonable M-R constraints from observations, one can infer the internal composition of neutron stars.

2.7 Moment of Inertia

The moment of inertia of a rotating object in a binary system can be used to infer individual tidal deformabilities. A couple of additional ODEs must be solved alongside the TOV equations to calculate the moment of inertia of neutron stars. For a slowly rotating relativistic star, Hartle [48] proposed a homogeneous second-order differential equation to calculate the dragging of local inertial frames, $\omega(r)$. From this specific work, the angular part of the spherically symmetric metric is defined as,

$$j = \left(1 - \frac{2Gm}{r}\right)^{1/2} e^{-\Phi} \tag{2.36}$$

This Φ value comes from the solution of Eq. 2.37

$$\frac{d\Phi}{dr} = -\frac{1}{\epsilon}\left(1 + \frac{P}{\epsilon}\right)^{-1} \frac{dP}{dr} \tag{2.37}$$

Scaling the rotation rate ω in the inertial frame with the angular velocity Ω in the fluid frame as $f = (\omega - \Omega)/\Omega$, the ODEs formulating the dragging is given as

$$\frac{dg}{dr} = -4r^3 \frac{dj}{dr} f \tag{2.38}$$

$$\frac{df}{dr} = \frac{g}{r^4 j} \tag{2.39}$$

A solution from the above equation provides the necessary information on the moment of inertia in terms of the scaled angular velocity.

$$I = \frac{R^4}{6G} \frac{df}{dr}\Big|_{\mathrm{r=R}} \tag{2.40}$$

2.8 Tidal Deformability

Two near orbiting objects will always respond to the gravitational field from each other. Depending on their respective sizes, the gravitational pull might change the outer structure in one or both of these objects. This response to the differential gravitational field is defined as the tidal force. This force determines the amount of stretching towards the center of the mass frame of these objects. Augustus Edward Hough Love made the first mathematical introduction on Earth's tidal response in 1909 [79]. There are three dimensionless parameters (Love numbers) $h, k,$ and l which formulate the rigidity and susceptibility of the object's shape due to tidal response. Love number h determines the ratio of the body tide to the equilibrium, k determines the self-reactive potential of that object due to the external potential, and l represents the transverse displacement.

In a binary neutron star, this tidal response produces deformations that can be directly measured. The tidal deformability Λ is defined as the linear response to the ratio of the induced mass quadrupole moment Q_{ij} to the tidal field ε_{ij}.

$$\Lambda = -\frac{Q_{ij}}{\varepsilon_{ij}} \tag{2.41}$$

This quantity can be parameterized with $l = 2$ Love number (general notation k_2) and the star's radius.

$$\Lambda = \frac{2}{3} k_2 r^5 \tag{2.42}$$

In a recent publication, authors in Ref. [129] showed the existence of a strong correlation between the moment of inertia $\bar{I}_{\mathrm{i}} = I_{\mathrm{i}}/m_{\mathrm{i}}^3$ and the tidal deformabilities $\bar{\Lambda}_{\mathrm{i}} = \Lambda_{\mathrm{i}}/m_{\mathrm{i}}^5$. These relationship from Ref. [129] was used to calculate the dimensionless tidal deformabilities of the NSs.

$$\begin{aligned} \ln\bar{\Lambda}_{\mathrm{i}} \simeq -30.5395 &+ 38.3931(\ln\bar{I}_{\mathrm{i}}) - 16.307(\ln\bar{I}_{\mathrm{i}})^2 \\ &+ 3.36972(\ln\bar{I}_{\mathrm{i}})^3 - 0.26105(\ln\bar{I}_{\mathrm{i}})^4 \end{aligned} \tag{2.43}$$

Here, $\mathrm{i} = \{1, 2\}$ is the index representing the members of the binary.

2.9 Model Descriptions

In section 2.5, the details are given on the procedure to select an EOS prior, either 3P or 4L. In addition to that, there are four different sources (QLMXB, PRE, GW, and NICER) of NSs to use in these analyses. A total of eight different models were selected from two EOS priors with combinations of different observations. The label for each model is in Table 2.2, and this convention is followed throughout this work.

Table 2.2: Legend explaining EOS parameterizations and data sets used in the figures. The three-polytrope model is labeled "3P", and the four line-segment model is labeled "4L".

Label	EOS parameterizations and data selection
(a)	3P with GW only
(b)	4L with GW only
(c)	3P with {GW, QLMXB, PRE}
(d)	4L with {GW, QLMXB, PRE}
(e)	3P with {GW, QLMXB, PRE, NICER}
(f)	4L with {GW, QLMXB, PRE, NICER}
(g)	3P with {GW, QLMXB, PRE, NICER} w/int. scat.
(h)	4L with {GW, QLMXB, PRE, NICER} w/int. scat.

The first two models (a and b) only take constraints from the gravitational wave observation GW170817 for the analysis. They can be used as baseline models to test and verify the posteriors from the LIGO-VIRGO inferences. Models c and d have additional X-ray observations from QLMXBS and PREs. In models e and f, the mass-radius constraints from PSR J0030+0451 are added to the previous X-ray data. These two models can be used to test the improvements, if any, on mass-radius relation with the published NICER observation.

The final two models include the intrinsic scattering operation on the X-ray data, and the outcome from these models should reveal any hidden systematics. These models are used to generate sample points from Markov Chain Monte Carlo simulations, and the details on the sampling process are given in the next chapter.

2.10 Sampling Method

Constraints from the observed binaries (except LIGO) are set as free parameters in the simulations. In total, our 3P models have twenty-two free parameters (twenty four with PSR J0030+0451); ten binaries (additional pulsar from NICER), eight EOS parameters (a, α, S, L, Γ_1, t_1, Γ_2, t_2, and Γ_3) and three more to parameterize LIGO observation ($\mathcal{M}_{\rm det}$, η, and z). The first four EOS parameters are used to calculate the QMC part while Γ and t represent the polytropic indices and transition points, respectively. In 4L models, a different set of EOS parameters (a, α, S, L, P_1, P_2, P_3, and P_4) was used but the other parameters for observed binaries, pulsars and GW constraints were kept same as before. Here, P's are four pressure line segments (4L) calculated in the high-density region. Models a and b have fewer parameters as all the X-ray data were excluded in them. The intrinsic scattering models, g and h, have eleven more additional parameters, one for each QLMXBs, PREs, and J0030. A combination of MPI and OpenMP implementations was used to parallelize the MCMC runs (four MPI rank and twelve OpenMP thread per MPI rank). Each of these process simulate individual Monte Carlo chain with coupled walkers within them. Nonetheless, these chains take a significant amount of time to equilibrate. Thus a generic Metropolis-Hastings algorithm with a single walker was not efficient enough for simulating eight different models. A system of multiple walkers was incorporated, $X = \{x_1, x_2, .., x_N\}$, referred to as ensemble of walkers, and an affine-invariant sampling method was used to expedite the sampling process. In this sampling method, the probability of individual walkers is independent, and the total probability for the ensemble can be obtained as $\pi = \pi(x_1)\pi(x_2)..\pi(x_N)$. In these simulations, a 30 walker ensemble was used for each OpenMP thread.

The affine-invariant sampling method was first proposed by Goodman and Weare [43]. This MCMC sampling algorithm uses an ensemble of walkers and has the property of affine-invariance, which means the performance is invariant under linear transformations in parameter space. The basic principle of this method is to allow each walker to undergo a trial move in each iteration and check the acceptance based on some probability in the parameter space. There are a couple of steps to follow during simulations:

1. Set the number of walkers X and initialize them (for the first iteration). One caveat of affine sampling is the need to use at least 2N walkers for N parameters. Each walker is initialized with N parameter values, and the walkers should get different initialization from one another.

2. Propose a trial move for k-th walker as

$$x_{\mathrm{trial}} = x_{\mathrm{k}} + z(x_{\mathrm{j,j\neq k}} - x_{\mathrm{k}}) \tag{2.44}$$

This equation updates the relative position of x_{k} based on other walkers in the ensemble. The maximum and minimum distances between the walkers are set by a step value a,

$$g(z) \propto \frac{1}{\sqrt{z}}, \; z \in [\frac{1}{a}, a] \tag{2.45}$$

$g(z)$ is the metric to measure the relative distance z for walkers in Eq. 2.44.

3. Set a Metropolis acceptance probability $\pi = min\,\{1, \mathcal{P}\;(x_{\mathrm{trial}})/\mathcal{P}\;(x_{\mathrm{k}})\}$ and update the walker.

$$x_{\mathrm{k}}(t+1) = \begin{Bmatrix} x_{\mathrm{trial}}, & \pi \\ x_{\mathrm{k}}, & 1-\pi \end{Bmatrix} \tag{2.46}$$

4. Repeat iterating over t from step 2.

The end criterion for this sampling method is defined by the autocorrelation length, which is the longest wavelength of oscillations in these distributions and corresponds to the number of steps between the uncorrelated samples in the posteriors. This length is highly dependent on how the burn-ins were chosen. Table 2.3 lists the auto-correlation lengths for a selection of parameters from the posteriors. For the burn-ins, the idea was to discard enough initial samples so that at least one band is removed from all models. With the maximum auto-correlation length from Table 2.3, 40000 initial samples were discarded from each model to ensure that the Markov chains are well equilibrated.

Table 2.3: Auto-correlation lengths for different models in thousand.

Model	S	L	$R_{1.4M_\odot}$	$M_{\max}$	q	Λ_1
(a)	3.30	4.01	8.17	2.25	5.61	7.63
(b)	2.94	2.89	3.22	3.30	3.85	3.58
(c)	18.97	19.57	23.81	16.02	22.92	22.75
(d)	14.03	14.33	21.21	22.41	18.56	19.94
(e)	25.79	19.45	12.31	13.44	23.99	17.82
(f)	19.41	24.48	15.07	22.73	19.86	20.58
(g)	14.47	14.47	9.57	9.95	10.53	10.21
(h)	14.37	14.38	10.66	11.79	11.43	10.38

The initial tests on these models were done on two in-house workstations, but the model simulations were performed with 200,000 core hour allocations in Bridges cluster from Pittsburgh Supercomputing Center (PSC). This project were also allocated 300,000 core hour in Comet cluster by the Extreme Science and Engineering Discovery Environment (XSEDE) which is supported by the National Science Foundation.

Chapter 3

Model Inferences

Inferential statistics is the core part of data-driven modeling. While there are several general approaches to inferential statistics, Bayesian inference is the widely accepted tool in physics.

3.1 Bayesian Inference

Bayesian is a method of statistical inference that allows researchers to combine prior information of a parameter set with the evidence gained in the inference process. This method is much more suitable than the frequentist method due to the underlying assingment of probabilities to the parameter space. One starts by defining a model M with an associated probability $\mathcal{P}(M)$, this is the prior without any information of data, and compute the likelihood function $\mathcal{P}(D|M)$ from given the data D. Using Bayes' formula, one can compute the posterior distribution $\mathcal{P}(M|D)$,

$$\mathcal{P}(M|D) \propto \mathcal{P}(D|M)\mathcal{P}(M) \tag{3.1}$$

An essential aspect of this method is that the priors should not be changed at any given moment after the likelihood or evidence is computed.

3.2 Intrinsic Scattering Parameter Posteriors

Figure 3.1 presents the posterior distributions for the intrinsic parameters (σs) from neutron star sources with spectral observations. The subplots are made from the respective EOS priors, 3P on the left and 4L on the right. These distributions provide insight into probable sources which might contain additional systematic uncertainties.

The peak near the lower values of the intrinsic parameter means that the spectral data are primarily noise-free. In Fig. 3.1, most sources have high probabilities for $\sigma < 0.1$ and, the distribution gradually goes to zero with an increasing value of σ. The QLMXB and NICER objects have slightly larger intrinsic scattering parameters than the PRE objects. Here, the neutron star in NGC 6397 is an exception. The posteriors from this source showed the tendency to peak around $\sigma \sim 1$. Authors in Ref. [112] found that the atmospheric prior, H or He, for NGC 6397 has a significant impact in its radii measurements. For an H atmospheric fit, NGC 6397 associated a small radius neutron star which might cause this significant peak at larger a value of σ.

Neutron star mass posteriors from the intrinsic scattering models are given in Fig. 3.2. In the top two panels, The normalized mass posteriors from each neutron star are shown. The LIGO-VIRGO observation GW170817 made more accurate mass measurements for the associated neutron stars than the X-ray sources. The strongly-peaked LIGO posteriors, referred to as M_1 and M_2, due to these accurate mass measurements from GW sources.

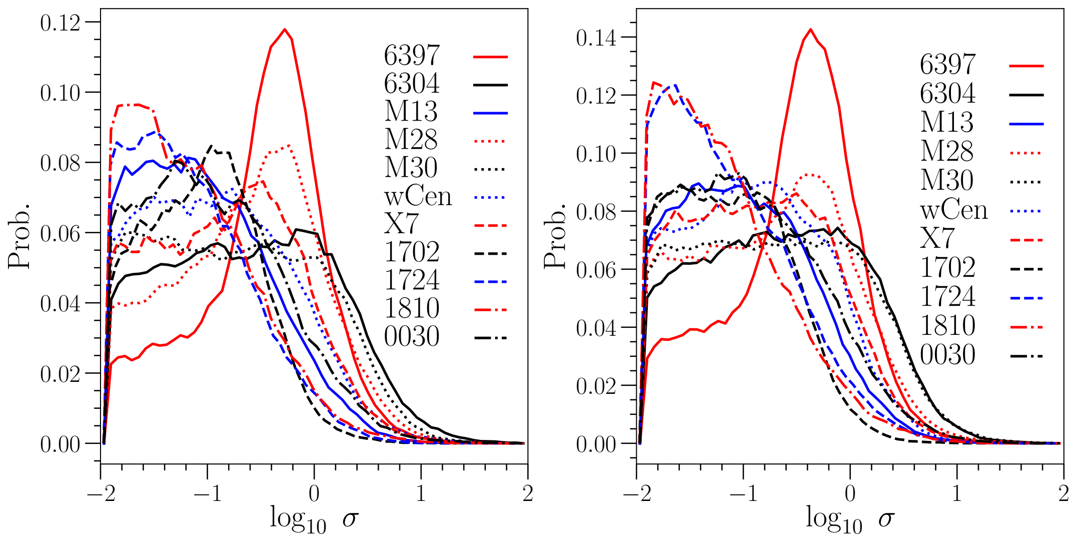

Figure 3.1: The posterior distributions for the intrinsic scattering parameters. The distributions are normalized with total Prob.= 1. The panels are grouped based on the EOS priors. The left panel is from model "3P, all+IS" and, the right one is based on model "4L, all+IS".

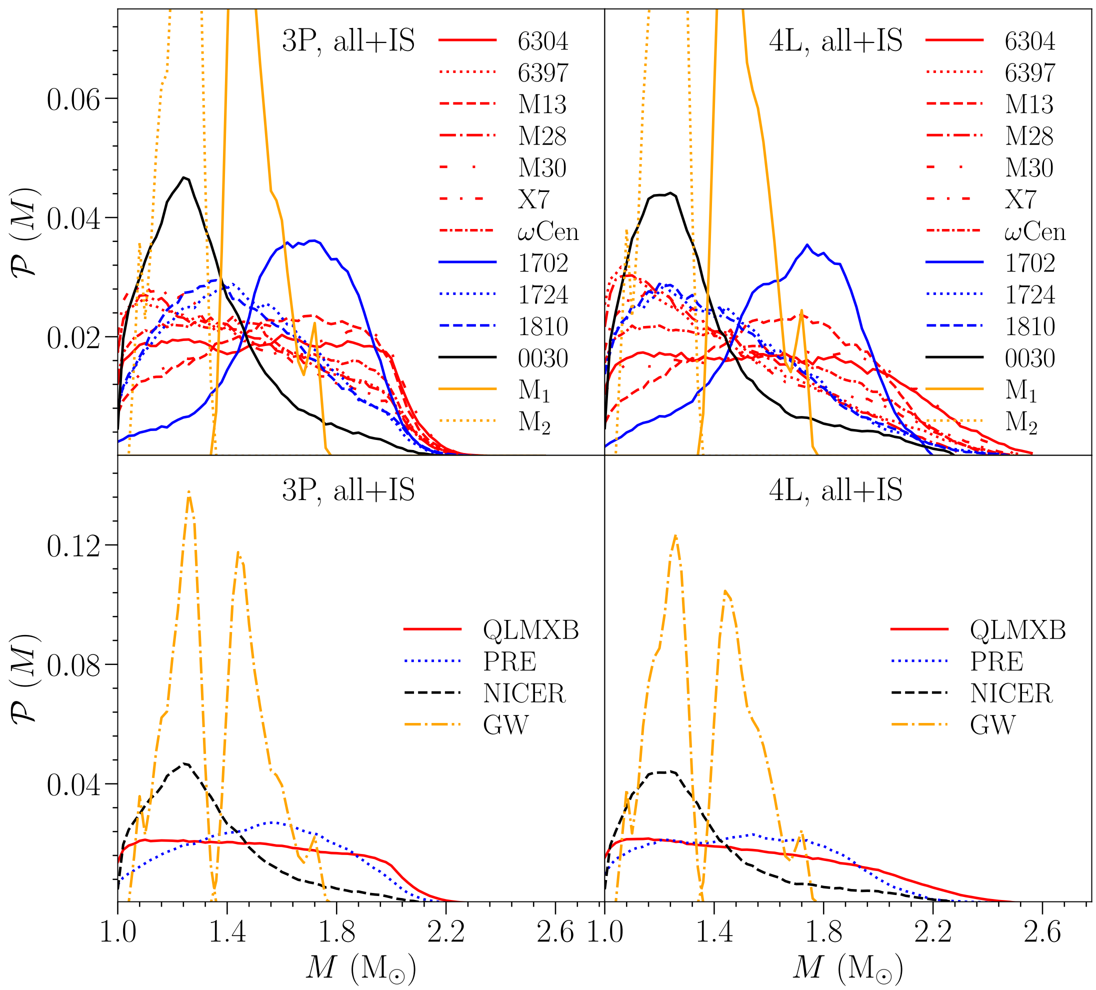

Figure 3.2: The normalized posterior distributions of NS masses from intrinsic scattering models, 3P in the left column and 4L in the right. The top two panels show posteriors for individual NSs while the bottom two panels provide posteriors for different groups of NSs.

In the bottom two panels, the mass posteriors are grouped by the kind of observation: neutron stars from QLMXBs, NSs that have photospheric X-ray bursts, the neutron star observed by NICER, and the LIGO NSs. In these grouped distributions, the posterior from NICER tend to have a slightly smaller mass than the other groups, and the X-ray burst sources prefer a larger mass. The posteriors distributions in the bottom two panels extend well above 2 $M_{\odot}$. The extended mass range indicates that the accurate maximum mass of a neutron star $M_{\rm max}$ can be this large. Tables with the 1σ and 2σ pressure range for all energy densities in models "3P, all+IS" and "4L, all+IS" are given in Appendix B. The radial range for all possible neutron star masses intrinsic scattering models are also tabulated in appendix B.

3.3 Neutron Star Posteriors

The posterior distributions of neutron star structure are acquired by using the methods described in chapter 2 and the assembled results in this section are published in Ref. [2]. The main objective of this project was to include the mass-radius constraints from GW170817 with the constraints from spectral observations of other sources. Observatories, whether it is earth-based or in space, detect a vast amount of radio signals all the time. Coupled with all other radiations, most of these detected signals are not good candidates to constrain NS radii. Providentially, the gravitational wave detection is not riddled with such background noises, and GW170817 provided excellent constraints on the NS masses. The hypothesis was that including the GW data in a joint analysis would provide new and better constraints on all other informative parameters.

Tidal deformabilities of NS binaries are strongly coupled with the compactness $C = M/R$ and the radius of NS. Detection of surface deformations in inspirals, due to tidal fields, provide a different take on radii measurements. Λ can be used to constrain R if the masses are known within an acceptable uncertainty. Figure 3.3 shows the posterior distributions for individual tidal deformabilities in NS binaries. In Fig. 10 of Ref. [74], the authors presented their results on the tidal deformations of GW170817 inspiral.

A combined analysis of GW and EM data can put resonable constraints on tidal deformations. Authors in Ref. [95] made a combined analysis with the GW data and the spectral information from the merger remnant and found the lower limit of $\tilde{\Lambda}$ supports equal or greater values than 300. Several recent publications demonstrated some variations on this lower limit.

Reference [27] used a set of different mass priors alongside EM data from the GW170817 merger to deduce the bounds of $\tilde{\Lambda}$. Their result for uniform component mass prior provides a range of $85 \leq \tilde{\Lambda}_{1.4} \leq 640$ with a 90% confidence limit. Expanding these results with a unitary gas conjecture, Ref. [68] found $240 \leq \tilde{\Lambda}_{1.4} \leq 720$ to be more stringent. The inclusion of radio signals from other binaries in this work made more profound predictions on $\tilde{\Lambda}_{1.4}$. Table 3.1 lists the bounds generated from each model.

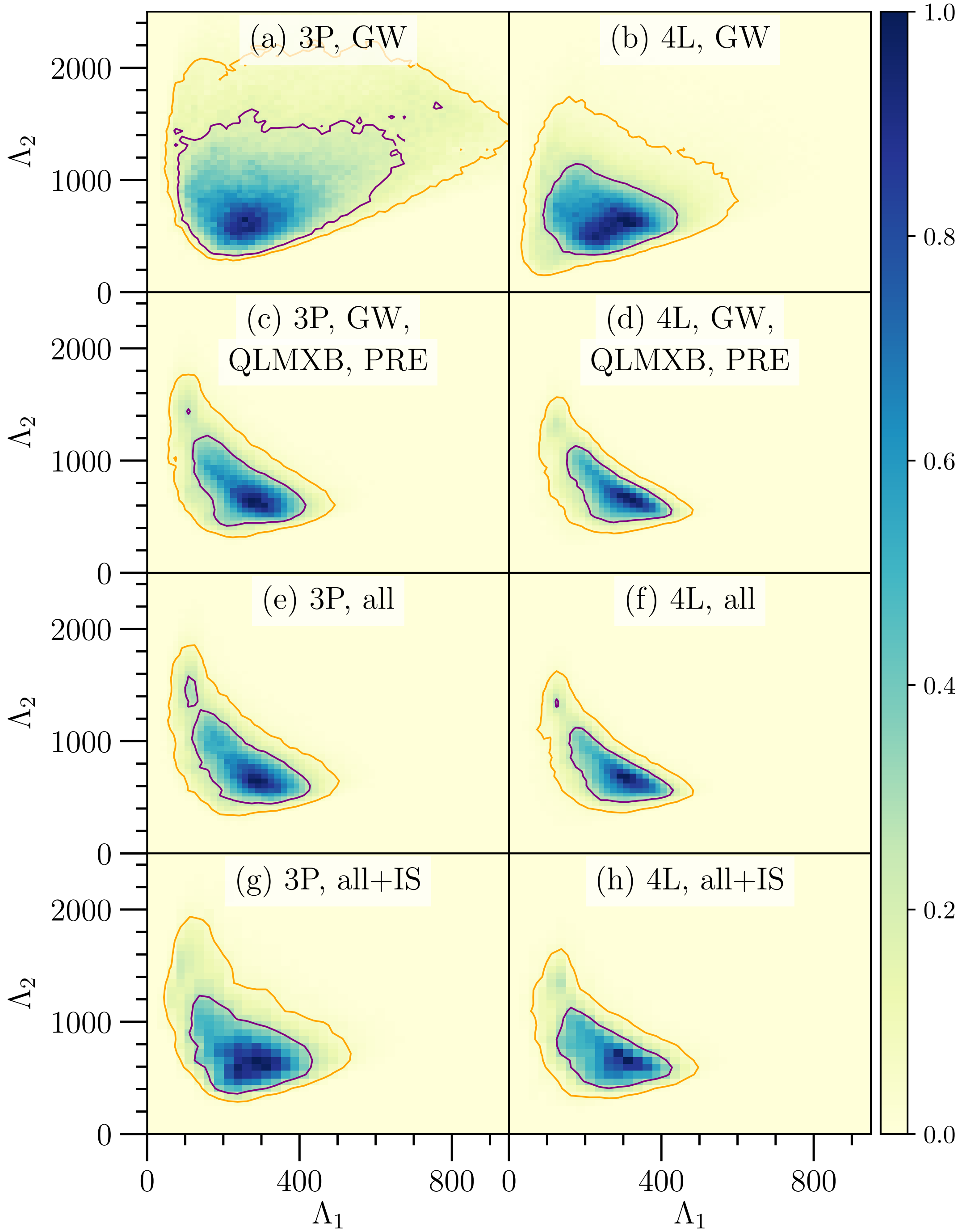

Figure 3.3: Posterior distributions for Λ_2 and Λ_1 with renormalized density plots. The renormalization process scales from 0 to 1. The purple and orange contours bound the 68% and 95% confidence intervals of these distributions. Left panels are generated with 3P EOS prior while the panels on the right column are from 4L EOS.

Table 3.1: Tidal deformability ($\tilde{\Lambda}$) for a 1.4 $M_\odot$ neutron star with 1σ (68%) and 2σ (95%) confidence limits.

Model	-2σ	-1σ	$+1\sigma$	$+2\sigma$
(a) 3P, GW	209	236	603	913
(b) 4L, GW	128	239	435	584
(c) 3P, GW, QLMXB, PRE	227	303	421	484
(d) 4L, GW, QLMXB, PRE	237	297	397	436
(e) 3P, all	220	303	432	537
(f) 4L, all	252	307	403	444
(g) 3P, all+IS	300	365	649	825
(h) 3P, all+IS	203	263	420	648

Figure 3.4 shows the EOS posteriors for all eight models. Spectral data can dominate gravitational ones, which can be seen in these posteriors, and this effect can be seen for energy densities up to 700 MeVfm^3. For the EOSs corresponding to 3P models, pressure P increases monotonically with energy densities, but this is not the case for the 4L ones. As it was mentioned earlier, the 4L prior was set to allow phase transition for large densities. Although an explicit phase transition of nuclear matter to quark matter was not implemented in this EOS prior, the kinks exhibited by the panels on the right side provide evidence towards the possible existence of this effect.

Apart from the kinks between 3P and 4L models, these EOSs in Fig. 3.4 do not present any different aspects within the subgroups. For this reason, all these EOS posteriors are rescaled in terms of model a and, their comparison plots are given in Fig. 3.5. The rescaled plots in Fig. 3.5 are constructed with the 2σ C.I. from "3P, GW" model, which is linearly transformed in-between 0 and 1, and the 1σ C.I. is normalized with the scale factor from 2σ transformation. The confidence limits from all other models are normalized with the same 2σ scaling factor. The 3P rescaled panels with the X-ray sources have slightly narrower 2σ range, except the "3P, all+IS" model, which has narrower 2σ range with the whole range shifted towards a larger pressure value. This shift was expected because the filter used in the intrinsic scattering method smooths out the internal boundaries and creates new centroid values in the dataset. The variations in pressure distribution are noticeable in the right-side panels. All 4L models have a larger spread in their EOS posteriors. Figure 3.5 also shows the normalized probability distribution of the maximum value of central energy density $\epsilon_{\max}$ for each model.

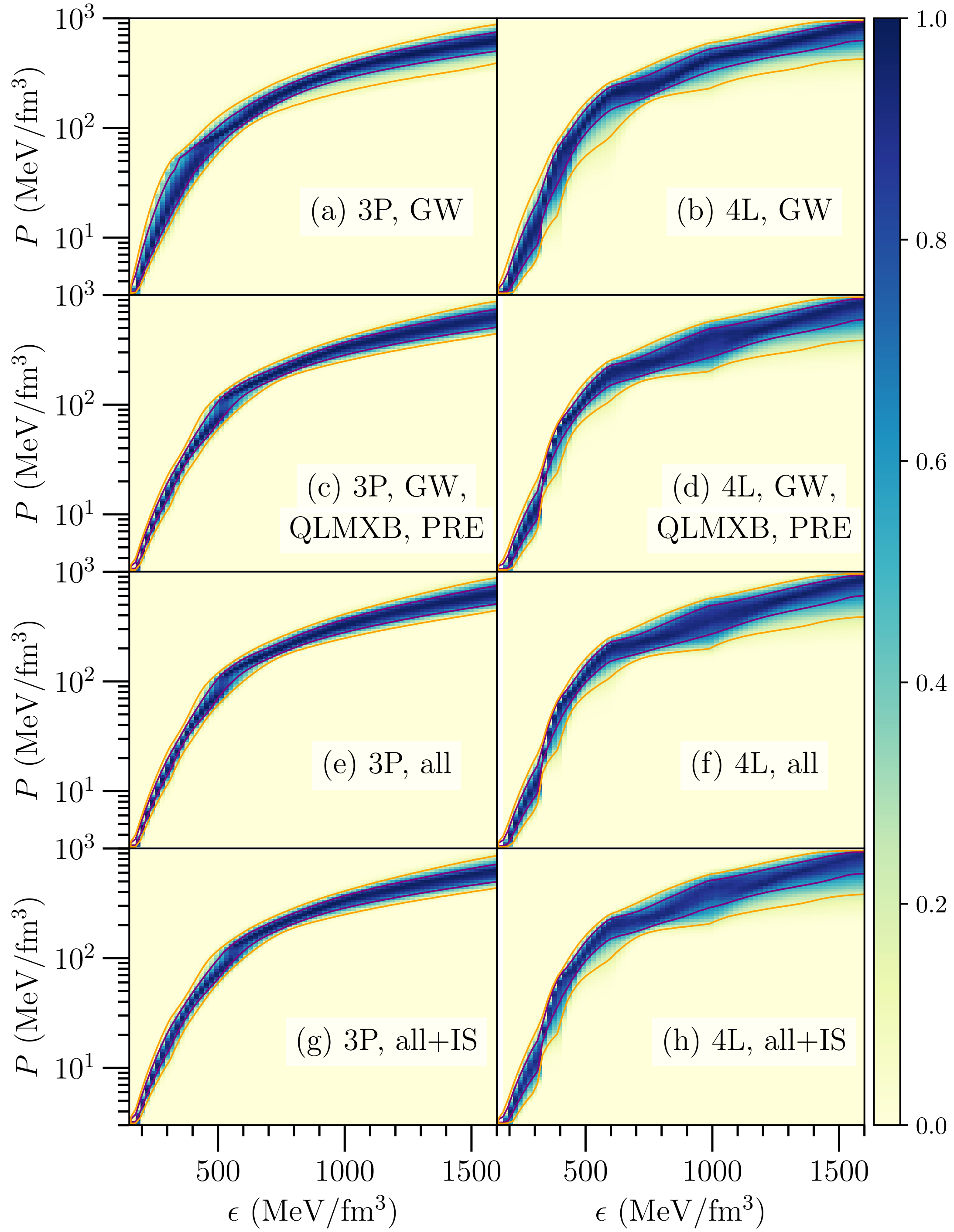

Figure 3.4: Posteriors for pressure as a function of energy desnsity. Left side panels are constructed with 3P EOS and the ones on right side corresponds to the 4L EOS. The purple and orange lines provide 1σ (68%) and 2σ (95%) confidence limits of these distributions.

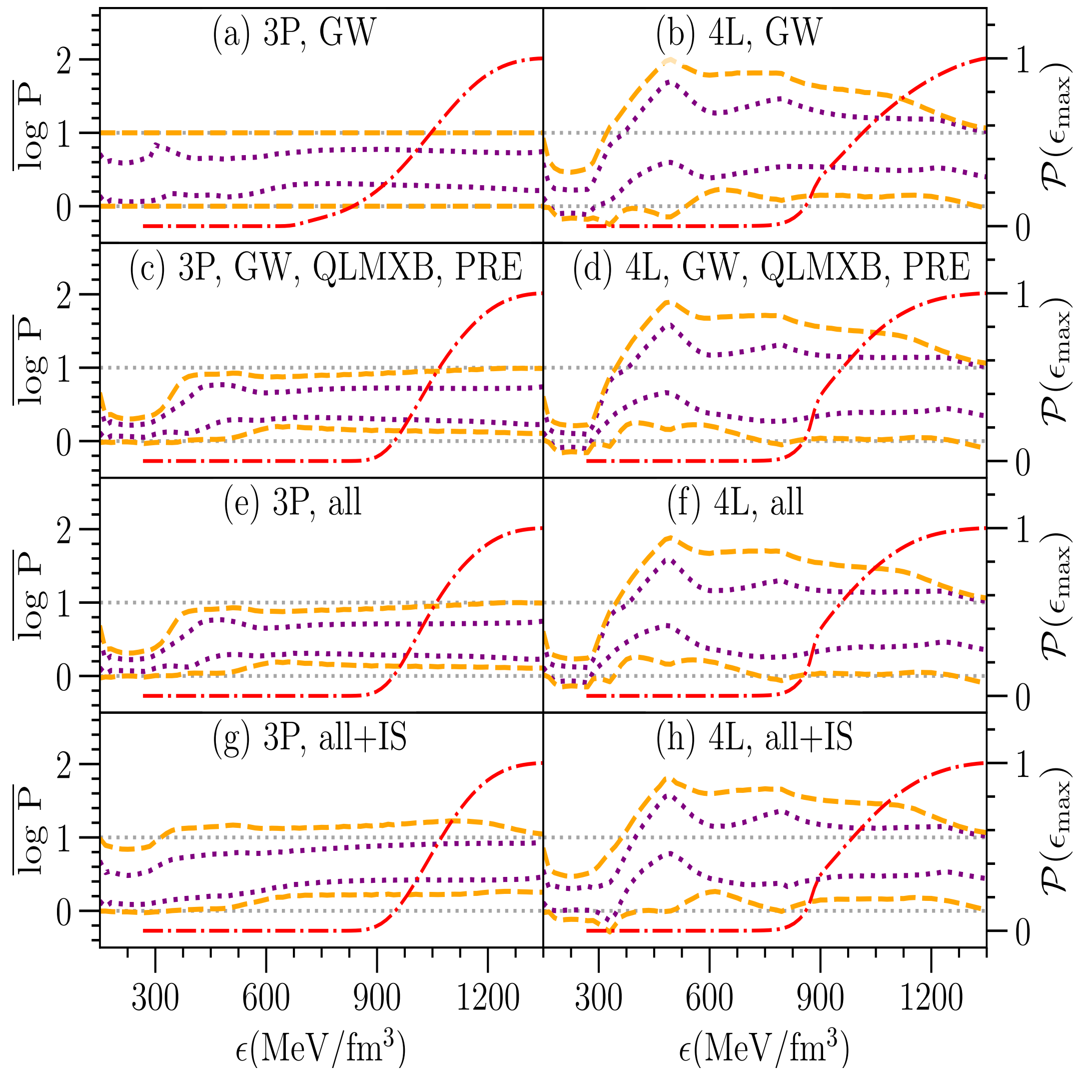

Figure 3.5: Rescaled pressure as a function of energy density given in 1σ (purple dotted line) and 2σ (orange dashed line) confidence limits. All limits are modified from the C.I. given in Fig. 3.4. The posterior probability of the central energy density $\epsilon_{\max}$ is given in the right-hand y axis. The normalized $\epsilon_{\max}$ is shown as a red dot-dashed line.

The $\epsilon_{\max}$ distributions mark the range of energy density, after which the density in the core starts to rise. For example, the central energy density in the "3P, GW" model begins to increase at $\epsilon \sim 700$ Mev/fm^3. In other 3P models, the change in probability for the central density begins near 900 MeV/fm^3. Also, the kinks in 4L models may indicate the possible phase transitions in the core.

The mass-radius distributions of neutron stars are given in Fig. 3.6. The effect on the neutron star radius with additional observations is apparent from these figures. The most significant spread on radial constraints is measured from the constructed models only with the GW data. Adding the QLMXBs and PREs significantly narrowed down the distributions. Models with NICER results from PSR J0030+451 do not provide better constraints than the models without it. NICER observation has predicted larger radii in comparison to the other X-ray sources. Also, M-R posterior distributions from the IS models predicted slightly larger 1σ and 2σ constraints than the models with the "all" dataset.

Figure 3.7 is made to compare the measured radii of 1.4 $M_\odot$ neutron star from all eight models. The 2σ C.I. from the models with GW data are $R_{1.4} \in [11.3, 13.9]$ km for 3P and $R_{1.4} \in [10.7, 13.1]$ km for 4L. Adding the EM data lowered the radius limit by 0.5 km.

The radius of a canonical mass neutron star is used to compare different models. Several different theoretical predictions were made on the radius limit of a 1.4 $M_\odot$ NS. Table 3.2 is compiled with a couple of model predictions from recent research done by different authors and made comparisons with the model inferences made in this project. In this Table 3.2, the predictions are grouped based on the type of observations used in the respective analysis.

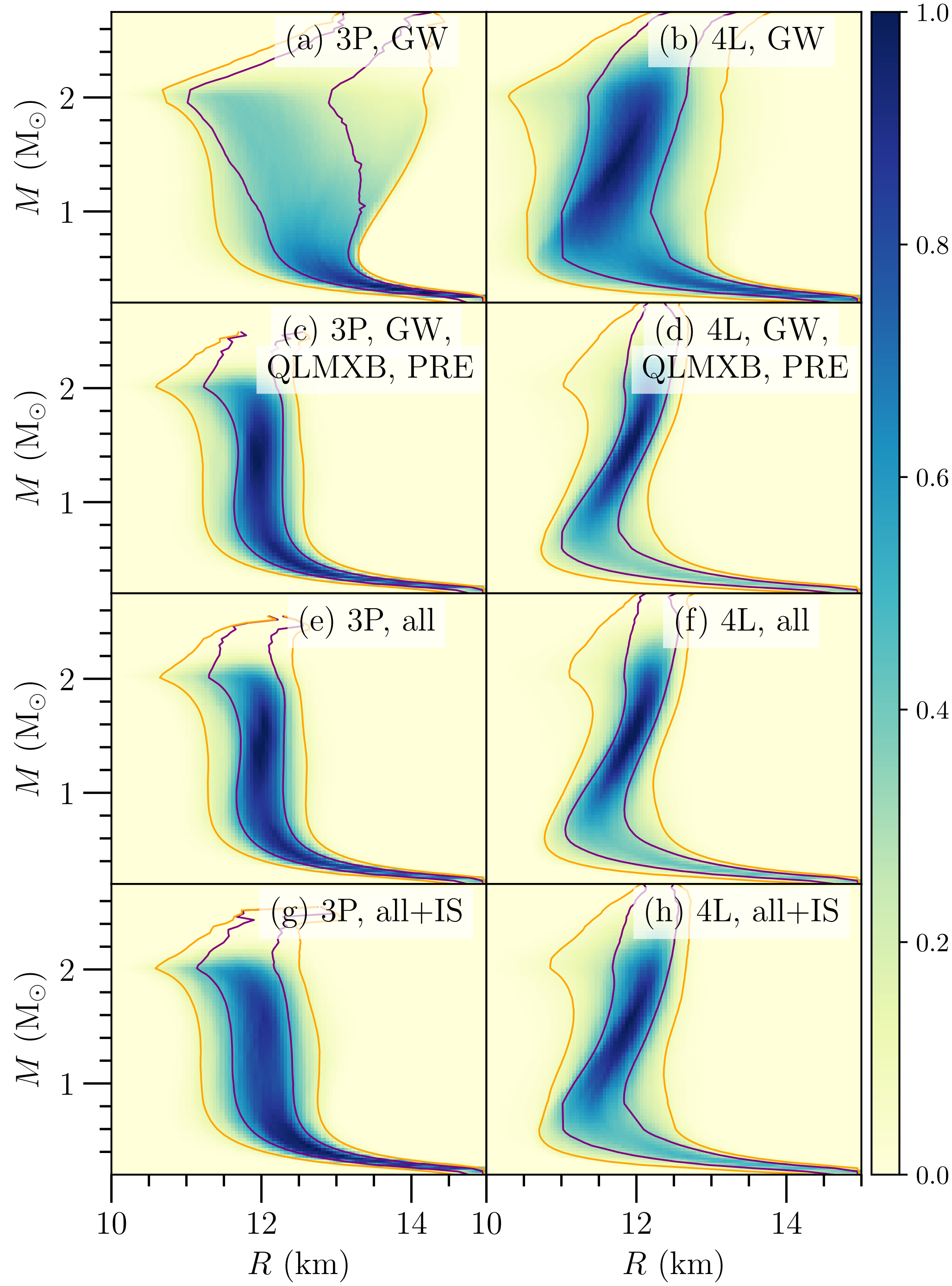

Figure 3.6: Posterior distributions for neutron star radius as a function of it's gravitational mass. Left side panels are constructed with 3P EOS and the ones on right side corresponds to the 4L EOS. The 1σ (68%) confidence limit is shown by the purple lines and 2σ (95%) C.I. are given with the orange ones.

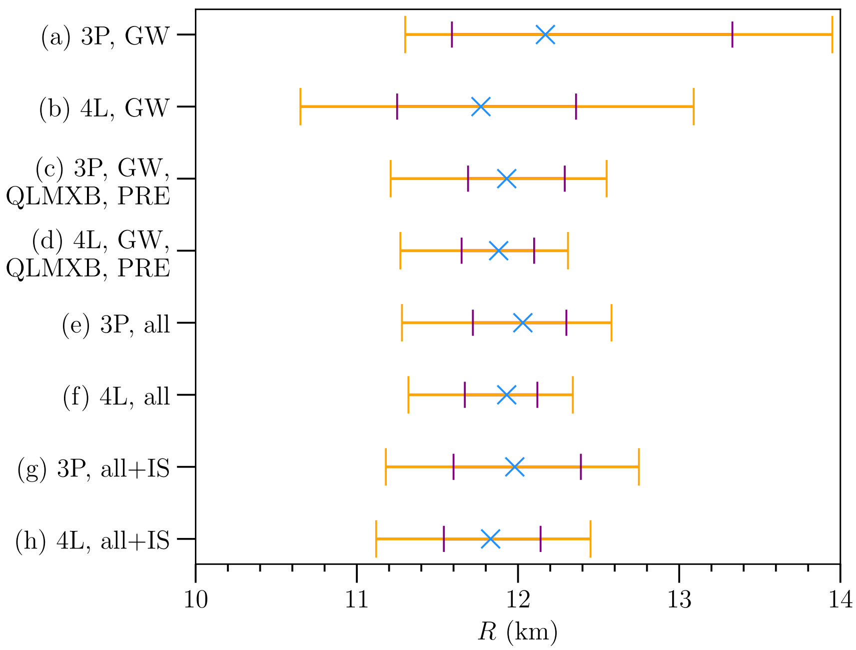

Figure 3.7: Radii measurements for a 1.4 $M_\odot$ neutron star from different models. The blue crosses represent the maximum a *posteriori* estimates. The purple and orange bars corresponds the 1σ and 2σ credible limits.

Table 3.2: Radial constraints for 1.4 $M_\odot$ neutron star from different models and compared with the constraints found in literature. "GWs" represents the dataset from GW170817 and GW190425. The "merger remnant" indicates the outcome from NS binary merger GW170817.

Reference	$R_{1.4}$	C.I.	Source
[74]	[10.5, 13.3]	90%	GW
[3]	[9.9, 13.6]	90%	GW
[39]	< 13.6	90%	GW
[62]	[9.4, 12.8]	90%	GW
[96]	[9.8, 13.2][1]	90%	GW
[38]	[10.36, 12.78]	90%	GW
Model "a"	[11.30, 13.95]	95%	GW
Model "b"	[10.65, 13.09]	95%	GW
[27]	[8.9, 13.2]	90%	GW, merger remnant
[95]	[11.4, 13.2]	90%	GW, merger remnant
[22]	[10.4, 11.9]	90%	GW, merger remnant
[29]	[11.98, 12.76]	90%	GW, QLMXB
[57]	[10.5, 11.8]	90%	GW, QLMXB
[31]	[10.94, 12.72]	90%	GWs, NICER
[65, 66]	[10.85, 13.41]	90%	GWs, NICER
[38]	[11.91, 13.25]	90%	GW, NICER
[58]	[11.3, 13.3]	90%	GW, NICER
[97]	[12, 13]	90%	GWs, NICER
[97]	[10.0, 11.5]	90%	GWs, QLMXB, PRE
Model "c"	[11.21, 12.55]	95%	GW, QLMXB, PRE
Model "e"	[11.28, 12.58]	95%	GW, QLMXB, PRE, NICER

3.4 Constraints on $M_{\max}$

The mass radius distributions in Seaction 3.3 are made with the EOS posterors that support $M_{\max} > 2\ \mathrm{M}_\odot$. No explicit upper bounds were applied to the calculations done the aforementioned section. Authors in Ref. [103] used a general relativistic magneto-hydrodynamics simulations to find a limit for the neutron star maximum mass. Their simulations predicted $M_{\max} \leq 2.17\ \mathrm{M}_\odot$ with 90% confidence limit. The M-R posteriors with $M_{\max} \leq 2.17\ \mathrm{M}_\odot$ is provided in Fig. 3.8. From this figure, it is evident that constraining $M_{\max} \in [2,\ 2.17]\ \mathrm{M}_\odot$ does modify the the whole distribution. Posteriors from all eight models have larger 1σ and 2σ C.I. than the unconstrained ones. The radial range for a $1.4\ \mathrm{M}_\odot$ NS with this maximum mass constraint is given in Table 3.3. As a matter of fact, the "4L, GW" model could not properly calculate the confidence intervals for $1.4\ \mathrm{M}_\odot$ NS.

A couple of recent observations made neutron star mass measurements significantly larger than $2.17\ \mathrm{M}_\odot$. LIGO-VIRGO collaboration also observed a compact object with $2.6\ \mathrm{M}_\odot$ [1]. There has been much discussion done about this object being a neutron star [37, 117]. Also, the intrinsic scattering analysis done in Section 3.2 predicted that the mass value for both QLMXB and PRE groups could extend far beyond $2.2\ \mathrm{M}_\odot$.

To test extreme mass limits of a neutron star, another maximum mass constraint $M_{\max} > 2.6\ \mathrm{M}_\odot$ has been applied to the posteriors. None of the 3P models could generate a model that supports this maximum mass limit, but the line-segment models can reach this $M_{\max}$. Although the polytropic models in this project currently did not predict any neutron star with $2.6\ \mathrm{M}_\odot$, it is not impossible to get to this mass value.

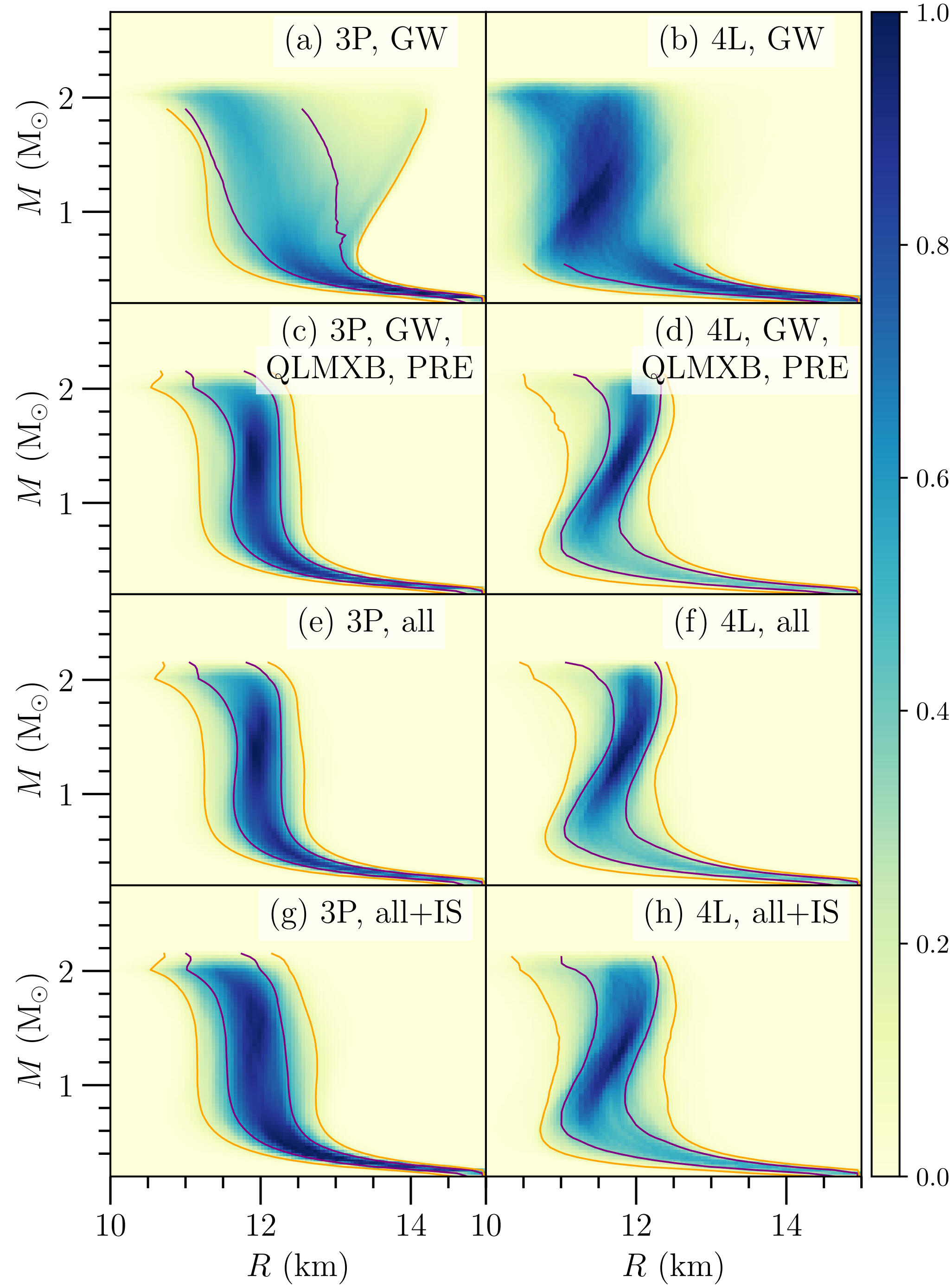

Figure 3.8: Posterior distributions for neutron star radius as a function of it's gravitational mass. Left side panels are constructed with 3P EOS and the ones on right side corresponds to the 4L EOS. The 1σ (68%) confidence limit is shown by the purple lines and 2σ (95%) C.I. are given with the orange ones.

Table 3.3: Radial constraints of a 1.4 $M_\odot$ neutron star with $M_{\max} < 2.17\ M_\odot$ limit. The units are in km.

Model & data	-2σ	-1σ	$+1\sigma$	$+2\sigma$
(a) 3P, GW	11.24	11.39	12.95	13.92
(b) 4L, GW	-	-	-	-
(c) 3P, GW, QLMXB, PRE	11.16	11.65	12.26	12.50
(d) 4L, GW, QLMXB, PRE	11.09	11.58	12.13	12.34
(e) 3P, all	11.23	11.69	12.27	12.55
(f) 4L, all	11.19	11.64	12.16	12.38
(g) 3P, all+IS	11.15	11.54	12.31	12.72
(h) 4L, all+IS	10.98	11.43	12.13	12.46

Table 3.4: Radial constraints of a 1.4 $M_\odot$ neutron star with $M_{\max} > 2.6\ M_\odot$ limit. The units are in km.

Model & data	-2σ	-1σ	$+1\sigma$	$+2\sigma$
(b) 4L, GW	11.56	11.79	12.79	13.45
(d) 4L, GW, QLMXB, PRE	11.59	11.74	12.08	12.30
(f) 4L, all	11.63	11.74	12.09	12.31
(h) 4L, all+IS	11.47	11.76	12.19	12.42

The radial ranges from the 4L models are given in Table 3.4. This table contains the radial range for a 1.4 $M_\odot$ neutron star with the 1σ and 2σ confidence intervals. These radial ranges are not significantly different from the bounds with the unconstrained $M_{\rm max}$. The only caveat is that the neutron star models with 2.6 $M_\odot$ have extremely low probabilities.

In Appendix B, the mass and EOS posteriors from the intrinsic scattering models with $M_{\rm max} > 2.6$ $M_\odot$ limit are given in a tabular form. These tables list the radii for all neutron star mass ranges.

3.5 Correlation Analysis

Several EOS independent correlations for NS binaries have appeared in recent literature. This project tested the independence of these correlations based on the prior assumptions of EOSs. These universal relations can be used to infer binary parameters (such as the moment of inertia) from observations of tidal deformabilities [129] without knowing the internal structure of NS. These correlations can predict the spin of binary systems like the spin priors presented from the LIGO merger event GW170817. This work compared parameters from our posteriors with some of these relations for NS binaries. In a recent work, authors in Ref. [130] demonstrated the existence of a correlation between the antisymmetric tidal parameter, $\Lambda_{\rm a} = \Lambda_2 - \Lambda_1$, with the symmetric part, $\Lambda_{\rm s} = \Lambda_2 + \Lambda_1$.

$$\Lambda_{\rm a,yy} = F_{\rm n}^{(\Lambda_{\rm a})}(q)\Lambda_{\rm s}^{-\alpha}\frac{a + \sum_{\rm i=1}^{3}\sum_{\rm j=1}^{2} b_{\rm ij} q^{\rm j} \Lambda_{\rm s}^{-\rm i/5}}{a + \sum_{\rm i=1}^{3}\sum_{\rm j=1}^{2} c_{\rm ij} q^{\rm j} \Lambda_{\rm s}^{-\rm i/5}} \tag{3.2}$$

Eq. 3.2 is true for NS binaries with a mass ratio-dependent function given below,

$$F_{\rm n}^{(\Lambda_{\rm a})}(q) \equiv \frac{1 - q^{10/(3-\rm n)}}{1 + q^{10/(3-\rm n)}} \tag{3.3}$$

Here, n represents the number of polytropes in associated models. We compared the antisymmetric tidal deformability from our simulations with the correlation presented in Ref. [130] and these plots are shown in Fig. 3.9.

Ideally the fractional difference, $(\Lambda_{\mathrm{a}} - \Lambda_{\mathrm{a,yy}})/\Lambda_{\mathrm{a}}$, should reside near 0 within a good tolerance limit. Figure 3.9 shows that all our models overestimate values of Λ_{a} compared to $\Lambda_{\mathrm{a,yy}}$. 3p models tend to vary from 0 to +20% while 4L models shows larger deviation of -10% to +30%. These ranges are measured within a 2σ confidence limit.

Another exciting feature of tidal deformability in NS binaries is documented in Ref. [27]. The dimensionless tidal deformability of binaries can be determined using the mass ratio q with appropriate proportionality constant α ($\alpha = 1$ in these calculations).

$$\Lambda_{\mathrm{rat}} = \frac{\Lambda_1}{\Lambda_2} = \alpha q^6 \tag{3.4}$$

In Fig. 3.10, tests were done to compare the variation of mass ratio powered 6 with the ratio of tidal deformabilities for all our models.

Our models underestimate q values for low ranges of Λ_{rat} and, fractional differences, $(q^6 - \Lambda_{\mathrm{rat}})/\Lambda_{\mathrm{rat}}$, are given in the above figure. Limits imposed on chirp mass, $\mathcal{M}$, and symmetric mass ratio, η, in our simulations, don't allow values lower than 0.6 for q. Also, equilibration of the individual chain might impact these correlations.

Compactness of a NS has the relation $C = M/R$ in natural units ($G = c = 1$). As it turns out, the EOS is highly dependent on how compact these stars are. Ref. [80] gave a correlation between the compactness and tidal deformability of NS and the correlation plots are given in appendix C.

$$C_{\mathrm{i}} = 3.71 \times 10^{-1} - 3.91 \times 10^{-2} \ln \Lambda_{\mathrm{i}} + 1.056 \times 10^{-3} (\ln \Lambda_{\mathrm{i}})^2. \tag{3.5}$$

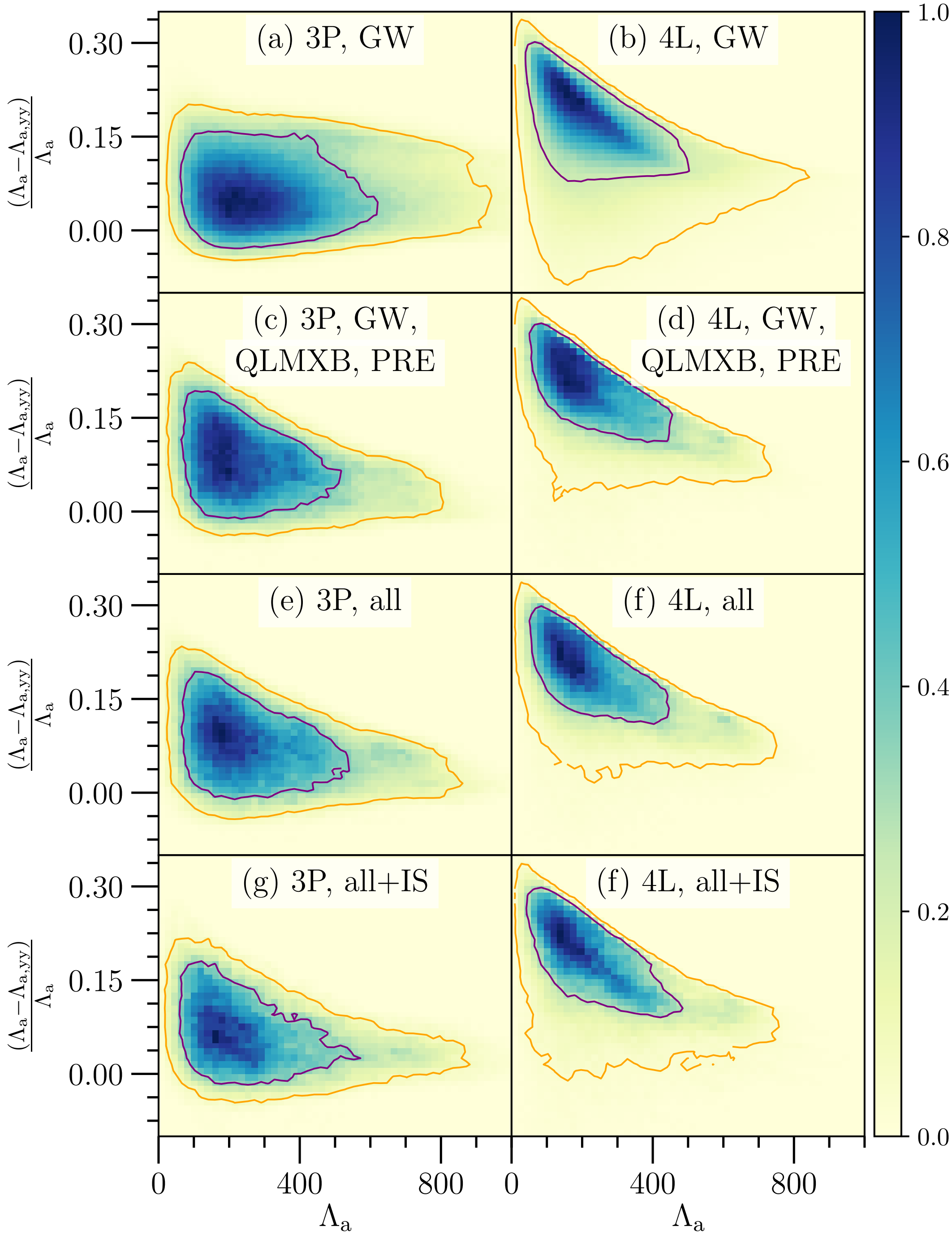

Figure 3.9: Posterior distributions for the deviations between $\tilde{\Lambda}_a$ and $\tilde{\Lambda}_{a,YY}$ versus $\tilde{\Lambda}_a$.

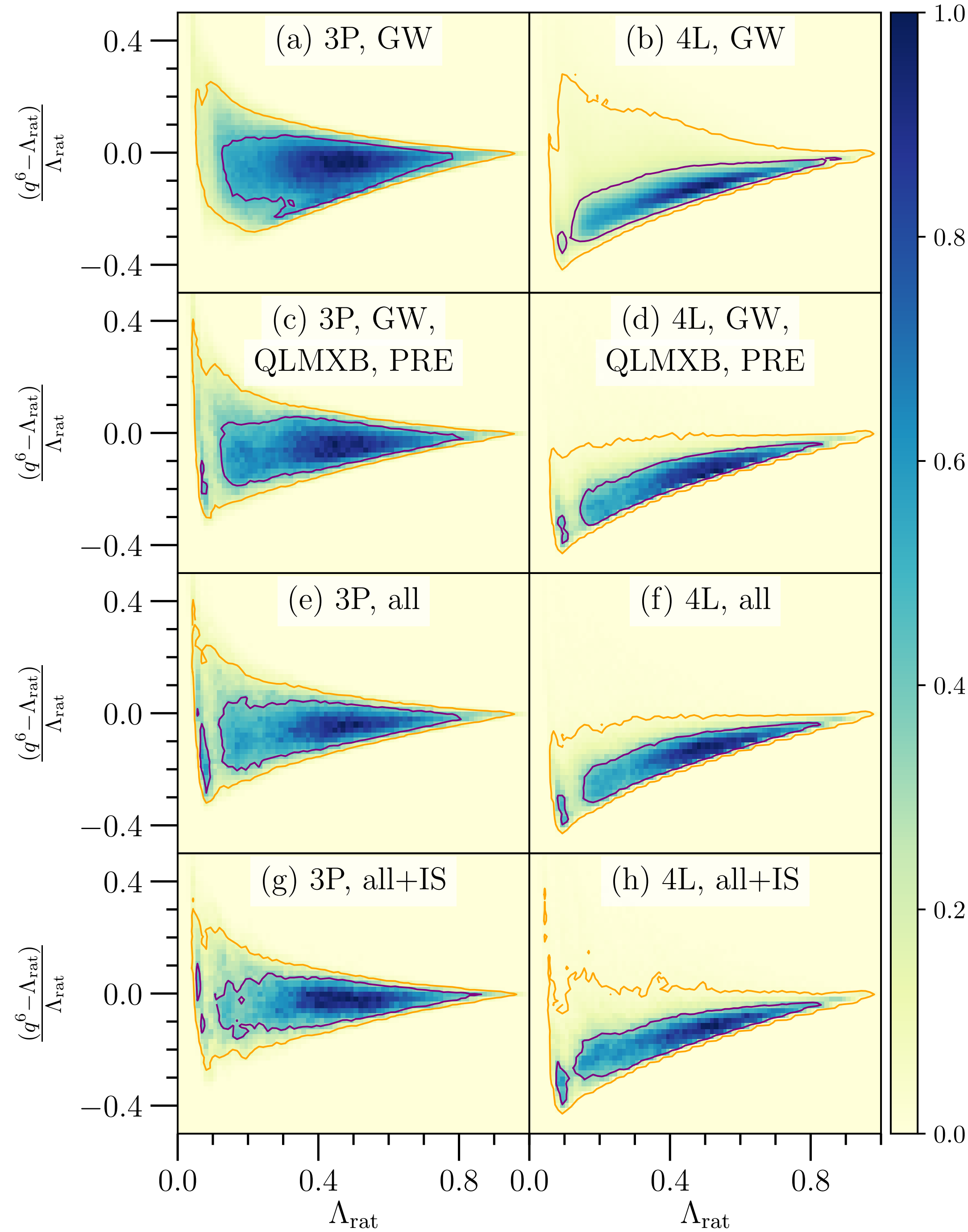

Figure 3.10: Posterior distributions for the deviations between $\Lambda_{\rm rat}$ and q^6 versus $\Lambda_{\rm rat}$.

The radius of a 1.4 solar mass neutron star can be correlated to the slope of symmetry energy L. This correlation is cited in Ref. [69]. Authors in Ref. [114] also pointed out that the correlation between $R_{1.4}$ and L depends on the EOS prior distribution. The joint posteriors given in Fig. 3.11 provide the correlation plot for L versus $R_{1.4}$. Adding the EM data weakens this correlation which is because of the strong constraint on R. Another correlation has also been suggested between the maximum mass of neutron star $M_{\max}$ and the corresponding radius [22]. The correlation between $R_{1.4}$ and $M_{\max}$ is relatively weak. Figure 3.12 shows the posteriors for these correlations. Pearson correlation coefficients are computed for these two correlations, and the coefficients are given in Table 3.5. Correlation coefficients between 0.9 and 1.0 indicate that variables are very highly correlated, coefficients between 0.7 and 0.9 are highly correlated, 0.5 and 0.7 indicate moderate correlation and, the range of $0.3 - 0.5$ indicate variables have a low correlation. Anything less than 0.3 represents little to no (linear) correlation. Coefficients in Table 3.5 indicates a low correlation between neutron star maximum mass with radius. Models with 3P EOS have correlations between L and $R_{1.4}$ and, the 4L EOS parameterizations have much weaker correlations.

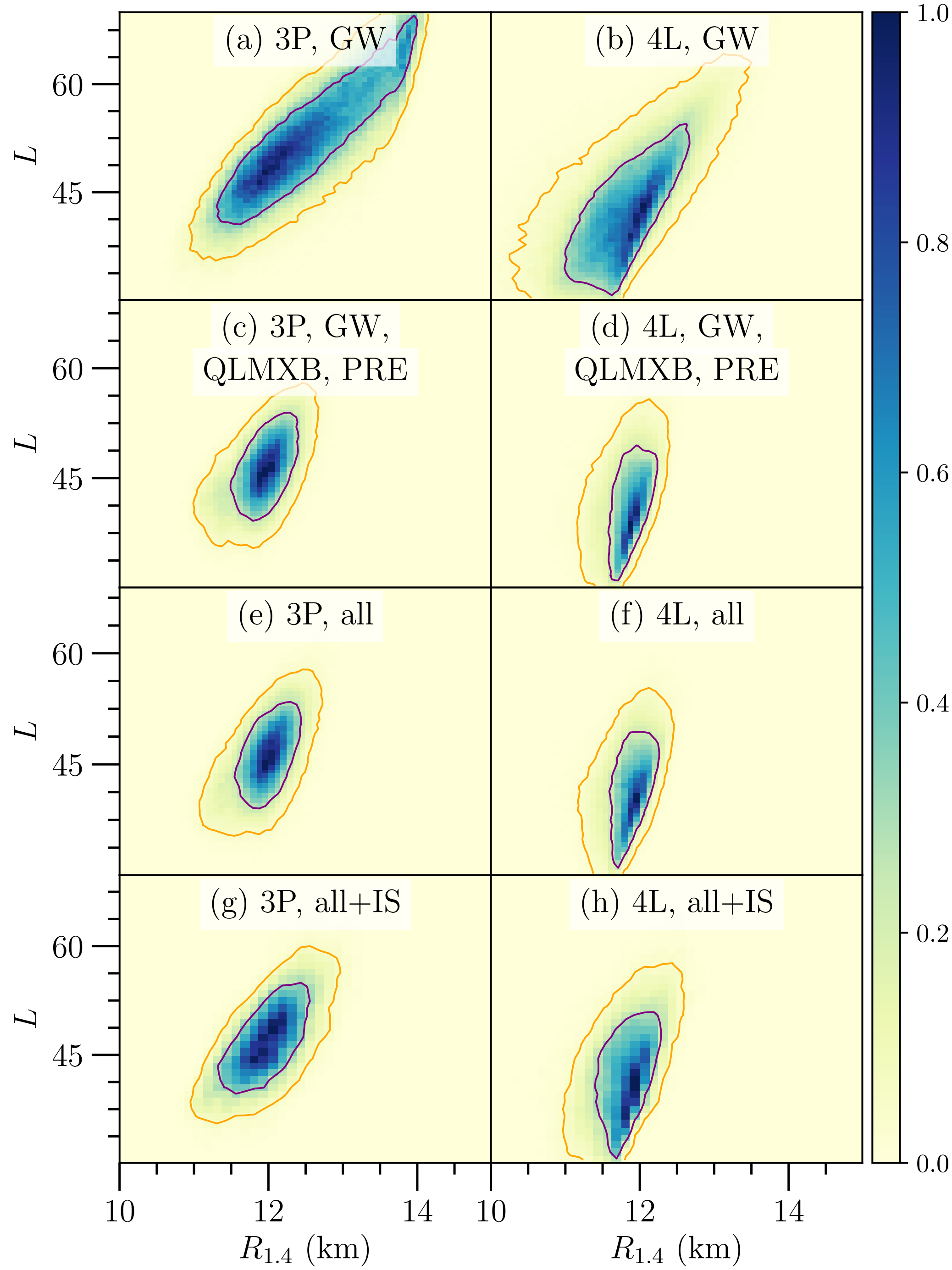

Figure 3.11: Posterior distributions demonstrating the cross correlation between $R_{1.4}$ and EOS parameter L.

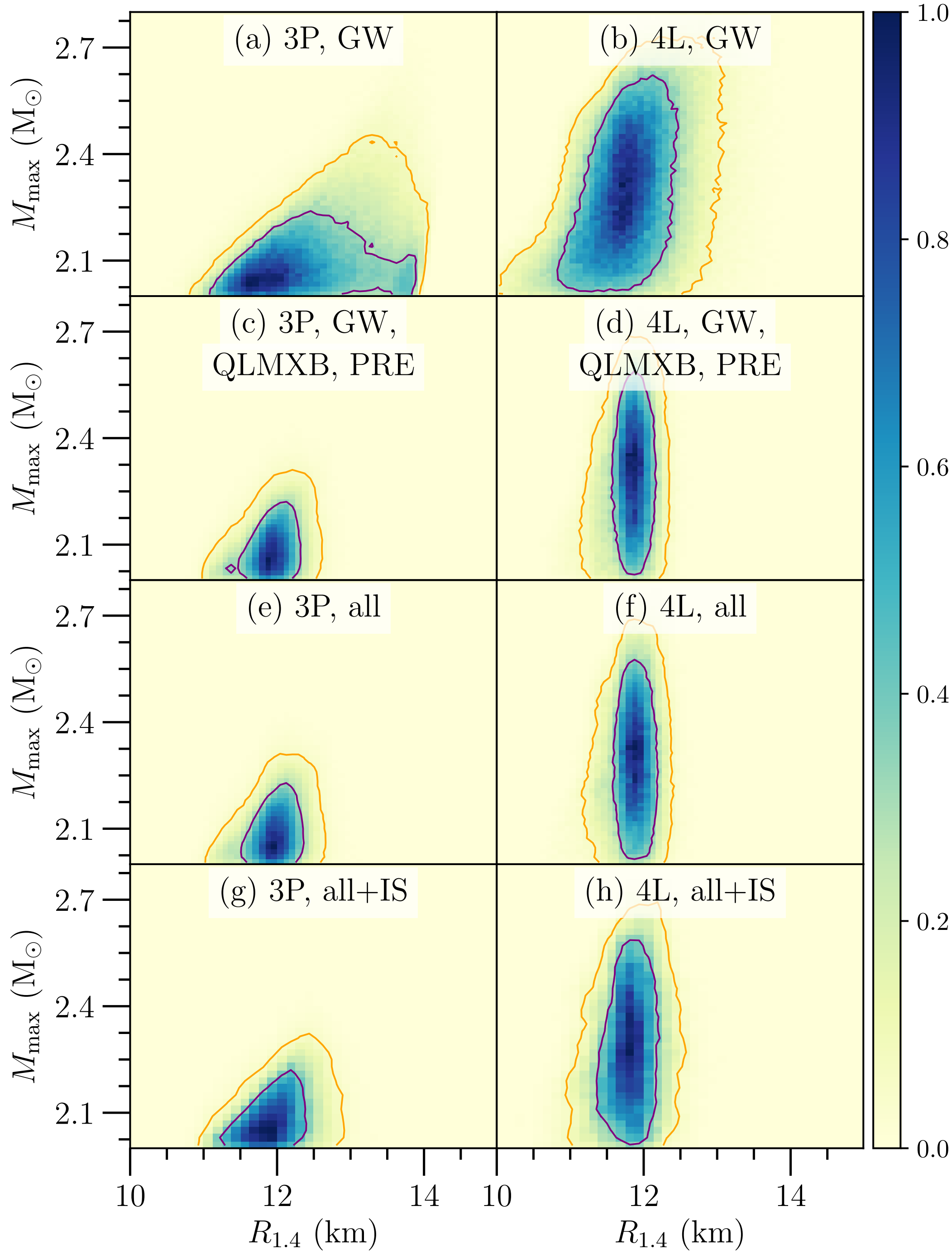

Figure 3.12: Posterior distributions demonstrating the cross correlation between $R_{1.4}$ and M_{max}.

Table 3.5: Pearson correlation coefficients between the radius of 1.4 solar mass neutron star with the neutron star maximum mass M_{max} and the slope of symmetry energy L.

Model	M_{max} vs $R_{1.4}$	L vs $R_{1.4}$
(a) 3P, GW	0.397	0.842
(b) 4L, GW	0.420	0.704
(c) 3P, GW, QLMXB, PRE	0.315	0.558
(d) 4L, GW, QLMXB, PRE	0.167	0.436
(e) 3P, all	0.283	0.575
(f) 4L, all	0.109	0.454
(g) 3P, all+IS	0.381	0.667
(h) 4L, all+IS	0.175	0.496

Chapter 4

Model Enhancements

There are always opportunities to update and upgrade the models described in the earlier chapters. Also, several different methods are out there to enhance a model and its predictability. Adding new data, adding new features, reducing prior biases, and taking notes of the outliers are some of the basic schemes that can be implemented to improve the models further. For neutron stars, the explicit implementation of rotations along the axis and non-radial pulsations due to the fluid motion are some of the possible enhancements out there. This chapter will present a couple of such cases that can be used to update the NS model.

4.1 Emulators

An emulator is not a replacement for simulation, but emulators can help speed up the overall simulation process. The emulators used in this project are built by selecting all possible functions over a given dataset. Compared to the time needed to generate samples from simulations, sampling from emulators are instantaneous. These samples will be used for the Bayesian inference afterwards. Therefore, an emulator can select possible combinations of parameter values rather than simulate the whole parameter space.

A model based on supervised learning is the first step to build a successful emulator. Supervised learning is mapping a function between input parameters to the outputs based on the example data. In machine learning, the inputs form the training parameters, and the outputs are called the labels of these parameters. The trained emulator can be used to predict the labels for a new combination of parameters.

4.1.1 Gaussian Process

The most critical part of supervised learning is to select an appropriate model to train. The model selected for this project is the Gaussian process (GP) [99, 127]. A Gaussian process generates all possible functions from the given dataset. These functions form a collective distribution of multivariate Gaussian.

$$f(X) \sim GP\,(\ m(X),\ \ k(X, X')\ ) \tag{4.1}$$

Here, X represents the vector with parameter values, (X, X') shows all possible pairs from X, $m(X)$ provides the mean vector and, $k(X, X')$ calculates the covariances (kernel) of the system. It is preferable to use Gaussian distributions to represent real-world data because of the Central Limit Theorem, which states that the samples from a non-normalized distribution still form a normal distribution with proper normalizations. So, any real-world data with finite mean μ and variance Σ can be written in the Gaussian form.

$$\mathcal{N}(\mu, \Sigma) \sim \mathcal{P}(X|\mu, \Sigma) = \frac{1}{\sqrt{2\pi\Sigma}}\ exp\left\{-\frac{1}{2}\left((X-\mu)^T\Sigma(X-\mu)\right)\right\} \tag{4.2}$$

A user-defined kernel function $k(X, X')$ can be used to determine the covariance matrix Σ. If the labels of these training parameters are given as vector Y, a joint posterior distribution is needed to map the relation between X and Y. Another benefit of using Gaussian distribution is that the joint posterior from the Two Gaussian functions returns a function in Gaussian form.

$$\mathcal{N}(\mu_3, \Sigma_3) = \mathcal{N}(\mu_1, \Sigma_1)\mathcal{N}(\mu_2, \Sigma_2) \tag{4.3}$$

Where the combined mean and covariance have the following forms,

$$\mu_3 = \frac{\Sigma_2\mu_1 + \Sigma_1\mu_2}{\Sigma_1 + \Sigma_2} \tag{4.4}$$

$$\Sigma_3 = \frac{\Sigma_1\Sigma_2}{\Sigma_1 + \Sigma_2} \tag{4.5}$$

For a test vector X_*, the predictive model based on Eq. 4.1 becomes

$$\begin{bmatrix} f(X) \\ f(X_*) \end{bmatrix} = \mathcal{N}\left(\begin{bmatrix} \mu \\ \mu_* \end{bmatrix}, \begin{bmatrix} k(X,X) & k(X,X_*) \\ k(X_*,X) & k(X_*,X_*) \end{bmatrix}\right) \tag{4.6}$$

4.1.2 Model Implementation

There are lots of well-known tools out there for machine learning. For this current work, a Gaussian Process Regression (GPR) model from scikit-Learn [47, 90, 125] has been implemented. A regression model uses statistical processes to define a relation between the independent variables and the dependent outcomes. A regression model is trained in machine learning based on the paired relation between the training parameters and their labels. This trained model is then used to predict the labels for a different set of parameters. A Gaussian process regression model is non-parametric but, the kernel functions can be defined with one or many hyperparameters. These hyperparameters are not directly learned within the model but are used to control the learning process itself. The most commonly used kernel functions for Gaussian process are Radial Basis Function kernel,

$$k(X, X') = \exp\left(-\frac{||X - X'||^2}{2l^2}\right) \tag{4.7}$$

Rational Quadratic kernel,

$$k(X, X') = \left(1 + \frac{||X - X'||^2}{2\alpha l^2}\right)^{-\alpha} \tag{4.8}$$

Exp-Sine-Squared kernel,

$$k(X, X') = \exp\left(-\frac{2sin^2\left(\pi||X - X'||^2/p\right)}{l^2}\right) \tag{4.9}$$

and Dot-Product kernel.

$$k(X, X') = \sigma_0^2 + X.X' \tag{4.10}$$

Here, X and X' represents data vectors. The Dot-Product kernel in Eq. 4.10 uses the predefined variance σ_0^2 as hyperparameter. All other kernels mentioned above use the length scale l between two adjacent points as a hyperparameter. Along with this length scale, the Rational Quadratic kernel has one extra mixing parameter α and, the Exp-Sine-Squared kernel uses the periodicity p to parameterize the covariances. Any one of these kernel functions (i.e., Rational quadratic kernel, Exp-Sine-Squared kernel, Etc.) is equally applicable in the

Gaussian process. Several predefined metric functions are available in scikit-learn, which can be used to decide the best kernel for GPR. In this work, root mean squared error is used to test the model's accuracy based on different kernels. For n sample points, if Y is the vector with accurate values for the test parameters and the model predicted values are given in Y', then the accuracy score of the prediction is defined as

$$RMSE = \sqrt{\frac{1}{n}\sum_{i=1}^{n}(Y - Y')^2} \tag{4.11}$$

The best score achievable is 0.0, while the worst will be closer to 1.0. In practice, a combination of different kernels can also be used in a single model. A rigorous test on these combinations can be performed in the future. For now, a Radial Basis Function (RBF) has been selected as the kernel. Equation 4.7 has the form of a Gaussian distribution which is another reason to chose the RBF kernel for Gaussian process regression.

The value of the hyperparameter can also affect the accuracy of the model. The RBF kernel can use any value for l but, too large or too small l value can misrepresent the relationship between data points. This misrepresentation can be tested with a couple of extreme values of l. For $l = 1$, Eq. 4.7 goes to zero for all values of $||X - X'||^2 \geq 4$, which means that any two points with a distance greater than four are considered uncorrelated. In the case of $l = 0.01$, the RBF is peaked at value zero, and nearly no correlation can be established between the points. This scenario of no correlation can also be reversed for a large value of l. For example, RBF can show a correlation between points with a distance of 100 for $l = 10$. The best way to determine the value of the hyperparameter is to use an optimizer function.

The purpose of an optimizer is to test all values of the hyperparameter in a given interval and return a value within the interval with the best possible score. The log-likelihood of the model based on Gaussian distribution is written as,

$$\log(\mathcal{P}(X, X') = -\frac{1}{2}\log(2\pi k(X, X')) - \frac{1}{2}(X - X')^{\mathrm{T}}k(X, X')(X - X') \quad (4.12)$$

Optimizer function selects different values for kernel hyperparameter from the given range, calculates the likelihood values and, tries to minimize the likelihood. An optimizer can also test the predictability of a model by using cross-validation. Cross-validation works by randomly splitting the training points into train-test sets and using them to measure the score for each split. However, a gradient-based optimizer uses a large amount of device memory, and the volume of required resources gets exponentially large with extended training points. Based on the tests done in this work, SciPy optimizers failed to minimize 4000 training samples in a machine with 16 gigabytes of memory. Rather than using optimizers, an exhaustive grid search can be used to find the best value for the hyperparameter and, an implementation of the "GridSearchCV" function from scikit-learn is used for this project.

4.1.3 Preliminary Results

Simulation results from model "3P, GW" has been chosen to test emulator implementation. In the Markov Chain Monte Carlo simulations, the randomly selected parameters are used to calculate the likelihood and, this likelihood is used in the Metropolis-Hastings algorithm. Calculating the likelihood is time-consuming, and a large number of points get rejected during the validation process. Rather than doing the total likelihood calculation, a trained emulator is used to predict the desired value for each random sample from the parameter space.

The model parameters are used as training parameters while the likelihood, radius of 1.4 $M_\odot$ neutron star, $M_{\max}$, and the speed of sound squared c_s^2 are used for parameter labels. $M_{\max}$ and c_s^2 is used to check the consistency of the predicted likelihood. The predicted likelihood will get rejected if the predicted $M_{\max} < 2.0$ and the predicted c_s^2 is bigger than one or smaller than zero.

A test dataset was created from the simulation results to test the accuracy of the model prediction. Figure 4.1 shows the comparison plot for test likelihood with the predicted ones. For model "3P, GW", emulator predictions are relatively accurate. A mass-radius posterior is also made from the emulated points, and this plot is shown in Fig. 4.2.

Apart from models "3P, GW" and "4L, GW", all other previously defined models include neutron star observations. For each of these NS sources, an additional mass parameter and an atmospheric parameter must be included with the training parameters. The issue arises with the atmospheric parameter as it is a binary variable representing 1 or 0 for the helium or the hydrogen atmosphere. Usually, logistic regression or classification models are used for binary variables. Therefore, it is necessary to test whether the atmospheric parameters are suitable for Gaussian process regression or a mixed model with Gaussian process classification and GPR for the NS observations models.

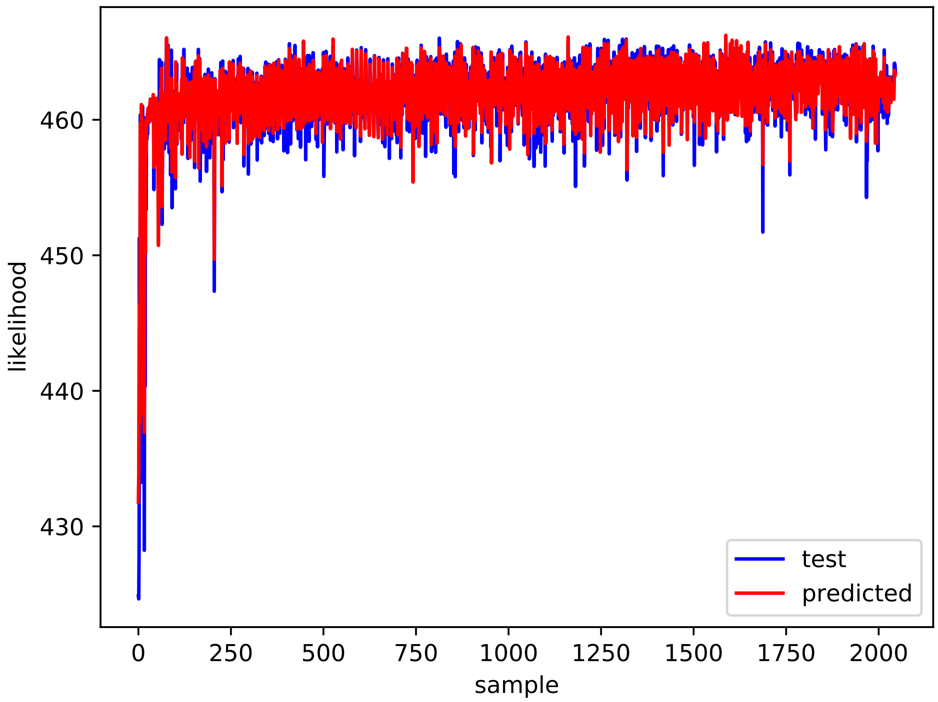

Figure 4.1: Comparison plot for test outputs with the predicted ones.

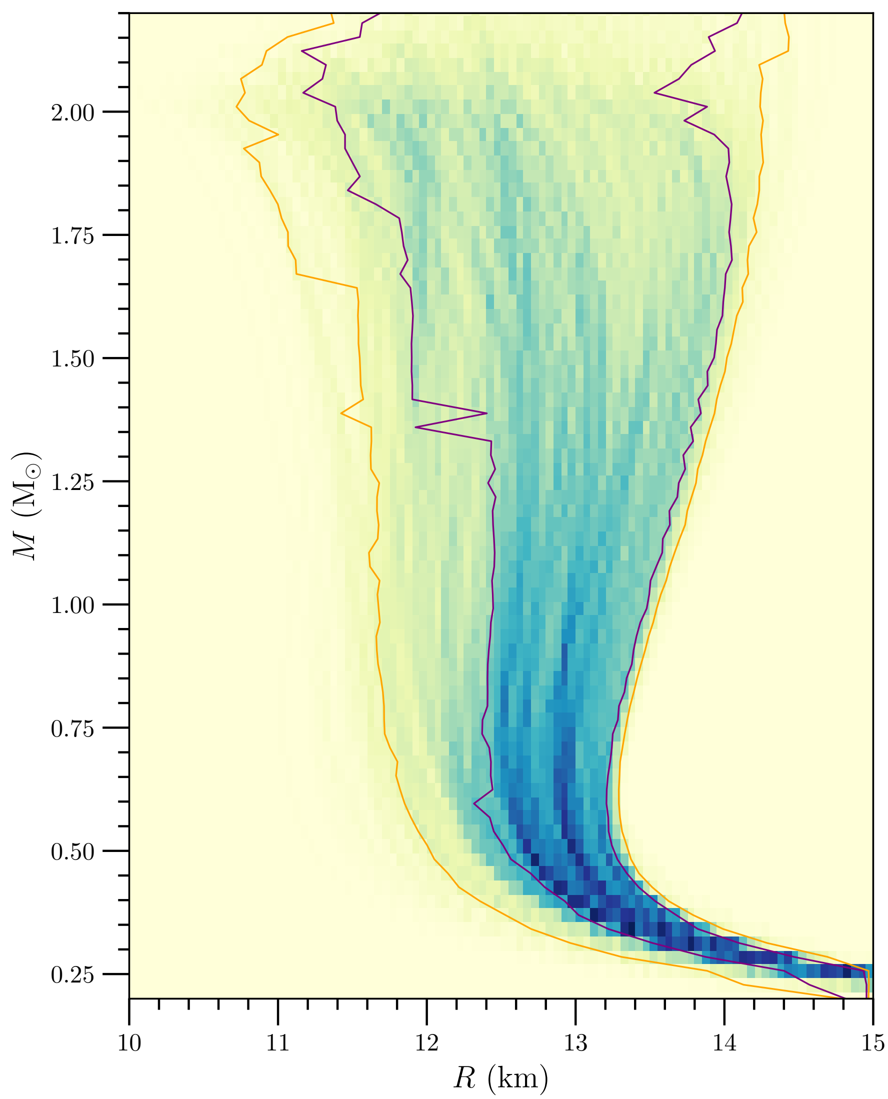

Figure 4.2: Mass-radius posteriors for model "3P, GW" from emulated points.

4.2 Non-Radial Pulsations of Neutron Star

There are several external means of excitation that can initiate oscillations within a neutron star [33]. Some of them are the energy released during the core-collapse supernova, energy from the infalling accreted matter in binaries, gravitational radiation from the binary inspiral, and the phase transition within the star's core. Neutron star oscillations can be divided into two major classes, radial modes and non-radial modes [46].

The star periodically oscillates along the radial axis in radial modes, and the spherical symmetry is kept conserved. The main driving force of this type of oscillation is the pressure gradient inside the star and, this mode is referred to as the p-mode.

The non-radial oscillations occur when the gas or liquid inside the star gets displaced. This kind of displacement creates deviations in spherical symmetry. Gravity acts as the restoring force in this type of oscillation. Hence, this form of oscillation is named g-mode. The spherical harmonics can characterize a non-radial oscillation with a small amplitude.

$$Y_l^m(\theta,\phi) \propto \pi_{\mathrm{p}} P_l^{|m|}(\cos\theta) e^{im\phi} \tag{4.13}$$

Here, θ and ϕ are polar and azimuthal angle respectively. The value of l and m determine the associated harmonics. π_{p} is the parity of the harmonics which can either be odd or even.

$$\pi_p = \begin{cases} (-1)^{l+1} & \text{odd parity} \\ (-1)^l & \text{even parity} \end{cases} \tag{4.14}$$

The small-amplitude pulsations can create nodes n within the system. The fundamental mode or the f-mode oscillations are described for all harmonics with $n = 0$, $m = 0$ and, $l \geq 0$.

4.2.1 f-mode Analysis

Different values of l in f-mode determine the type of pulsations within the star. If $l = 0$, the f-mode becomes equivalent to the radial mode, and it can be shown from the spherical harmonics.

$$P_0^0(\cos\theta) = 1 \tag{4.15}$$

For $l = 1$, the oscillation corresponds to the dipole mode. This dipole motion in f-mode is not possible as it requires deviations in the center of mass of the star. Therefore, the lowest order f-mode oscillation is observed for $l = 2$. The line element in equilibrium is given as,

$$(ds^2)_0 = e^{\nu} dt^2 - e^{\lambda} dr^2 - r^2(d\theta^2 + \sin^2\theta d\phi^2) \tag{4.16}$$

Authors in Ref. [118] showed that the non-radial perturbation in neutron star interior could be described with the fluid displacement vector ξ_α and ten equations from the metric perturbation $h_{\alpha\beta}$. Reference [118] also showed that only the even parity condition could have non-zero fluid displacements. The perturbed line element will be,

$$ds^2 = (ds^2)_0 + h_{\alpha\beta} dx^\alpha dx^\beta \tag{4.17}$$

The perturbation metric over here can be written as,

$$h_{\alpha\beta} = \begin{bmatrix} H_0 e^{\lambda} & H_1 & 0 & 0 \\ H_1 & H_2 e^{\lambda} & 0 & 0 \\ 0 & 0 & r^2 K & 0 \\ 0 & 0 & 0 & r^2 \sin^2\theta K \end{bmatrix} P_l(\cos\theta) \tag{4.18}$$

Here, H_0, H_1, H_2, and K are functions of time and radius. All these perturbations are not independent, and H_2 can be defined by the other three. Authors in Ref. [77] showed that with appropriate gauge, the time component of ξ_α will be zero $\xi_t = 0$ and only the spatial components will contribute to the perturbation. Also, the perturbations get damped over time, and this damping phenomenon is determined by the complex frequency ω. Three spatial components of the fluid displacement vector are given as,

$$\xi_r = \frac{e^{-\lambda/2}}{r^{1-l}} W Y_l^m e^{i\omega t} \tag{4.19}$$

$$\xi_\theta = -r^{l-2} V \partial_\theta Y_l^m e^{i\omega t} \tag{4.20}$$

$$\xi_\phi = -\frac{r^{l-2}}{\sin^2\theta} V \partial_\phi Y_l^m e^{i\omega t} \tag{4.21}$$

$V(r,t)$ and $W(r,t)$ are fluid displacement vectors. Reference [77] also calculated the equations of motion based on the perturbation parameters and showed the recipe to solve these equations with a given equation of state. Article [77] defined a new perturbation function X in terms of H_0, V, W, pressure p, and density ρ.

$$X = \omega^2 (p+\rho) e^{-\nu/2} V - \frac{p'}{r} e^{(\nu-\lambda)/2} W + \frac{1}{2}(p+\rho) e^{\nu/2} H_0 \tag{4.22}$$

The prime notation over p defines the pressure derivatives in terms of r. The function defining the relationship between all the perturbations in the f-mode analysis is given as,

$$\begin{aligned} H_0 &= \frac{1}{3m+\frac{1}{2}(l+2)(l-1)r+4\pi r^3 p}\,[8\pi r^3 e^{-\nu/2}X \\ &\quad -\left\{\frac{1}{2}(l+1)(m+4\pi r^3 p)-\omega^2 r^3 e^{-(\lambda+\nu)}\right\}H_1 \\ &\quad +\left\{\frac{(l+2)(l-1)r}{2}-\frac{\omega^2 r^3}{e^{\nu}}-\frac{e^{\lambda}(m+4\pi r^3 p)(3m-r+4\pi r^3 p)}{r}\right\}K] \end{aligned} \tag{4.23}$$

Here, m is the enclosed mass of the star with a specific value of r. Equations 4.22 and 4.23 can be used to reduce the number of free parameters, and the system of equations will consist of four ODEs with H_1, K, W and X. These ODEs are independent of parameter t but depend explicitly on r.

$$\begin{aligned} H_1' &= -\frac{1}{r}\left[l+1+\frac{2me^{\lambda}}{r}+4\pi r^2 e^{\lambda}(p-\rho)\right]H_1 \\ &\quad +\frac{e^{\lambda}}{r}\left[H_0+K-16\pi(p+\rho)V\right] \end{aligned} \tag{4.24}$$

$$\begin{aligned} K' &= \frac{H_0}{r}+\frac{l(l+1)}{r}H_1-\left[\frac{l+1}{r}-\frac{\nu'}{2}\right]K \\ &\quad -8\pi(p+\rho)\frac{e^{\lambda/2}}{2}W \end{aligned} \tag{4.25}$$

$$W' = -\frac{(l+1)}{r}W+re^{\lambda/2}\left[\frac{X}{\gamma\ p\ e^{\nu/2}}-\frac{l(l+1)}{r^2}V+\frac{H_0}{2}+K\right] \tag{4.26}$$

$$\begin{aligned} X' &= -\frac{l}{r}X+\frac{(p+\rho)e^{\nu/2}}{2}\left[\frac{1}{r}-\frac{\nu'}{2}H_0\right] \\ &\quad +\frac{(p+\rho)e^{\nu/2}}{2}\left[\frac{r\omega^2}{e^{\nu}}+\frac{l(l+1)}{2r}\right]H_1 \\ &\quad +\frac{(p+\rho)e^{\nu/2}}{2}\left[\frac{3\nu'}{2}-\frac{1}{r}\right]K-\frac{(p+\rho)e^{\nu/2}}{2}\frac{l(l+1)\nu'}{r}V \\ &\quad -\frac{(p+\rho)e^{\nu/2}}{r}\left[4\pi(p+\rho)e^{\lambda/2}+\omega^2 e^{(\lambda/2-\nu)}\frac{r^2}{2}\left(\frac{\nu'}{r^2 e^{\lambda/2}}\right)'\right]W \end{aligned} \tag{4.27}$$

Here, γ is the adiabatic constant for the given EOS.

$$\gamma = \left(\frac{p+\rho}{p}\right)\frac{dp}{d\rho} \tag{4.28}$$

The boundary conditions for these ODEs are also given in Ref. [77].

$$K(0) = \pm(p_0+\rho_0) \tag{4.29}$$

$$W(0) = 1 \tag{4.30}$$

$$H_1(0) = \frac{\{2lK(0)+16\pi(p_0+\rho_0)W(0)\}}{l(l+1)} \tag{4.31}$$

$$X(0) = (p_0+\rho_0)e^{\nu_0/2}\left\{\frac{K(0)}{2}+\left[\frac{4\pi(3p_0+\rho_0)}{3}-\frac{\omega^2}{le^{\nu_0}}\right]W(0)\right\} \tag{4.32}$$

As it is evident from the expressions of the ODEs, the solutions are singular at $r = 0$. Also, the singularity occurs when the frequency becomes equal to the values given in the equations below.

$$\omega^2 = \frac{1}{2}l(l+1)e^{(\lambda+\nu)}\left[\frac{m}{r^3}+4\pi p\right] \tag{4.33}$$

$$\omega^2 = \frac{1}{4}l(l+1)\frac{1}{r}\frac{d}{dr}e^{\nu} \tag{4.34}$$

To solve this system of equations [4.24–4.27] at $r = 0$, a power series solution near 0 is necessary [30]. Therefore at $r \sim 0$,

$$H_1(r) = H_1(0)+\frac{r^2}{2}H''(0) \tag{4.35}$$

$$K(r) = K(0)+\frac{r^2}{2}K''(0) \tag{4.36}$$

$$W(r) = W(0)+\frac{r^2}{2}W''(0) \tag{4.37}$$

$$X(r) = X(0)+\frac{r^2}{2}X''(0) \tag{4.38}$$

The first-order derivatives vanish at $r = 0$ and the higher order corrections $\mathcal{O}(r^4)$ are omitted in the calculation. Values for $H_1(0)$, $K(0)$, $W(0)$ and, $X(0)$ are given as the boundary conditions. The second-order derivatives can be computed numerically.

$$AY''(0) = BY(0) \tag{4.39}$$

Where, Y is a vector with parameters H_1, K, W and, X. A and B are 4×4 matrices. Pressure and densities need to be expanded in respective power series to obtain the matrix elements for A and B.

$$p(r) = p_0 + \frac{r^2}{2}p_2 + \frac{r^4}{4}p_4 \tag{4.40}$$
$$\rho(r) = \rho_0 + \frac{r^2}{2}\rho_2 + \frac{r^4}{4}\rho_4 \tag{4.41}$$
$$\nu(r) = \nu_0 + \frac{r^2}{2}\nu_2 + \frac{r^4}{4}\nu_4 \tag{4.42}$$

Higher order p, ρ and, ν coefficients can be evaluated from the zeroth order ones.

$$p_2 = -\frac{4}{3}(p_0 + \rho_0)(3p_0 + \rho_0) \tag{4.43}$$
$$\rho_2 = \frac{p_2(p_0 + \rho_0)}{\gamma_0 p_0} \tag{4.44}$$
$$\nu_2 = \frac{8\pi}{3}(3p_0 + \rho_0) \tag{4.45}$$
$$p_4 = -\frac{2\pi}{5}(p_0 + \rho_0)(5p_2 + \rho_2) - \frac{2\pi}{3}(p_2 + \rho_2)(3p_0 + \rho_0) - \frac{32\pi^2}{9}\rho_0(p_0 + \rho_0)(3p_0 + \rho_0) \tag{4.46}$$
$$\nu_4 = \frac{4\pi}{5}(5p_2 + \rho_2) + \frac{64\pi^2}{9}\rho_0(3p_0 + \rho_0) \tag{4.47}$$

With the coefficients for pressure and densities, the matrix elements for A are as follows:

$$
\begin{aligned}
A_{00} &= 0 && (4.48)\\
A_{01} &= -\frac{p_0+\rho_0}{4} && (4.49)\\
A_{02} &= \frac{1}{2}\left[p_2 + \left(\frac{p_0+\rho_0}{e^{\nu_0}}\right)\frac{\omega^2(l+3)}{l(l+1)}\right] && (4.50)\\
A_{03} &= \frac{1}{2}e^{-\nu_0/2} && (4.51)\\
A_{10} &= -\frac{1}{4}l(l+1) && (4.52)\\
A_{11} &= \frac{1}{2}(l+1) && (4.53)\\
A_{12} &= 4\pi(p_0+\rho_0) && (4.54)\\
A_{13} &= 0 && (4.55)\\
A_{20} &= \frac{1}{2}(l+3) && (4.56)\\
A_{21} &= -1 && (4.57)\\
A_{22} &= -8\pi(p_0+\rho_0)\left(\frac{l+3}{l(l+1)}\right) && (4.58)\\
A_{23} &= 0 && (4.59)\\
A_{30} &= -\frac{1}{8}l(l+1)(p_0+\rho_0)e^{\nu_0/2} && (4.60)\\
A_{31} &= 0 && (4.61)\\
A_{32} &= -(p_0+\rho_0)s^{\nu_0/2}\left[\frac{(l+2)\nu_2}{4} - 2\pi(p_0+\rho_0) - \frac{\omega^2}{2e^{\nu_0}}\right] && (4.62)\\
A_{33} &= \frac{1}{2}(l+2) && (4.63)
\end{aligned}
$$

The matrix elements of B are formulated with the coefficients of two new equations Q_0 and Q_1. These two equations are given as a linear combination of $Y(0)$.

$$Q_0 = Q_{0H_1}H_1(0) + Q_{0K}K(0) + Q_{0W}W(0) + Q_{0K}K(0) \qquad (4.64)$$

$$Q_1 = Q_{1H_1}H_1(0) + Q_{1K}K(0) + Q_{1W}W(0) + Q_{1K}K(0) \tag{4.65}$$

Coefficients from Eqs. 4.64 and 4.65 are given below.

$$Q_{0H_1} = -\frac{4}{(l+2)(l-1)}\left[\frac{2\pi}{3}l(l+1)(3p_0+\rho_0) - \frac{\omega^2}{e^{\nu_0}}\right] \tag{4.66}$$

$$Q_{0K} = -\frac{4}{(l+2)(l-1)}\left[\frac{8\pi\rho_0}{3} + \frac{\omega^2}{e^{\nu_0}}\right] \tag{4.67}$$

$$Q_{0W} = 0 \tag{4.68}$$

$$Q_{0K} = \frac{32\pi}{(l+2)(l-1)e^{\nu_0/2}} \tag{4.69}$$

$$Q_{1H_1} = 0 \tag{4.70}$$

$$Q_{1K} = \frac{3}{l(l+1)} \tag{4.71}$$

$$Q_{1W} = \frac{8\pi\rho_0}{3l} \tag{4.72}$$

$$Q_{1K} = \frac{2}{l(l+1)\ \gamma_0\ p_0\ e^{\nu_0/2}} \tag{4.73}$$

The matrix B is given as,

$$B_{00} = \frac{1}{4}(p_0+\rho_0)Q_{0H_1} + \frac{1}{2}(p_0+\rho_0)\frac{\omega^2}{e_{\nu_0}}Q_{1H_1} \tag{4.74}$$

$$B_{01} = \frac{1}{4}(p_2+\rho_2) + \frac{1}{4}(p_0+\rho_0)Q_{0K} + \frac{1}{2}(p_0+\rho_0)\frac{\omega^2}{e_{\nu_0}}Q_{1K} \tag{4.75}$$

$$\begin{aligned} B_{02} = {} & \frac{1}{4}(p_0+\rho_0)Q_{0W} + \frac{1}{2}(p_0+\rho_0)\frac{\omega^2}{e_{\nu_0}}Q_{1W} \\ & - \left\{p_4 - \frac{4\pi}{3}p_2\rho_0 + [p_2+\rho_2-(p_0+\rho_0)\nu_2]\frac{\omega^2}{2le^{\nu_0}}\right\} \end{aligned} \tag{4.76}$$

$$B_{03} = \frac{1}{4}(p_0+\rho_0)Q_{0X} + \frac{1}{2}(p_0+\rho_0)\frac{\omega^2}{e_{\nu_0}}Q_{1X} + \frac{1}{4}\frac{\nu_2}{e^{\nu_0/2}} \tag{4.77}$$

$$B_{10} = \frac{1}{2}Q_{0H_1} \tag{4.78}$$

$$B_{11} = \frac{1}{2}Q_{0K} + \frac{4\pi}{3}(3p_0+\rho_0) \tag{4.79}$$

$$B_{12} = \frac{1}{2}Q_{0W} - 4\pi\left[p_2+\rho_2+\frac{8\pi}{3}\rho_0(p_0+\rho_0)\right] \tag{4.80}$$

$$B_{13} = \frac{1}{2}Q_{0X} \tag{4.81}$$

$$B_{20} = \frac{1}{2}Q_{0H_1} - 8\pi(p_0+\rho_0)Q_{1H_1} + 4\pi\left[\frac{(2l+3)\rho_0}{3} - p_0\right] \tag{4.82}$$

$$B_{21} = \frac{1}{2}Q_{0K} - 8\pi(p_0+\rho_0)Q_{1K} \tag{4.83}$$

$$B_{22} = \frac{1}{2}Q_{0W} - 8\pi(p_0+\rho_0)Q_{1W} + \frac{8\pi}{l}(p_2+\rho_2) \tag{4.84}$$

$$B_{23} = \frac{1}{2}Q_{0K} - 8\pi(p_0+\rho_0)Q_{1K} \tag{4.85}$$

$$B_{30} = (p_0+\rho_0)e^{\nu_0/2}\left\{\frac{1}{4}Q_{0H_1} - \frac{1}{4}l(l+1)\nu_2 Q_{1H_1} + \frac{\omega^2}{2e^{\nu_0}}\right\} \tag{4.86}$$

$$B_{31} = (p_0+\rho_0)e^{\nu_0/2}\left\{\frac{1}{4}Q_{0K} - \frac{1}{4}l(l+1)\nu_2 Q_{1K} + \frac{nu_2}{2}\right\} \tag{4.87}$$

$$\begin{aligned} B_{32} = {} & (p_0+\rho_0)e^{\nu_0/2}\{\frac{1}{4}Q_{0W} - \frac{1}{4}l(l+1)\nu_2 Q_{1W} + \frac{1}{2}(l+1)\nu_4 \\ & -2\pi(p_2+\rho_2) - \frac{16\pi^2}{3}\rho_0(p_0+\rho_0) \\ & +\frac{1}{2}(\nu_4 - \frac{4\pi}{3}\rho_0\nu_2) + \frac{\omega^2}{2e^{\nu_0}}(\nu_2 - \frac{8\pi}{3}\rho_0)\} \end{aligned} \tag{4.88}$$

$$\begin{aligned} B_{33} = {} & (p_0+\rho_0)e^{\nu_0/2}\left\{\frac{1}{4}Q_{0K} - \frac{1}{4}l(l+1)\nu_2 Q_{1K}\right\} \\ & +\frac{l}{2(p_0+\rho_0)}\left[p_2+\rho_2+\frac{1}{2}(p_0+\rho_0)\nu_2\right] \end{aligned} \tag{4.89}$$

$Y''(0)$ is calculated numerically using matrices A and B in Eq. 4.39. This provides a complete solution overall ranges of r to the system of equations [4.24–4.27]. Solving these equations has various implications. Firstly, the frequency analysis of the f-mode can give a direct relationship with the compactness M/R of the star [77], and it might shed light on the time needed for the perturbation to dissipate. On the other hand, f-mode can directly be related to tidal deformations. Reference [54] showed that the tidal responses could arise from the perturbation in the Schwarzschild metric. The f-mode oscillations are also possible in binary inspirals. The frequency of the f-mode with the amplitude and damping time can be used to infer masses of the binary inspiral [25]. Authors in Ref. [55] showed that the maximum frequency $\omega_{\max}$ of the f-mode could be related to the orbital frequency Ω of the inspiral.

$$|m|\Omega = \omega_{\max} \tag{4.90}$$

A similar analysis to the ones done in section 3.5 will help test this universality relation given in Eq. 4.90. The frequency range of the f-mode is well known. The oscillation frequency varies between $1 \sim 3$ kHz. LIGO-VIRGO analysis provided the f-mode frequency for GW170817 between $1.67 \sim 2.18$ kHz, and the calculated damping time is $0.155-0.255$ s. Reference [126] used these information to measure the range of tidal deformability for a 1.4 $M_\odot$ neutron star, $\tilde{\Lambda}_{1.4} \in [70,\ 580]$. This calculation showed the possibility to constrain $\tilde{\Lambda}$ from the non-radial oscillations. Thus, studying the perturbations in neutron superfluid will be a major upgrade to the neutron star models presented in this dissertation.

4.3 A Brief Discussion on Other Possibilities

The inferences presented in Chapter 3 are based on a handful of neutron star observations. The QLMXBs and PREs used in this dissertation also do not cover all binaries. A comprehensive analysis should include the mass distributions from all neutron stars. References [68, 133] provide details on the mass distributions for different kinds of NS sources. The next step would be to include these distributions with the models presented in this dissertation.

Neutron stars with masses larger than the 2 $M_\odot$ has been observed, and more observations are pushing the maximum mass limit to the higher ranges. PSR J2215+5135 [76] has the mass upper limit of 2.44 $M_\odot$, and the upper limit of the measured mass from MSP J0740+6620 [26] is 2.24 $M_\odot$. Also, LIGO-VIRGO observation GW190814 [1] detected a compact object with 2.6 $M_\odot$ which can be, not confirmed yet, the highest mass of a neutron star ever observed [37, 117]. Therefore, a different approach is necessary to select the EOSs that can reach beyond these maximum mass $M_{\rm max}$ limit.

The stiffness of the EOS determines the maximum possible mass of a neutron star. In a polytropic EOS model, the adiabatic indices $\Gamma_{\rm i}$ manipulate the value of probable $M_{\rm max}$. Rather than using $\Gamma_{\rm i}$ as the model parameter, one can use $M_{\rm max}$. A simple variable transformation can also be done to relate $\Gamma_{\rm i}$ with $M_{\rm max}$.

$$M_{\rm max}(\Gamma_{\rm i}) \rightarrow \Gamma_{\rm i}(M_{\rm max}) \tag{4.91}$$

Similarly, a different variable transformation can be use used in the 4L line-segment (lns) models.

$$M_{\rm max}(lns_{\rm i}) \rightarrow lns_{\rm i}(M_{\rm max}) \tag{4.92}$$

Here, lns refers to the line segments. By doing these transformations in Eqs. 4.91 and 4.92, one can explicitly set the desired maximum mass in the analyses. Reference [45] discussed an hybrid EOS model to test the upper bound of $M_{\rm max}$. Their approach in combining soft and stiff EOSs may also be tested to reach the maximum mass of 2.6 $M_\odot$.

Chapter 5

Conclusions

The primary objective of this work was to analyze the neutron star structure using alternative forms of NS observations. This dissertation has presented a qualitative comparison between the electromagnetic and gravitational wave observations of neutron stars by performing joint analyses. The systematics such as the redshift correction z in the LIGO observation and the atmospheric constraints in quiescent low-mass X-ray binaries are adequately incorporated in this work. Although EM and GW observations are different in their respective forms of detection methods, it is evident that combining the resultant constraints from these measurements does provide better estimates of neutron star properties.

Chapter 2 of this dissertation lists various undertakings to reform the observed data for further analyses. Implementing an estimator to generate a dense grid from the GW170817 data made the GW input more statistically sound. Observational data from the X-ray sources were also modified with convolution operations, which were done to test the hidden systematic of these sources. The convolution operations, named intrinsic scattering (IS), took the mass-radius distributions from each source, and transformed the value from each grid point with the computed variances associated to that point and its neighbors. The chapter mentioned here also reports the equation of state parameterization for neutron stars. This project appropriately discussed the validity of both polytropic and line-segment EOSs. Furthermore, there is no firm evidence yet to disallow any one of these EOS priors.

The posteriors from the model analyses were presented in Chapter 3. A total of eight different models were simulated to demonstrate the effect from newer addition of NS sources. The data used in different models are gradually enhanced with different kinds of observations.

$$\text{GW} \rightarrow \text{GW, QLMXB, and PRE} \rightarrow \text{GW, all} \rightarrow \text{GW, all+IS}$$

This project referred to the combined X-ray sources from QLMXB, PRE, and NICER as "all". It was shown that the models corresponding to the GW dataset generated the least confined posterior distributions. Adding QLMXBs and PREs to GW greatly condenses the posteriors. The inclusion of NICER observation PSR J0030+451 had a different outcome. Rather than confining, the NICER dataset slightly broadens these distributions, albeit not noticeable in qualitative comparison. The posteriors from the IS models also have a broader spectrum than the "GW, all" models, but no new precise information can be ciphered from them.

A comparison figure [3.2] was made for the mass distributions from each of the NS sources used in this work. Among these sources, the NSs from GW170817 was the most precise. The plots containing the mass distributions by grouping the sources into their respective observation types were more informative than the individual ones. An exciting inference from these distributions has to be the upper limit of neutron star mass. Both QLMXB and PRE showed a tendency to extend far beyond the 2 $M_\odot$, which was the canonical mass limit for the minimum value of the maximum mass NS. The upper limit from these mass distributions implies that the current models can easily incorporate the newly discovered massive NSs with slight modifications.

The goal of the structural analysis was to constrain the tidal deformability and the radii of neutron stars. Models with the "GW, QLMXB, and PRE" dataset provide the best constraints for these two quantities. The tidal deformability range for a 1.4 $M_\odot$ neutron star with a 95% confidence limit is $\tilde{\Lambda}_{1.4} \in [227, 484]$ for the 3P EOS, and $\tilde{\Lambda}_{1.4} \in [237, 436]$ for the 4L. The radial range for $R_{1.4}$ is given as $[11.21\ \mathrm{km}, 12.55\ \mathrm{km}]$ and $[11.25\ \mathrm{km}, 12.39\ \mathrm{km}]$ for the 3P and 4L EOS priors, respectively.

Although the 4L EOS prior provide better constraints for $\tilde{\Lambda}_{1.4}$ and $R_{1.4}$, the 4L models in $\Lambda_2 - \Lambda_1$ [Fig. 3.3] and $M - R$ [Fig. 3.6] distributions show definite tendency to bend towards the low-radii limit for low-mass NSs. The 3P models are free of such biases, thus making the results from this prior more adequate. There is some beneficial aspect to the 4L EOS prior as well. The implicit phase transition within the 4L EOS allows the corresponding model to predict neutron stars with considerably larger masses than the 3P models. For example, Appendix B provides tables from the IS models that indicate the maximum probable NS mass for the 3P model is 2.4 $M_\odot$, while the 4L model can go up to 2.7 $M_\odot$. The probability of getting to the 2.7 $M_\odot$ mass range currently makes the 4L EOS prior a better choice for performing analysis on the 2.6 $M_\odot$ neutron star candidate from GW190814. With proper conditioning, the polytropic models can achieve a higher maximum mass value. It is just that the probability is extremely low to get a neutron star model that supports 2.6 $M_\odot$ with the current 3P EOS parameterization.

This project also presented quantitative comparisons to test the validity of a couple of EOS independent quantities in the NS binaries. The first check was performed on the anti-symmetric part of the tidal deformabilities $\tilde{\Lambda}_{\mathrm{a}}$ from all eight models with the parameterized one $\tilde{\Lambda}_{\mathrm{a,YY}}$ based on Ref. [130]. The deviations between these two quantities are nearly 20% with a 2σ confidence limit for the 3P models, and the disparity is even higher for the 4L. Therefore, it is evident that $\tilde{\Lambda}_{\mathrm{a}}$ is not entirely independent of the EOS prior.

The relationship between the mass ratio q and the ratio of individual tidal deformability is also speculated as EOS independent [27]. The deviations $q^6 - (\Lambda_1/\Lambda_2)$ calculated from the model posteriors are significantly large, $\sim 40\%$ for a 2σ C.I., which also did not support the prior independence.

Reference [80] showed that the compactness C_{i} of the individual neutron star in the binaries can be paraemterized with its tidal deformation. This project calculated the variations between the parameterized C_{i} and $M_{\mathrm{i}}/R_{\mathrm{i}}$, which is less than 10% with a 2σ limit.

The Pearson correlation tests in section 3.5 provided insight on the relationship between the neutron star radius R with the slope of the symmetry energy L and the maximum mass $M_{\mathrm{max.}}$. It was shown in Chapter 3 that L is moderately correlated to R in the 3P models, but the 4L models did not indicate any correlation between these two parameters. Also, M_{max} is nearly independent of R for all EOS priors.

Chapter 4 was constructed to demonstrate the future possibilities of neutron star research. Data-driven neutron star modeling is undoubtedly qualified to take advantage of machine learning methods such as supervised learning. In section 4.1

a preliminary implementation of machine learning in the current neutron star models was discussed. This implementation of the emulator was done to reduce the overall computation cost of simulations. For example, an emulator can filter out a subset in parameter space with a similar likelihood of the training data, thus reducing the need to simulate the entire space. The accuracy test of the emulator output based on the "3P, GW" model showed excellent outcomes and, the initial mass-radius constraints for this model are also given in the section mentioned here.

Non-radial pulsations of neutron stars, mainly f-mode, can provide valuable insight into tidal structures. Section 4.2 discussed the analytical details on the f-mode analysis, thus relating the compactness of the neutron star with oscillation frequencies. Furthermore, it was shown in a couple of recent works that the f-mode frequency range $1-3$ kHz varies from the radial oscillations and, the radio signal from the LIGO observations can be used to relate the tidal deformability $\tilde{\Lambda}$ with the pulsation mode corresponding to the $l=2$ spherical harmonics [54, 126]. Therefore, f-mode is genuinely significant to neutron star structure analysis.

Another planned update to the current neutron star models is to explicitly use the minimum value of the maximum mass neutron star $M_{\max}$ as the model parameter. The linear transformations relating $M_{\max}$ with the EOS parameters were briefly discussed in section 4.3. Moreover, it is imperative to include mass distributions from all classes of neutron stars to upgrade the models presented in this dissertation.

5.1 Final Remarks

The models presented in this dissertation made several significant inferences. The primary outcomes are as follows:

- This work predicted stringent radial bounds for 1.4 $M_\odot$ NS, and compared to the other published works, these R constraints made significant improvements.
- Different groups of neutron star sources do not behave similarly under identical parameterization. In this project, QLMXBs represents the central portion of the combined dataset. Thus, these NSs dictate the overall radial bounds. Neutron star radii constraints do not always improve with additional observations. NICER observations shift the radial bounds towards larger values. This shift might be accurate but can only be concluded with more NICER statistics used in similar analyses.
- Intrinsic scattering calculations did not find any compelling unknown unknowns within the X-ray source data, but the procedure shown here can be used for more sophisticated analyses in the future.
- Lastly, this dissertation demonstrated that machine learning algorithms could be applied within NS model simulations. Supervised learning might enhance the timeframe of constructing improved models with upcoming neutron star observations.

To summarize; this dissertation provided successful models comprising both the gravitational wave and the electromagnetic wave observations, yielded an updated mass-radius and tidal deformability constraints of 1.4 $M_\odot$ neutron star, administered various correlation analysis on neutron star parameters and, discussed future possibilities of theoretical neutron star models. Thus, this work attempted to contribute to the vast and diverse discipline of neutron star research.

Bibliography

[1] Abbott, R. et al. (2020). GW190814: Gravitational Waves from the Coalescence of a 23 Solar Mass Black Hole with a 2.6 Solar Mass Compact Object. *Astrophys. J. Lett.*, 896(2):L44. 68, 98

[2] Al-Mamun, M., Steiner, A. W., Nättilä, J., Lange, J., O'Shaughnessy, R., Tews, I., Gandolfi, S., Heinke, C., and Han, S. (2021). Combining electromagnetic and gravitational-wave constraints on neutron-star masses and radii. *Phys. Rev. Lett.*, 126:061101. 57

[3] Annala, E., Gorda, T., Kurkela, A., and Vuorinen, A. (2018). Gravitational-wave constraints on the neutron-star-matter equation of state. *Phys. Rev. Lett.*, 120:172703. 67

[4] Antoniadis, J., Freire, P. C. C., Wex, N., Tauris, T. M., Lynch, R. S., van Kerkwijk, M. H., Kramer, M., Bassa, C., Dhillon, V. S., Driebe, T., Hessels, J. W. T., Kaspi, V. M., Kondratiev, V. I., Langer, N., Marsh, T. R., McLaughlin, M. A., Pennucci, T. T., Ransom, S. M., Stairs, I. H., van Leeuwen, J., Verbiest, J. P. W., and Whelan, D. G. (2013). A massive pulsar in a compact relativistic binary. *Science*, 340:6131. 8

[5] Baade, W. and Zwicky, F. (1934). Supernovae and cosmic rays. *Phys. Rev.*, 45:138. 20

[6] Backer, D. C., Kulkarni, S. R., Heiles, C., Davis, M. M., and Goss, W. M. (1982). A millisecond pulsar. *Nature*, 300(5893):615. 10

[7] Bahcall, J. N. and Wolf, R. A. (1965). Neutron stars. ii. neutrino-cooling and observability. *Phys. Rev.*, 140:B1452. 21

[8] Bell Burnell, S. J. (1977). Petit four*. *Annals of the New York Academy of Sciences*, 302(1):685. 10

[9] Benacquista, M. J. and Downing, J. M. B. (2013). Relativistic binaries in globular clusters. *Liv. Rev. Rel.*, 16:4. 28

[10] Bethe, H. A. (1990). Supernova mechanisms. *Reviews of Modern Physics*, 62:801. 3

[11] Blaes, O. M., Blandford, R. D., Madau, P., and Yan, L. (1992). On the evolution of slowly accreting neutron stars. *Astrophys. J.*, 399:634. 1

[12] Blandford, R. D., Applegate, J. H., and Hernquist, L. (1983). Thermal origin of neutron star magnetic fields. *Mon. Not. Royal. Astron. Soc.*, 204:1025. 11

[13] Bogdanov, S., Heinke, C. O., Özel, F., and Güver, T. (2016). Neutron star mass-radius constraints of the quiescent low-mass x-ray binaries x7 and x5 in the globular cluster 47 tuc. *The Astrophysical Journal*, 831(2):184. 21

[14] Brown, E. F., Bildsten, L., and Rutledge, R. E. (1998). Crustal heating and quiescent emission from transiently accreting neutron stars. *Astrophys. J. Lett.*, 504:L95. 12

[15] Burrows, A. (1987). The birth of neutron stars and black holes. *Physics Today*, 40(9):28. 2, 4

[16] Burrows, A. (2013). Colloquium: Perspectives on core-collapse supernova theory. *Rev. Mod. Phys.*, 85:245. 3

[17] Burrows, A. and Goshy, J. (1993). A theory of supernova explosions. *Astrophys. J. Lett.*, 416:L75. 3

[18] Burwitz, V., Haberl, F., Neuhaeuser, R., Predehl, P., Truemper, J., and Zavlin, V. E. (2003). The thermal radiation of the isolated neutron star rx j1856.5-3754 observed with chandra and xmm-newton. *Astron. Astrophys.*, 399:1109. 1

[19] Cameron and G., A. (1959). Neutron star models. *apj*, 130:884. 1

[20] Cameron, A. G. (1959). Neutron star models. *Astrophys. J.*, 130:884. 20

[21] Camilo, F., Thorsett, S. E., and Kulkarni, S. R. (1994). The magnetic fields, ages, and original spin periods of millisecond pulsars. *Astrophys. J. Lett.*, 421:L15. 11

[22] Capano, C. D., Tews, I., Brown, S. M., Margalit, B., De, S., Kumar, S., Brown, D. A., Krishnan, B., and Reddy, S. (2020). Stringent constraints on

neutron-star radii from multimessenger observations and nuclear theory. *Nat. Astron.*, 4:625. 67, 75

[23] Chadwick, J. (1932). The existence of a neutron. *Proceedings of the Royal Society of London. Series A, Containing Papers of a Mathematical and Physical Character*, 136(830):692. 19

[24] Chandrasekhar, S. (1931). The Maximum Mass of Ideal White Dwarfs. *Astrophys. J.*, 74:81. 20

[25] Chirenti, C., Gold, R., and Miller, M. C. (2017). Gravitational waves from f-modes excited by the inspiral of highly eccentric neutron star binaries. *The Astrophysical Journal*, 837(1):67. 25, 96

[26] Cromartie, H. T., Fonseca, E., Ransom, S. M., Demorest, P. B., Arzoumanian, Z., Blumer, H., Brook, P. R., Decesar, M. E., Dolch, T., Ellis, J. A., and et al. (2019). Relativistic shapiro delay measurements of an extremely massive millisecond pulsar. *Nature Astronomy*, 4(1):72. 22, 97

[27] De, S., Finstad, D., Lattimer, J. M., Brown, D. A., Berger, E., and Biwer, C. M. (2018). Tidal deformabilities and radii of neutron stars from the observation of gw170817. *Phys. Rev. Lett.*, 121:091102. 24, 58, 67, 72, 102

[28] De Luca, A. (2008). Central compact objects in supernova remnants. *AIP Conference Proceedings*, 983(1):311. 7

[29] d'Etivaux, N. B., Guillot, S., Margueron, J., Webb, N., Catelan, M., and Reisenegger, A. (2019). New constraints on the nuclear equation of state from the thermal emission of neutron stars in quiescent low-mass x-ray binaries. *Astrophys. J.*, 887(1):48. 67

[30] Detweiler, S. L. and Lindblom, L. (1985). On the nonradial pulsations of general relativistic stellar models. *Astrophys. J.*, 292:12. 25, 92

[31] Dietrich, T., Coughlin, M. W., Pang, P. T., Bulla, M., Heinzel, J., Issa, L., Tews, I., and Antier, S. (2020). New Constraints on the Supranuclear Equation

of State and the Hubble Constant from Nuclear Physics – Multi-Messenger Astronomy. *Science*, 370(6523):1450. 67

[32] Du, X., Steiner, A. W., and Holt, J. W. (2019). Hot and dense homogeneous nucleonic matter constrained by observations, experiment, and theory. *Phys. Rev. C*, 99:025803. 38

[33] Duncan, R. C. (1998). Global seismic oscillations in soft gamma repeaters. *The Astrophysical Journal*, 498(1):L45. 88

[34] Einstein, A. (1916). Näherungsweise Integration der Feldgleichungen der Gravitation. *Sitzungsberichte der Königlich Preußischen Akademie der Wissenschaften (Berlin)*, page 688. 14

[35] Elshamouty, K. G., Heinke, C. O., Morsink, S. M., Bogdanov, S., and Stevens, A. L. (2016). The impact of surface temperature inhomogeneities on quiescent neutron star radius measurements. *Astrophys. J*, 826(2):162. 9

[36] Espinoza, C. M., Lyne, A. G., Stappers, B. W., and Kramer, M. (2011). A study of 315 glitches in the rotation of 102 pulsars. *Monthly Notices of the Royal Astronomical Society*, 414(2):1679. 11

[37] Essick, R. and Landry, P. (2020). Discriminating between neutron stars and black holes with imperfect knowledge of the maximum neutron star mass. *Astrophys. J.*, 904(1):80. 68, 98

[38] Essick, R., Tews, I., Landry, P., Reddy, S., and Holz, D. E. (2020). Direct astrophysical tests of chiral effective field theory at supranuclear densities. *Phys. Rev. C*, 102:055803. 67

[39] Fattoyev, F. J., Piekarewicz, J., and Horowitz, C. J. (2018). Neutron skins and neutron stars in the multimessenger era. *Phys. Rev. Lett.*, 120:172702. 67

[40] Fewell, M. P. (1995). The atomic nuclide with the highest mean binding energy. *American Journal of Physics*, 63(7):653. 3

[41] Gandolfi, S., Carlson, J., and Reddy, S. (2012). Maximum mass and radius of neutron stars, and the nuclear symmetry energy. *Phys. Rev. C*, 85:032801(R). 1, 37

[42] Gold, T. (1968). Rotating neutron stars as the origin of the pulsating radio sources. 11

[43] Goodman, J. and Weare, J. (2010). Ensemble samplers with affine invariance. *Commun. App. Math. and Comput. Sci.*, 5:65. 49

[44] Haensel, P., Potekhin, A., and Yakovlev, D. (2007). *Neutron Stars 1 - Equation of State and Structure: P. Haensel*. Springer-Verlag New York. 4

[45] Han, S. and Prakash, M. (2020). On the minimum radius of very massive neutron stars. *The Astrophysical Journal*, 899(2):164. 98

[46] Handler, G. (2013). *Asteroseismology*, pages 207–241. Springer Netherlands, Dordrecht. 88

[47] Harris, C. R., Millman, K. J., van der Walt, S. J., Gommers, R., Virtanen, P., Cournapeau, D., Wieser, E., Taylor, J., Berg, S., Smith, N. J., Kern, R., Picus, M., Hoyer, S., van Kerkwijk, M. H., Brett, M., Haldane, A., Fernández del Río, J., Wiebe, M., Peterson, P., Gérard-Marchant, P., Sheppard, K., Reddy, T., Weckesser, W., Abbasi, H., Gohlke, C., and Oliphant, T. E. (2020). Array programming with NumPy. *Nature*, 585:357. 81

[48] Hartle, J. B. (1967). Slowly Rotating Relativistic Stars. I. Equations of Structure. *The Astrophysical Journal*, 150:1005. 44

[49] Hawking, S. W. (1972). Gravitational radiation: The theoretical aspect. *Contemporary Physics*, 13(3):273. 14

[50] Heger, A., Fryer, C. L., Woosley, S. E., Langer, N., and Hartmann, D. H. (2003). How massive single stars end their life. *The Astrophysical Journal*, 591(1):288. 2

[51] Heinke, C. O., Grindlay, J. E., Lugger, P. M., Cohn, H. N., Edmonds, P. D., Lloyd, D. A., and Cool, A. M. (2003). Analysis of the quiescent low-mass x-ray binary population in galactic globular clusters. *The Astrophysical Journal*, 598(1):501. 12

[52] Heinke, C. O., Rybicki, G. B., Narayan, R., and Grindlay, J. E. (2006). A hydrogen atmosphere spectral model applied to the neutron star x7 in the globular cluster 47 tucanae. *The Astrophysical Journal*, 644(2):1090. 21

[53] Hewish, A., Bell, S. J., Pilkington, J. D. H., Scott, P. F., and Collins, R. A. (1968). Observation of a rapidly pulsating radio source. *Nature (London)*, 217:709. 21

[54] Hinderer, T. (2008). Tidal love numbers of neutron stars. *The Astrophysical Journal*, 677(2):1216. 25, 96, 103

[55] Ho-Yin Ng, H., Chi-Kit Cheong, P., Lin, L.-M., and Li, T. G. F. (2020). Gravitational-wave asteroseismology with f-modes from neutron star binaries at the merger phase. *arXiv e-prints*, page arXiv:2012.08263. 96

[56] Hulse, R. A. and Taylor, J. H. (1975). Discovery of a pulsar in a binary system. *Astrophys. J.*, 195:L51. 8, 21

[57] Jiang, J.-L., Tang, S.-P., Shao, D.-S., Han, M.-Z., Li, Y.-J., Wang, Y.-Z., Jin, Z.-P., Fan, Y.-Z., and Wei, D.-M. (2019). The equation of state and some key parameters of neutron stars: Constraints from GW170817, the nuclear data, and the low-mass x-ray binary data. *Astrophys. J.*, 885(1):39. 67

[58] Jiang, J.-L., Tang, S.-P., Wang, Y.-Z., Fan, Y.-Z., and Wei, D.-M. (2020). PSR j0030+0451, GW170817, and the nuclear data: Joint constraints on equation of state and bulk properties of neutron stars. *Astrophys. J.*, 892(1):55. 67

[59] Kokkotas, K. D. (2008). *Gravitational Wave Astronomy*, pages 140–166. John Wiley and Sons, Ltd. 14

[60] Kortelainen, M., Lesinski, T., Moré, J., Nazarewicz, W., Sarich, J., Schunck, N., Stoitsov, M. V., and Wild, S. (2010). Nuclear energy density optimization. *Phys. Rev. C*, 82:024313. 40

[61] Kortelainen, M., McDonnell, J., Nazarewicz, W., Olsen, E., Reinhard, P.-G., Sarich, J., Schunck, N., Wild, S. M., Davesne, D., Erler, J., and Pastore, A. (2014). Nuclear energy density optimization: Shell structure. *Phys. Rev. C*, 89:054314. 38

[62] Kumar, B. and Landry, P. (2019). Inferring neutron star properties from gw170817 with universal relations. *Phys. Rev. D*, 99:123026. 67

[63] Kumar, H. S., Safi-Harb, S., and Gonzalez, M. E. (2012). Chandra and xmm-newton studies of the supernova remnant g292.2-0.5 associated with the pulsar j1119-6127. *Astrophys. J.*, 754:96. 1

[64] Landau, L. (1932). On the theory of stars. *Phys. Z. Sowjetunion*, 1:185. 19

[65] Landry, P. and Essick, R. (2019). Nonparametric inference of the neutron star equation of state from gravitational wave observations. *Phys. Rev. D*, 99:084049. 67

[66] Landry, P., Essick, R., and Chatziioannou, K. (2020). Nonparametric constraints on neutron star matter with existing and upcoming gravitational wave and pulsar observations. *Phys. Rev. D*, 101:123007. 67

[67] Lasota, J.-P. (2001). The disc instability model of dwarf novae and low-mass x-ray binary transients. *New Astronomy Reviews*, 45(7):449. 12

[68] Lattimer, J. M. (2019). Neutron star mass and radius measurements. *Universe*, 5(7):159. 1, 58, 97

[69] Lattimer, J. M. and Prakash, M. (2001). Neutron star structure and the equation of state. *The Astrophysical Journal*, 550(1):426. 1, 75

[70] Lattimer, J. M. and Steiner, A. W. (2014). Neutron star masses and radii from quiescent low-mass x-ray binaries. *Astrophys. J.*, 784:123. 1

[71] Li, B.-A. and Steiner, A. W. (2006). Constraining the radii of neutron stars with terrestrial nuclear laboratory data. *Phys. Lett. B*, 642:436. 1

[72] Lieb, E. H. and Yau, H.-T. (1987). A Rigorous Examination of the Chandrasekhar Theory of Stellar Collapse. *Astrophys. J.*, 323:140. 3

[73] LIGO Scientific and Virgo Collaborations (2017). Gw170817: Observation of gravitational waves from a binary neutron star inspiral. *Phys. Rev. Lett.*, 119:161101. 1, 14, 21

[74] LIGO Scientific and Virgo Collaborations (2018). Gw170817: Measurements of neutron star radii and equation of state. *Phys. Rev. Lett.*, 121:161101. 14, 28, 58, 67

[75] LIGO Scientific and Virgo Collaborations (2019). Properties of the binary neutron star merger gw170817. *Phys. Rev. X*, 9:011001. 22, 28

[76] Linares, M., Shahbaz, T., and Casares, J. (2018). Peering into the dark side: Magnesium lines establish a massive neutron star in PSR j2215+5135. *The Astrophysical Journal*, 859(1):54. 22, 97

[77] Lindblom, L. and Detweiler, S. L. (1983). The quadrupole oscillations of neutron stars. *Astrophys. J.*, 53:73. 90, 92, 96

[78] Liu, Q. Z., van Paradijs, J., and van den Heuvel, E. P. J. (2007). A catalogue of low-mass x-ray binaries in the galaxy, lmc, and smc. *Astronomy and Astrophysics*, 469(2):807. 7

[79] Love, A. E. H. (1909). The yielding of the earth to disturbing forces. *Proceedings of the Royal Society of London. Series A, Containing Papers of a Mathematical and Physical Character*, 82(551):73. 45

[80] Maselli, A., Cardoso, V., Ferrari, V., Gualtieri, L., and Pani, P. (2013). Equation-of-state-independent relations in neutron stars. *Phys. Rev. D*, 88:023007. 24, 72, 102

[81] Mereghetti, S. (2011). *High-Energy Emission from Pulsars and their Systems*. Springer Berlin Heidelberg, Berlin, Heidelberg. 7

[82] Middleditch, J. and Priedhorsky, W. C. (1986). Discovery of Rapid Quasi-periodic Oscillations in Scorpius X-1. *Astrophys. J.*, 306:230. 11

[83] Misner, C. W., Thorne, K. S., and Wheeler, J. A. (1973). *Gravitation*. W. H. Freeman, San Francisco. 14

[84] Nättilä, J., Miller, M. C., Steiner, A. W., Kajava, J. J. E., Suleimanov, V. F., and Poutanen, J. (2017). Neutron star mass and radius measurements from atmospheric model fits to x-ray burst cooling tail spectra. *Astron. and Astrophys.*, 608:A31. 27, 28

[85] Nättilä, J., Steiner, A. W., Kajava, J. J. E., Suleimanov, V. F., and Poutanen, J. (2016). Equation of state constraints for the cold dense matter inside neutron stars using the cooling tail method. *Astron. Astrophys.*, 591:A25. 28

[86] Nättilä, J., Miller, M. C., Steiner, A. W., Kajava, J. J. E., Suleimanov, V. F., and Poutanen, J. (2017). Neutron star mass and radius measurements from atmospheric model fits to x-ray burst cooling tail spectra. *A&A*, 608:A31. 22, 34

[87] Navarro, J., Manchester, R. N., Sandhu, J. S., Kulkarni, S. R., and Bailes, M. (1997). Mean Pulse Shape and Polarization of PSR J0437-4715. *Astrophys. J.*, 486(2):1019. 11

[88] Oppenheimer, J. and Volkoff, G. (1939). On Massive neutron cores. *Phys. Rev.*, 55:374. 20

[89] Pavlov, G. G., Sanwal, D., and Teter, M. A. (2004). Central compact objects in supernova remnants. *IAU Symp.*, 218:239. 1, 7

[90] Pedregosa, F., Varoquaux, G., Gramfort, A., Michel, V., Thirion, B., Grisel, O., Blondel, M., Prettenhofer, P., Weiss, R., Dubourg, V., Vanderplas, J., Passos, A., Cournapeau, D., Brucher, M., Perrot, M., and Duchesnay, E. (2011). Scikit-learn: Machine learning in Python. *Journal of Machine Learning Research*, 12:2825. 32, 81

[91] Pons, J. A., Reddy, S., Prakash, M., Lattimer, J. M., and Miralles, J. A. (1999). Evolution of proto–neutron stars. *The Astrophysical Journal*, 513(2):780. 1

[92] Pons, J. A., Steiner, A. W., Prakash, M., and Lattimer, J. M. (2001). Evolution of proto-neutron stars with quarks. *Phys. Rev. Lett.*, 86:5223. 1

[93] Raaijmakers, G., Riley, T. E., Watts, A. L., Greif, S. K., Morsink, S. M., Hebeler, K., Schwenk, A., Hinderer, T., Nissanke, S., Guillot, S., Arzoumanian, Z., Bogdanov, S., Chakrabarty, D., Gendreau, K. C., Ho, W. C. G., Lattimer, J. M., Ludlam, R. M., and Wolff, M. T. (2019). A NICER view of PSR j0030+0451: Implications for the dense matter equation of state. *Astrophys. J*, 887(1):L22. 1, 28

[94] Radhakrishnan, V. and Cooke, D. J. (1969). Magnetic Poles and the Polarization Structure of Pulsar Radiation. *Astrophysical Letters*, 3:225. 11

[95] Radice, D. and Dai, L. (2019). Multimessenger parameter estimation of gw170817. *Eur. Phys. J. A*, 55(4):50. 58, 67

[96] Raithel, C. A. (2019). Constraints on the Neutron Star Equation of State from GW170817. *Eur. Phys. J. A*, 55(5):80. 67

[97] Raithel, C. A., Özel, F., and Psaltis, D. (2021). Optimized statistical approach for comparing multi-messenger neutron star data. *Astrophys. J*, 908(1):103. 67

[98] Ransom, S. M., Stairs, I. H., Archibald, A. M., Hessels, J. W. T., Kaplan, D. L., van Kerkwijk, M. H., Boyles, J., Deller, A. T., Chatterjee, S., Schechtman-Rook, A., Berndsen, A., Lynch, R. S., Lorimer, D. R., Karako-Argaman, C., Kaspi, V. M., Kondratiev, V. I., McLaughlin, M. A., van Leeuwen, J., Rosen, R., Roberts, M. S. E., and Stovall, K. (2014). A millisecond pulsar in a stellar triple system. *Nature*, 505(7484):520. 8

[99] Rasmussen, C. E. (2004). *Gaussian Processes in Machine Learning*, pages 63–71. Springer Berlin Heidelberg, Berlin, Heidelberg. 80

[100] REICHLEY, P. E. and DOWNS, G. S. (1969). Observed decrease in the periods of pulsar psr 0833–45. *Nature*, 222(5190):229. 11

[101] Ridolfi, A., Gautam, T., Freire, P. C. C., Ransom, S. M., Buchner, S. J., Possenti, A., Venkatraman Krishnan, V., Bailes, M., Kramer, M., Stappers, B. W., Abbate, F., Barr, E. D., Burgay, M., Camilo, F., Corongiu, A., Jameson, A., Padmanabh, P. V., Vleeschower, L., Champion, D. J., Chen, W., Geyer, M., Karastergiou, A., Karuppusamy, R., Parthasarathy, A., Reardon, D. J., Serylak, M., Shannon, R. M., and Spiewak, R. (2021). Eight new millisecond pulsars from the first MeerKAT globular cluster census. *Monthly Notices of the Royal Astronomical Society*, 504(1):1407. 10

[102] Riley, T. E., Watts, A. L., Bogdanov, S., Ray, P. S., Ludlam, R. M., Guillot, S., Arzoumanian, Z., Baker, C. L., Bilous, A. V., Chakrabarty, D., Gendreau, K. C., Harding, A. K., Ho, W. C. G., Lattimer, J. M., Morsink, S. M., and Strohmayer, T. E. (2019). A NICER view of PSR j0030+0451: Millisecond pulsar parameter estimation. *Astrophys. J.*, 887(1):L21. 1, 23, 28

[103] Ruiz, M., Shapiro, S. L., and Tsokaros, A. (2018). Gw170817, general relativistic magnetohydrodynamic simulations, and the neutron star maximum mass. *Phys. Rev. D*, 97:021501. 68

[104] Schutz, B. F. (1985). *A First Course in Gneneral Relativity*. Cambridge Univ. Pr., Cambridge, UK. 14

[105] Scientific, L. and Collaboration, V. (2016). Observation of gravitational waves from a binary black hole merger. *Phys. Rev. Lett.*, 116:061102. 14

[106] Servillat, M., Heinke, C. O., Ho, W. C. G., Grindlay, J. E., Hong, J., van den Berg, M., and Bogdanov, S. (2012). Neutron star atmosphere composition: the quiescent, low-mass X-ray binary in the globular cluster M28. *Monthly Notices of the Royal Astronomical Society*, 423(2):1556. 13

[107] Shapiro, S. L. and Teukolsky, S. A. (1983). *Black Holes, White Dwarfs, and Neutron Stars*. John Wiley and Sons, Ltd. 2

[108] Shaw, A. W., Heinke, C. O., Steiner, A. W., Campana, S., Cohn, H. N., Ho, W. C. G., Lugger, P. M., and Servillat, M. (2018). The radius of the quiescent neutron star in the globular cluster m13. *Mon. Not. R. Astron. Soc.*, 476:4713. 27

[109] Skyrme, T. (1958). The effective nuclear potential. *Nuclear Physics*, 9(4):615–634. 20

[110] Stairs, I. H. (2003). Testing general relativity with pulsar timing. *Living Reviews in Relativity*. 9

[111] Steiner, A. W., Gandolfi, S., Fattoyev, F. J., and Newton, W. G. (2015). Using neutron star observations to determine crust thicknesses, moments of inertia, and tidal deformabilities. *Phys. Rev. C*, 91:015804. 37

[112] Steiner, A. W., Heinke, C. O., Bogdanov, S., Li, C., Ho, W. C. G., Bahramian, A., and Han, S. (2018). Constraining the mass and radius of neutron stars in globular clusters. *Mon. Not. R. Astron. Soc.*, 476:421. 21, 22, 27, 54

[113] Steiner, A. W., Lattimer, J. M., and Brown, E. F. (2013). The neutron star mass-radius relation and the equation of state of dense matter. *Astrophys. J. Lett.*, 765:L5. 1

[114] Steiner, A. W., Lattimer, J. M., and Brown, E. F. (2016). Neutron star radii, universal relations, and the role of prior distributions. *Eur. Phys. J. A*, 52:18. 1, 75

[115] Steiner, A. W., Prakash, M., Lattimer, J. M., and Ellis, P. J. (2005). Isospin asymmetry in nuclei and neutron stars. *Phys. Rep.*, 411:325. 40

[116] Sukhbold, T., Ertl, T., Woosley, S. E., Brown, J. M., and Janka, H.-T. (2016). Core-collapse supernovae from 9 to 120 solar masses based on neutrino-powered explosions. *The Astrophysical Journal*, 821(1):38. 2

[117] Tews, I., Pang, P. T. H., Dietrich, T., Coughlin, M. W., Antier, S., Bulla, M., Heinzel, J., and Issa, L. (2021). On the nature of GW190814 and its impact on the understanding of supranuclear matter. *Astrophys. J*, 908(1):L1. 68, 98

[118] Thorne, K. S. and Campolattaro, A. (1967). Non-Radial Pulsation of General-Relativistic Stellar Models. I. Analytic Analysis for L ¿= 2. *Astrophys. J.*, 149:591. 89

[119] Thorsett, S. E., Arzoumanian, Z., Camilo, F., and Lyne, A. G. (1999). The triple pulsar system psr b1620-26 in m4. *The Astrophysical Journal*, 523(2):763. 8

[120] Thorsett, S. E. and Chakrabarty, D. (1999). Neutron star mass measurements. i. radio pulsars. *Astrophys. J.*, 512(1):288. 1

[121] Tolman, R. C. (1939). Static solutions of Einstein's field equations for spheres of fluid. *Phys. Rev.*, 55:364. 20

[122] van den Heuvel, E. P. J. (2018). High-mass x-ray binaries: progenitors of double compact objects. *Proceedings of the International Astronomical Union*, 14(S346):1. 7

[123] van der Klis, M., Jansen, F., van Paradijs, J., Lewin, W. H. G., van den Heuvel, E. P. J., Trümper, J. E., and Sztajno, M. (1985). Intensity-dependent quasi-periodic oscillations in the x-ray flux of gx5-1. *Nature*, 316(6025):225. 11

[124] van Paradijs, J. (1982). Some remarks on the spectra of X-ray bursts. *Astronomy and Astrophysics*, 107:51. 13

[125] Virtanen, P., Gommers, R., Oliphant, T. E., Haberland, M., Reddy, T., Cournapeau, D., Burovski, E., Peterson, P., Weckesser, W., Bright, J., van der Walt, S. J., Brett, M., Wilson, J., Millman, K. J., Mayorov, N., Nelson, A. R. J., Jones, E., Kern, R., Larson, E., Carey, C. J., Polat, İ., Feng, Y., Moore, E. W., VanderPlas, J., Laxalde, D., Perktold, J., Cimrman, R., Henriksen, I., Quintero, E. A., Harris, C. R., Archibald, A. M., Ribeiro, A. H., Pedregosa, F., van Mulbregt, P., and SciPy 1.0 Contributors (2020). SciPy 1.0: Fundamental Algorithms for Scientific Computing in Python. *Nature Methods*, 17:261. 81

[126] Wen, D.-H., Li, B.-A., Chen, H.-Y., and Zhang, N.-B. (2019). GW170817 implications on the frequency and damping time of f -mode oscillations of neutron stars. *Physical Review C*, 99(4):045806. 25, 97, 103

[127] Williams, C. and Rasmussen, C. (1996). Gaussian processes for regression. In *Advances in neural information processing systems 8*, pages 514–520, Cambridge, MA, USA. Max-Planck-Gesellschaft, MIT Press. 80

[128] Woodley, K. A., Goldsbury, R., Kalirai, J. S., Richer, H. B., Tremblay, P.-E., Anderson, J., Bergeron, P., Dotter, A., Esteves, L., Fahlman, G. G., Hansen, B. M. S., Heyl, J., Hurley, J., Rich, R. M., Shara, M. M., and Stetson, P. B. (2012). The spectral energy distributions of white dwarfs in 47 tucanae: The distance to the cluster. *Astron. J.*, 143(2):50. 27

[129] Yagi, K. and Yunes, N. (2013). I-love-q: Unexpected universal relations for neutron stars and quark stars. *Science*, 341(6144):365. 46, 71

[130] Yagi, K. and Yunes, N. (2017). Approximate universal relations among tidal parameters for neutron star binaries. *Classical and Quantum Gravity*, 34(1):015006. 24, 71, 72, 102

[131] Özel, F. (2012). Surface emission from neutron stars and implications for the physics of their interiors. *Reports on Progress in Physics*, 76(1):016901. 9

[132] Özel, F., Psaltis, D., Güver, T., Baym, G., Heinke, C., and Guillot, S. (2016). The dense matter equation of state from neutron star radius and mass measurements. *The Astrophysical Journal*, 820(1):28. 21

[133] Özel, F., Psaltis, D., Narayan, R., and Villarreal, A. S. (2012). On the mass distribution and birth masses of neutron stars. *The Astrophysical Journal*, 757(1):55. 97

Appendices

A Correlations Between Binary Parameters

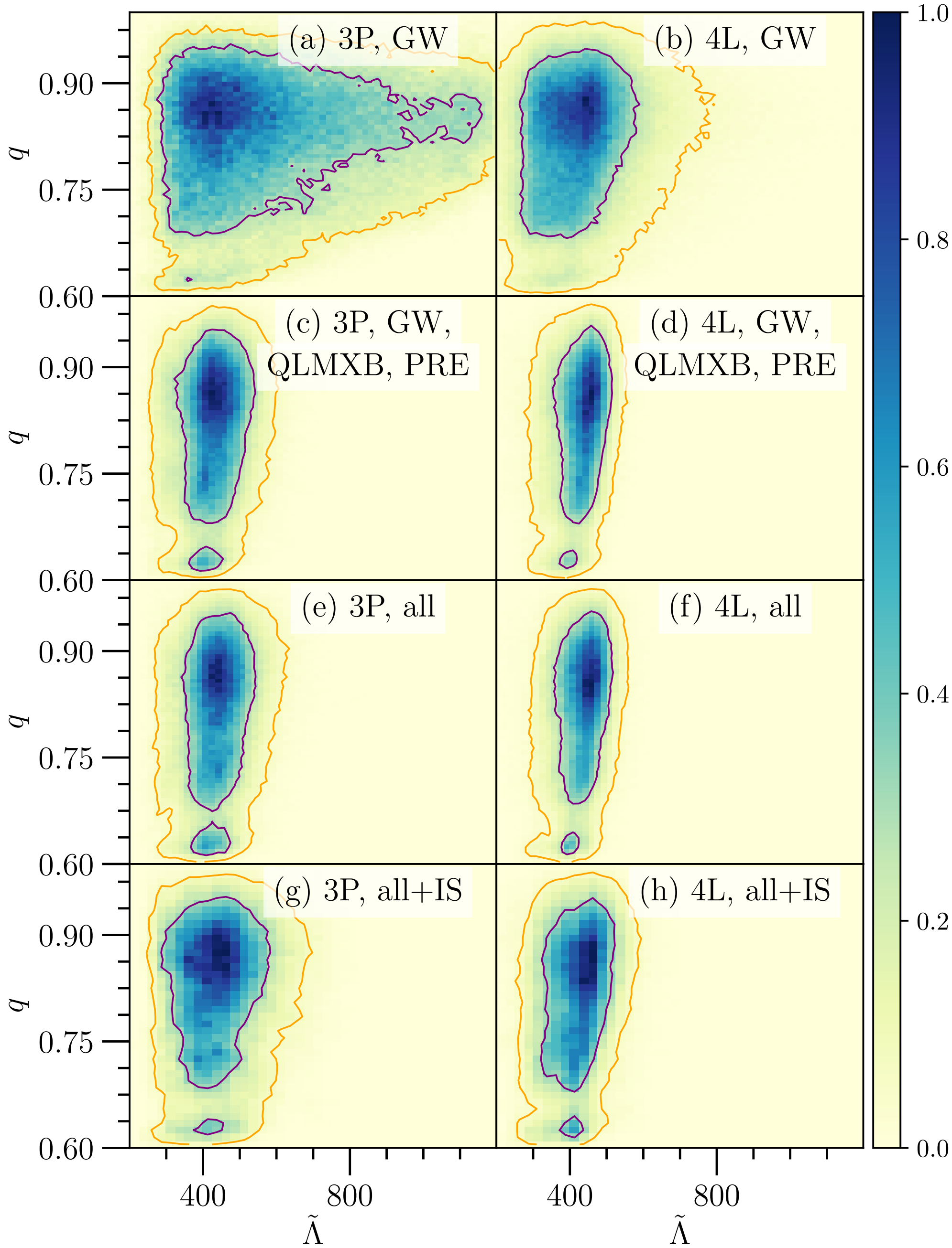

Figure 1: Posterior distributions presenting the relation between the mass ratio q with the tidal deformability $\tilde{\Lambda}$. Models with EM data can strongly limit the range of $\tilde{\Lambda}$. The min-max range of q remains mostly unaffected by different model descriptions.

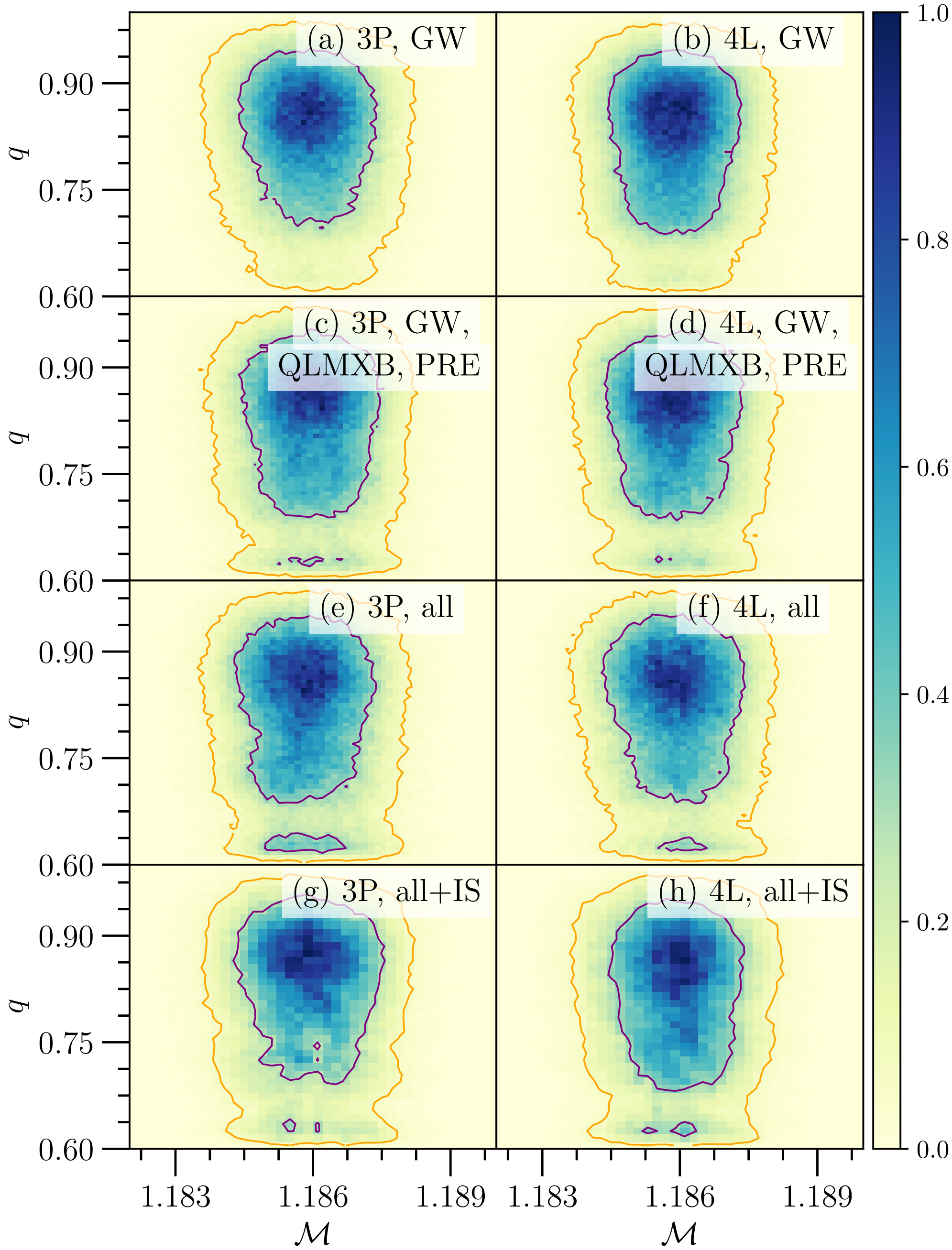

Figure 2: Posterior distributions presenting the relation between the mass ratio q with the chirp mass $\mathcal{M}$. These posteriors are mostly unaffected by the difference in datasets.

B M-R Variations in IS Models

Section 3.4 reviewed the low probability in 3P models of finding a neutron star with 2.6 $M_{\odot}$. There are still possibilities to find a massive enough neutron star from the polytropic models, comparable to the X-ray sources with large masses. This appendix will present the maximum allowed mass based on the current form of the intrinsic scattering models. For this specific section, the IS models do not contain any additional benefits over the other models.

Tables 1 is constructed from the "3P, all+IS" posteriors, and it contains the radial ranges for neutron stars with all possible masses. Here, the masses lower than the solar mass is discarded. The maximum mass archived in the "3P, all+IS" model is 2.4 $M_{\odot}$. Although it is not high enough to include the mass from GW190814, this maximum mass limit will still incorporate the most massive neutron star.

Table 2 contains the radial ranges from model "4L, all+IS" with all allowed masses. The line-segment models can generate neutron star mass up to 2.7 $M_{\odot}$. The 4L models were constructed to allow implicit phase transitions, which may be the possible reason for larger mass predictions. The implication of getting larger masses in 4L models is that the phase transitions may be the physics behind the formation of massive neutron stars.

Table 1: Neutron star radii (in km), with the 1σ and 2σ C.I. for model "3P, all+IS".

M ($\mathrm{M}_\odot$)	R (km)			
	-2σ	-1σ	$+1\sigma$	$+2\sigma$
1.00	11.20	11.63	12.42	12.76
1.10	11.19	11.62	12.41	12.77
1.20	11.19	11.61	12.41	12.77
1.30	11.19	11.61	12.40	12.77
1.40	11.18	11.60	12.39	12.75
1.50	11.17	11.59	12.37	12.73
1.60	11.13	11.56	12.35	12.68
1.70	11.09	11.53	12.34	12.65
1.80	11.00	11.45	12.30	12.60
1.90	10.88	11.36	12.26	12.56
2.00	10.59	11.14	12.17	12.51
2.10	10.77	11.25	12.16	12.51
2.20	11.04	11.43	12.20	12.52
2.30	11.23	11.57	12.23	12.51
2.40	11.53	11.77	12.29	12.52

Table 2: Neutron star radii (in km), with the 1σ and 2σ C.I. of for model"4L, all+IS".

M ($M_\odot$)	R (km)			
	-2σ	-1σ	$+1\sigma$	$+2\sigma$
1.00	10.88	11.16	11.86	12.38
1.10	10.95	11.27	11.92	12.37
1.20	11.01	11.36	11.98	12.38
1.30	11.07	11.46	12.06	12.40
1.40	11.12	11.54	12.14	12.45
1.50	11.15	11.58	12.19	12.49
1.60	11.16	11.61	12.24	12.53
1.70	11.15	11.67	12.30	12.58
1.80	11.11	11.70	12.36	12.62
1.90	11.04	11.70	12.39	12.64
2.00	10.85	11.68	12.44	12.66
2.10	10.87	11.70	12.47	12.67
2.20	11.05	11.75	12.50	12.69
2.30	11.21	11.80	12.52	12.70
2.40	11.37	11.85	12.55	12.77
2.50	11.53	11.89	12.56	12.71
2.60	11.74	11.99	12.52	12.73
2.70	11.98	12.13	12.47	12.62

C Compactness of NS Binaries

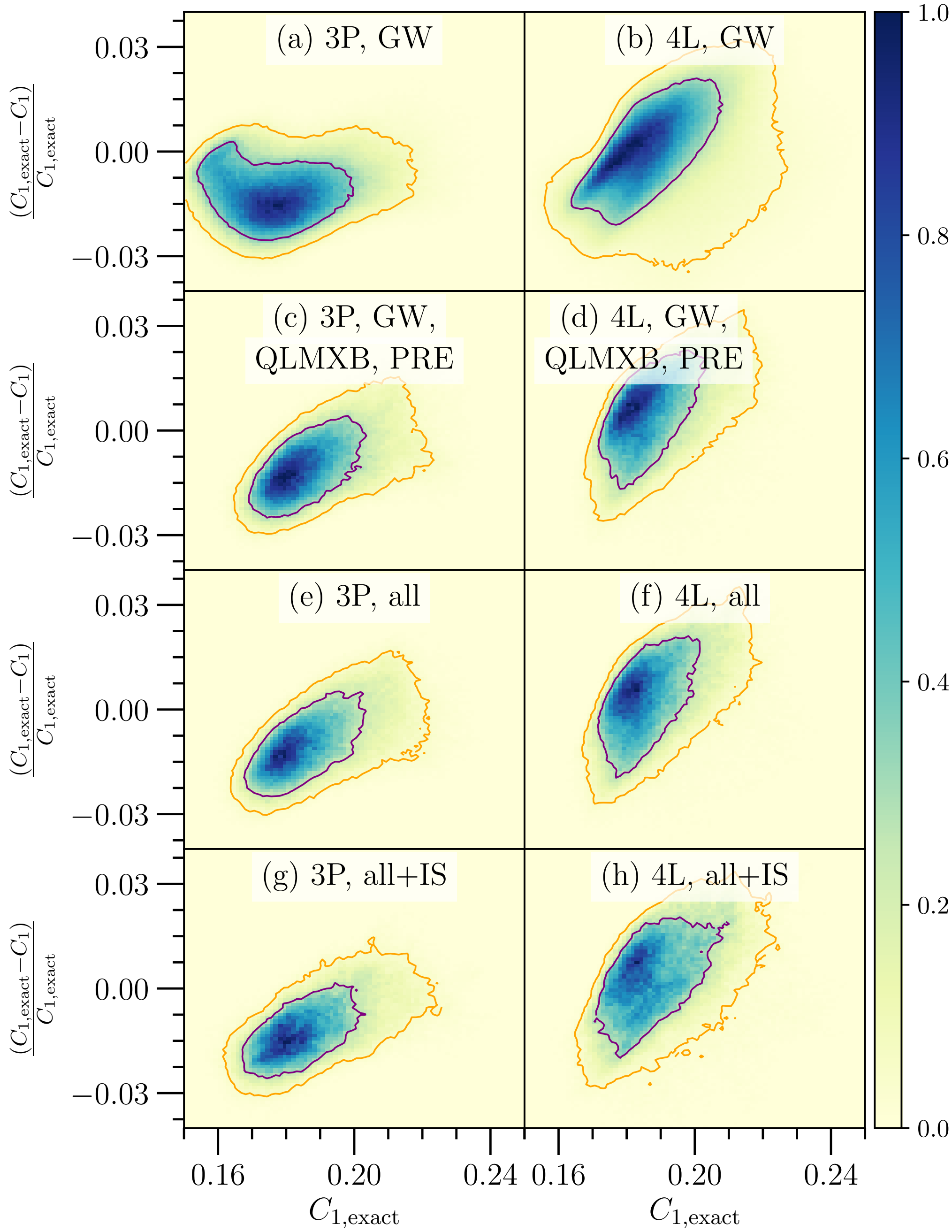

Figure 3: Posterior distributions for the deviations between $C_{\mathrm{exact},1}$ and C_1 versus $C_{\mathrm{exact},1}$.

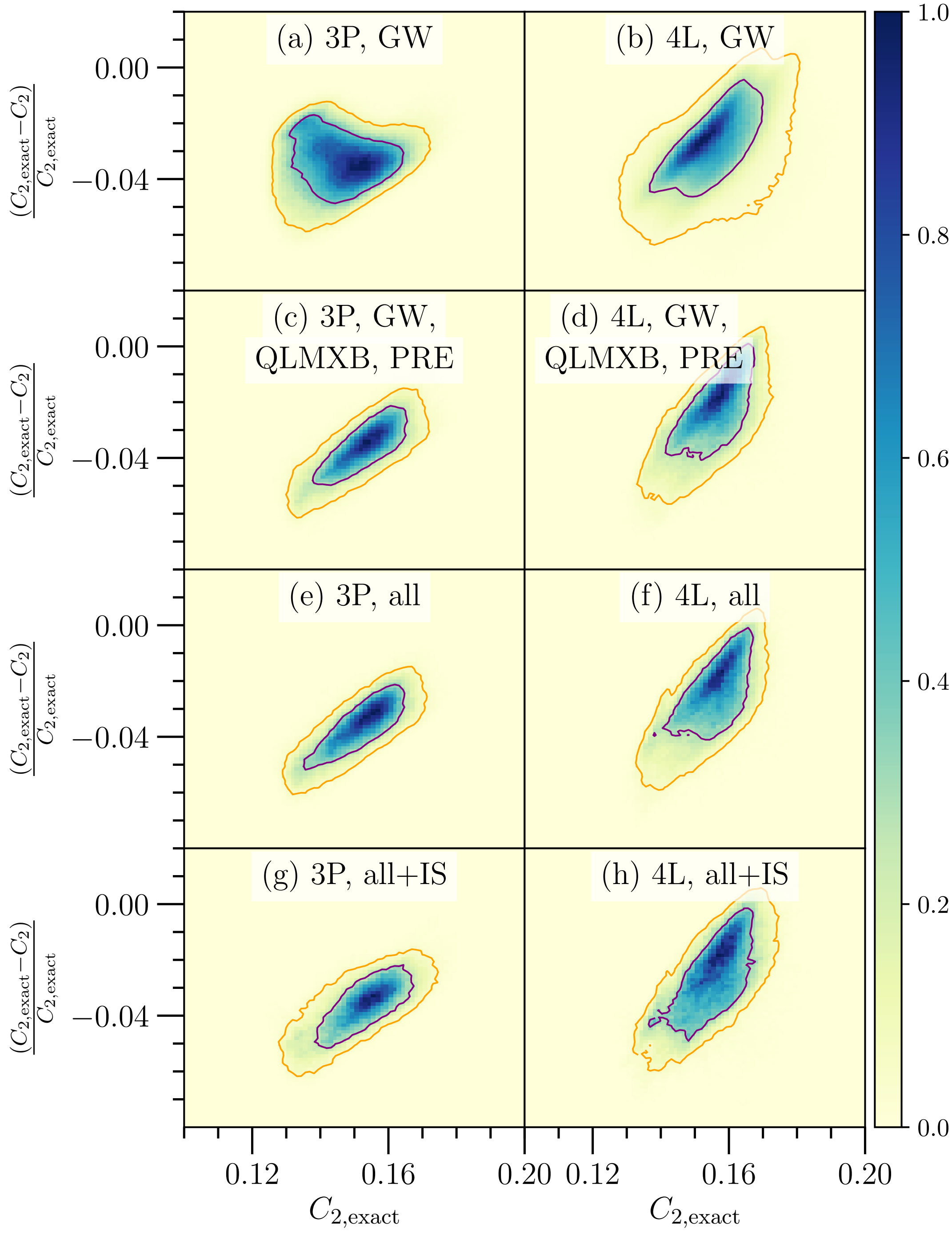

Figure 4: Posterior distributions for the deviations between $C_{\mathrm{exact},2}$ and C_2 versus $C_{\mathrm{exact},2}$.

Vita

Originally from Bangladesh, Mohammad Al-Mamun grew up in Dhaka, Bangladesh. After high school and college, he attended the University of Dhaka and received a Bachelor of Science degree in Physics. He attended the Theoretical Physics department in the same university to complete his Masters in Science degree. He chose to attend the University of Tennessee, Knoxville, to pursue a Doctor of Philosophy degree in Physics with a concentration in Nuclear Astrophysics Theory. His research interest includes studying the structure of neutron stars with electromagnetic and gravitational wave observations. After graduation, he will apply his acquired skills during graduate studies in computational research and development. He is incredibly grateful to his parents, friends, and doctoral advisor as he starts his new career.